STATE OF CALIFORNIA • DEPARTMENT OF TRANSPORTATION

TECHNICAL REPORT DOCUMENTATION PAGE

TR-0003 (REV 04/2024)

1. REPORT NUMBER	2. GOVERNMENT ASSOCIATION NUMBER	3. RECIPIENT'S CATALOG NUMBER
CA25-4418		

4. TITLE AND SUBTITLE	5. REPORT DATE
Effect of Fines on Liquefaction Triggering Analyses	December 2025
	6. PERFORMING ORGANIZATION CODE

7. AUTHOR	8. PERFORMING ORGANIZATION REPORT NO.
Varun N. S. Renugah, Arda Sahin, Scott J. Brandenberg, Jonathan P. Stewart	

9. PERFORMING ORGANIZATION NAME AND ADDRESS	10. WORK UNIT NUMBER
Natural Hazards Risk and Resiliency Research Center (NHR3), Department of Civil and Environmental Engineering University of California, Los Angeles 404 Westwood Plaza, Los Angeles, CA 90095	11. CONTRACT OR GRANT NUMBER 65A0774 TO 011

12. SPONSORING AGENCY AND ADDRESS	13. TYPE OF REPORT AND PERIOD COVERED
California Department of Transportation 1120 N St., Sacramento, CA 95814	4/08/2024 - 2/28/2025
	14. SPONSORING AGENCY CODE

15. SUPPLEMENTARY NOTES

16. ABSTRACT

This report presents a new framework for applying fines content corrections in soil liquefaction evaluations. Fines content affects both penetration resistance and cyclic resistance, but current methods use a single correction to represent both effects. This study separates these influences by using variable-rate CPT data to assess the effect of fines on penetration resistance, and cyclic laboratory test data to evaluate their impact on cyclic resistance. While fines consistently reduce penetration resistance, their effect on cyclic strength may increase or decrease depending on factors such as coarse fraction state, fines plasticity, and overconsolidation.

The influence of fines on CPT drainage conditions is examined to develop relationships that adjust measured cone resistance to equivalent drained conditions using the soil behavior type index. These relationships allow CPT data obtained under partially drained or undrained conditions to be normalized to clean-sand conditions.

A methodology is proposed for evaluating cyclic strength of soils with varying fines content by integrating clean-sand liquefaction triggering concepts with fine-grained soil cyclic failure models. Clean sand resistance is evaluated using an NGL laboratory-based model, while fine-grained soil resistance is estimated using a new model developed in this report that accounts for plasticity and overconsolidation. An interpolation approach is provided for soils with intermediate fines content.

The proposed corrections are applied to critical layer data from an existing CPT-based triggering model and compared with legacy approaches. The study also assesses alternative seismic intensity measures and finds no improvement over peak horizontal acceleration and magnitude when evaluated against field liquefaction data.

17. KEY WORDS	18. DISTRIBUTION STATEMENT
Fines content, liquefaction triggering, cyclic softening, cyclic resistance ratio, cone penetration test	No Restrictions

19. SECURITY CLASSIFICATION *(of this report)*	20. NUMBER OF PAGES	21. COST OF REPORT CHARGED
Unclassified	69	

DISCLAIMER STATEMENT

This document is disseminated in the interest of information exchange. The contents of this report reflect the views of the authors who are responsible for the facts and accuracy of the data presented herein. The contents do not necessarily reflect the official views or policies of the State of California or the Federal Highway Administration. This publication does not constitute a standard, specification or regulation. This report does not constitute an endorsement by the Department of any product described herein.

For individuals with sensory disabilities, this document is available in alternate formats. For information, call (916) 654-8899, TTY 711, or write to California Department of Transportation, Division of Research, Innovation and System Information, MS-83, P.O. Box 942873, Sacramento, CA 94273-0001.

Effect of Fines on Liquefaction Triggering Analyses

Varun N. S. Renugah

Arda Sahin

Scott J. Brandenberg

Jonathan P. Stewart

Department of Civil and Environmental Engineering
University of California, Los Angeles

Abstract

This report develops a new approach for implementing fines content corrections when evaluating soil liquefaction potential. Fines content influences both penetration resistance and cyclic resistance. In current fines content corrections, a single adjustment to penetration resistance is used to model both influences. This report separates the two influences by using variable rate cone penetration test data to evaluate the influence of fines content on cone penetration test (CPT) resistance, and cyclic laboratory test data to evaluate the influence of fines on cyclic resistance. The effect of fines is always to reduce penetration resistance. However, cyclic strength of soils can increase or decrease with increasing fines content depending on soil characteristics such as the state of the coarse fraction, the plasticity of the fines, and the degree of overconsolidation.

The influence of fines on drainage effects in CPT soundings is evaluated, the trends of which are used to develop a relationship between the measured cone tip resistance and the tip resistance that would be measured under drained loading conditions, using soil behavior type index as a conditioning variable. The resulting relationships allow penetration resistances measured under partially drained or undrained conditions (i.e., when variable amounts of fines are present) to be adjusted for equivalent drained conditions (i.e., the expected conditions for clean sands).

A methodology for evaluating cyclic strengths of soil mixtures with variable levels of fines is proposed that combines concepts from liquefaction triggering evaluation for clean sands (using penetration resistance) and cyclic failure evaluation for fine-grained soils (using material properties like plasticity index and overconsolidation ratio). The cyclic resistance of clean sands is evaluated using a laboratory-based model developed in the NGL project. The cyclic resistance of fine-grained soil is evaluated using a model developed in this report that extends prior results from literature using an extended database. The proposed model captures over-consolidation effects and the effects of variable levels of soil plasticity index. An interpolation function is provided to evaluate the cyclic strength for sands with intermediate levels of fines between those extremes.

The procedures for fines corrections to penetration resistance and cyclic strength analysis are applied to critical layer data from an existing CPT-based triggering model. The levels of adjustment from uncorrected penetration resistance-cyclic stress ratio data points are compared for the legacy models and proposed framework developed in this report. This report also evaluates whether alternative intensity measures provide predictive power beyond peak horizontal acceleration and magnitude, which are currently used in most triggering models. Preliminary findings are that alternative intensity measures do not provide enhancements when evaluated against field liquefaction data.

Keywords: Fines content, liquefaction triggering, cyclic softening, cyclic resistance ratio, cone penetration test

Acknowledgements and Disclaimer

This research study was funded by the California Department of Transportation (Caltrans), under Contract No. 65A0774. The opinions, findings, conclusions, and recommendations expressed in this publication are those of the author(s) and do not necessarily reflect the view of Caltrans, Pacific Earthquake Engineering Research (PEER) Center, or the Regents of the University of California. The authors would like to thank Sharon Yen, Kyungtae Kim, and Thomas Shantz at Caltrans for managing the contract, providing insightful technical comments during the project, and reviewing our project deliverables.

Contents

List of Tables

List of Figures

1 Introduction

Fines content (*FC*), defined as the percentage by mass of particles finer than 75μm, influences the mechanical properties of soil by altering its microstructure and state. This has been well established through extensive experimental investigations. Thevanayagam (2007) theorized that when fines are contained entirely within the void spaces between sand particles, they do not participate in the interparticle contact force chain, and the mechanical behavior of the soil is controlled by the coarse particles. As the fines content increases, some fraction of the fines become active contributors to the force-chain that was originally composed of only the coarse material, and the behavior of the soil is influenced by both the coarse and fine fractions. Further increasing *FC* gradually replaces coarse particle contacts with fines until the limiting fines content (FC_{th}) is reached. At this point, the fine fraction controls the behavior of the soil and the coarse particles are floating in a matrix of fines. The value of FC_{th} is generally around 20-40% (Cubrinovski and Ishihara 2002).

The mechanical properties of a clean sand are predominantly characterized by its state parameter (ξ) or relative density (D_R) (e.g., Bolton 1986), whereas over-consolidation ratio (*OCR*) and mineralogy (often represented by plasticity index, *PI*) control the mechanical behavior of fine-grained materials (Ladd 1991, Mitchell and Soga 2005). Figure 1.1 shows a coarse material with the stress transfer controlled by granular particles (Part a), fine-grained material with a combination of silt and clay particles (Part c), and a soil mixture with both coarse and fine particles (Part b). Secondary factors, such as age and fabric, influence cyclic strength across a range of *FC*. Sand-fine mixtures, as illustrated in Figure 1.1(b), exhibit characteristics of both. Relative density often cannot be measured for mixtures of sands and fines, particularly when the fine fraction consists of plastic clayey materials. Plasticity measurements are affected by the sand fraction that passes the #40 sieve. As such, *PI* for mixtures of sand and fines may not be representative of the fine-grained fraction of soils (Qamar et al. 2024).

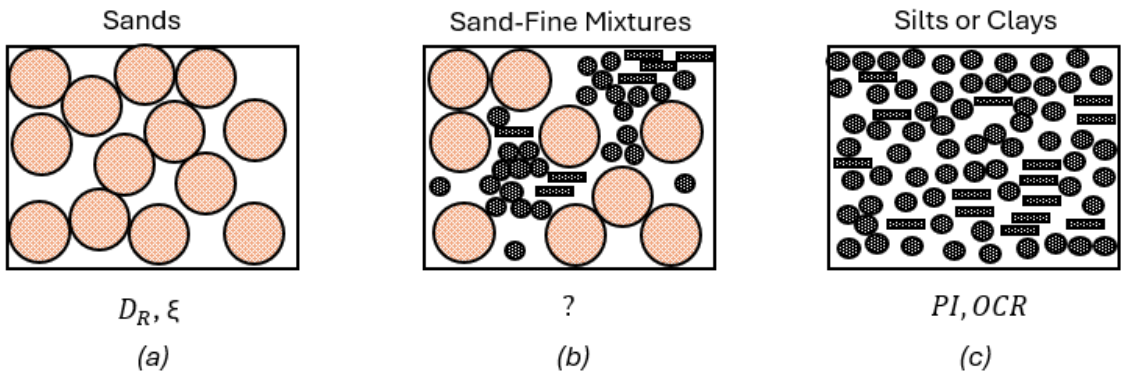

Figure 1.1 Parameters controlling the mechanical behavior of different soils.

The presence of fines also alters the gradation of the soil. Basson et al. (2024) have shown using the discrete element method (DEM) that the material's shear strength and dilation are increased with increasing coefficient of uniformity (C_U), which is affected by fines. Gradation has also been shown to influence the location and the slope of the critical state line (*CSL*) (Dash et al. 2010; Wei and Yang 2019; Yang et al. 2015).

1.1 Fines Content Corrections in Liquefaction Models

For a given penetration resistance, sands with fines have been shown to exhibit higher liquefaction resistance compared with clean sands. For example, Seed et al. (1983) interpreted liquefaction case histories based on overburden-corrected SPT blow count (N_1) vs. cyclic stress ratio (*CSR*) and proposed a curve separating cases where manifestation was and was not observed. They recommended adding 7.5 to the measured N_1 value for silty sands, which produces a fines-corrected SPT blow count that can be used with the boundary curve for clean sands. This is equivalent to shifting the boundary line for clean sands to the left by $\Delta N_1 = 7.5$ (Figure 1.2). As a result, for a given penetration resistance, silty sands exhibited a higher liquefaction resistance than clean sands. They supported their fines content adjustment based on field observations and laboratory tests by Japanese researchers (e.g., Tatsuoka et al. 1980, Tokimatsu and Yoshimi 1981) in which sands with fines were found to have higher liquefaction resistance than clean sands with the same penetration resistance. Furthermore, Zhou (1981) found that the cone penetration resistance of silty sands had to be increased to capture field observations during the 1976 Tangshan earthquake. Fines content corrections have been routinely applied in liquefaction triggering evaluation procedures since these early studies on the topic (e.g., Seed et al. 1985, Youd et al. 2001, Cetin et al. 2004, Moss et al. 2006, Boulanger and Idriss 2008, Cetin et al. 2018).

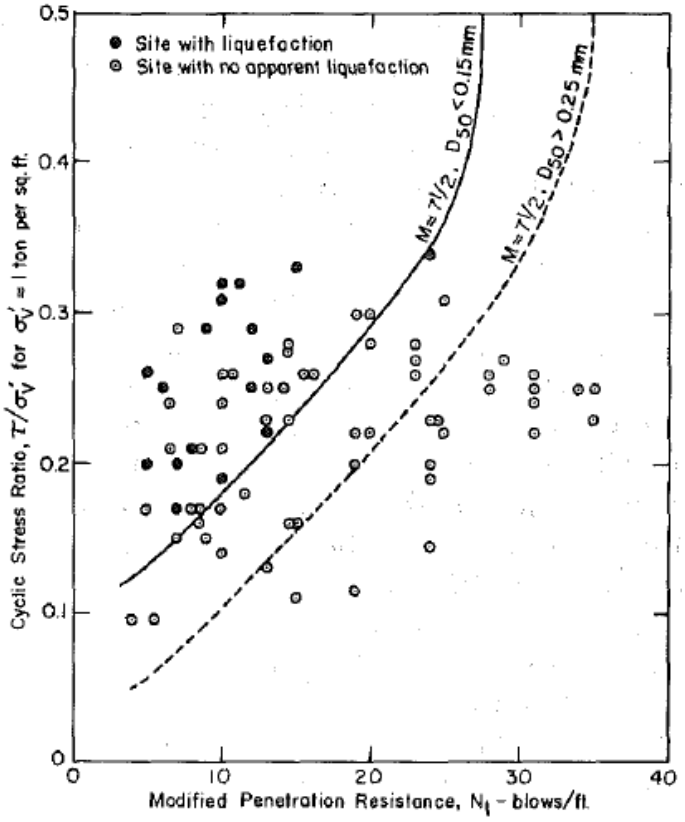

Figure 1.2 Correlation between field liquefaction behavior of silty sands (D50 < 0.15mm) and clean sands (D50 > 0.25 mm) (Seed et al. 1983)

Table 1.1 summarizes fines content corrections commonly used in liquefaction triggering evaluation procedures. Robertson and Wride (1998) proposed a multiplicative factor, K_c, applied to overburden-corrected cone penetration tip resistance, where K_c is defined as a function of soil behavior type index (I_c). Youd et al. (2001) recommended a fines correction consisting of an additive factor, α, and a multiplicative factor, β, both of which are functions of FC. Their fines correction has no influence on the measured penetration resistance for $FC < 5\%$ and is constant for $FC > 35\%$. Cetin et al. (2004) used Bayesian inference to regress a multiplicative fines content correction factor, C_{Fines}, that is applied to the overburden- and energy-corrected SPT blow count, $(N_1)_{60}$, where C_{Fines} is a function of $N_{1,60}$ and FC. Moss et al. (2006) used Bayesian inference from cone penetration test (CPT) field case histories to develop a factor, Δq_c, be added to the measured overburden-corrected cone tip resistance (q_{c1}) to account for the influence of fines, where Δq_c is a function of CSR and friction ratio, R_f. Idriss and Boulanger (2006, 2008, 2010) proposed an additive factor $\Delta N_{1,60}$ to be applied to the measured overburden- and energy-corrected SPT blow count, where $\Delta N_{1,60}$ is a function of FC. These relationships were updated as new field data was added to the dataset on which the model is developed. Boulanger and Idriss (2016) developed similar correction factors for cone penetration resistance, in which Δq_{c1N} is a function of FC and q_{c1N}. Cetin et al. (2018) used Bayesian inference to regress a $\Delta N_{1,60}$ that is a function of FC and $N_{1,60}$.

Table 1.1 Fines corrections in liquefaction triggering models.

Reference	Penetration	Applicability	Correction Factor
Seed et al. 1983	SPT	$D_{50} <$ 0.15 mm	$\Delta N_1 = 7.5$
Robertson and Wride 1998	CPT	$I_c < 2.6$	$(q_{c1N})_{cs} = K_c\, q_{c1N}$ $K_c = f(I_c)$
Youd et al. 2001	SPT	$0\% \le FC \le 35\%$	$N_{1,60,cs} = \alpha + \beta N_{1,60}$ $\alpha, \beta = f(FC)$
Cetin et al. 2004	SPT	$0\% \le FC \le 35\%$	$N_{1,60,CS} = N_{1,60}\, C_{Fines}$ $C_{Fines} = f(N_{1,60}, FC)$
Moss et al. 2006b	CPT	$0.5 \le R_f \le 5$	$q_{c1,mod} = q_{c1} + \Delta q_c$ $\Delta q_c = f(CSR, R_f)$
Idriss and Boulanger 2006, 2008, 2010	SPT	$0\% \le FC \le 60\%$	$N_{1,60,CS} = N_{1,60} + \Delta N_{1,60}$ $\Delta N1_{60} = f(FC)$
Boulanger and Idriss 2016	CPT	$0\% \le FC \le 100\%$	$q_{c1N,cs} = q_{c1N} + \Delta q_{c1N}$ $\Delta q_{c1N} = f(q_{c1N}, FC)$
Cetin et al. 2018	SPT	$0\% \le FC \le 35\%$	$N_{1,60,CS} = N_{1,60} + \Delta N_{1,60}$ $\Delta N_{1,60} = f(N_{1,60}, FC)$

Saye et al. (2021) proposed a "common origin" procedure to evaluate the cyclic resistance of soils based on CPT data using a soil classification index, ΔQ. They argue that ΔQ inherently captures factors such as mineralogy, grain shape, *OCR*, gradation, etc., negating the need for susceptibility assessment and fines-corrections. As such, their method does not include a fines correction, and therefore does not appear in Table 1.1, yet the method does inherently account for the influence of fines.

1.2 Separating Influence of Fines on Penetration Resistance and Cyclic Resistance

Fines influence both penetration resistance and liquefaction resistance. Fines influence hydraulic conductivity and compressibility, and therefore drainage conditions during penetration resistance tests. Whereas cone penetration is drained for clean sands, it transitions toward undrained behavior as fines are added. The influence of compressibility extends beyond its influence on drainage; more compressible soils exhibit lower penetration resistance due to elasto-plastic soil response. Fines also influence liquefaction resistance due to different interparticle contact chains for coarse grained vs. fines-dominant soil mixtures, particularly when fines fractions include particles with plastic mineralogy. The fines content corrections in Table 1.1 do not distinguish these effects but inherently capture them to the extent they are represented in case history databases.

For example, Youd et al. (2001) state:

> *"Whether this increase is caused by an increase of liquefaction resistance or a decrease of penetration resistance is not clear."*

Moss et al. (2006a) state:

> *"An index test measurement includes the effects of all the competing physical phenomena that occur as the measurement is required. Physical responses may be working in a constructive or destructive manner to produce the final measurement…The cumulative result is that an increase in friction ratio correlates with an increase in liquefaction resistance."*

A natural question is whether there is benefit in separating the influence of fines on penetration resistance from the influence of fines on cyclic resistance. This is the question that has guided the work presented in this report and that is illustrated schematically in Figure 1.3. According to this framework, the triggering curve is shifted to the left to account for the influence of fines on penetration resistance and is shifted either up or down to account for the influence of fines on cyclic resistance. By accounting for the horizontal and vertical effects separately, we provide a more conceptually robust framework that accounts for the range of possible effects in both directions.

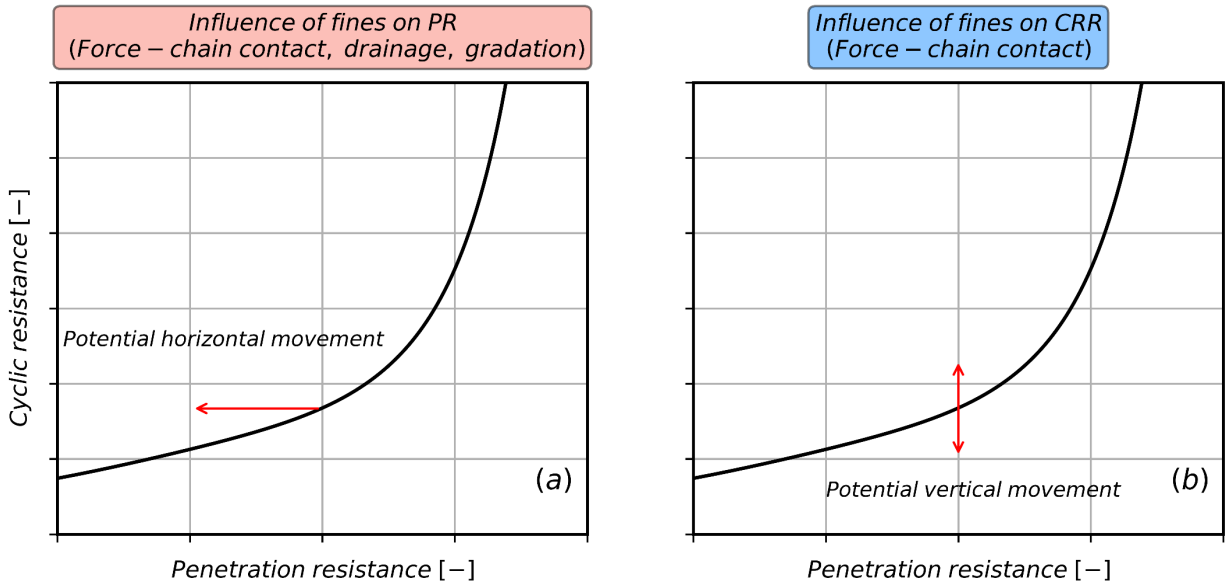

Figure 1.3 Influence of fines on the liquefaction triggering curve including (a) the influence on penetration resistance and (b) the influence on cyclic resistance.

1.3 Cyclic Strength of Fine-Grained Soil

When FC increases beyond FC_{th}, the fines fraction dominates soil behavior. Quantifying the cyclic resistance of fine-grained soils is therefore an important part of understanding fines content

corrections. Early liquefaction case histories were dominated by observations of manifestation of liquefaction of sands and a few silty sands (with $FC < 35\%$). As a result, early liquefaction models were developed for coarse-grained soils, with penetration resistance adjusted for *FC*. However, the 1999 Chi-Chi earthquake in Taiwan (Chu et al. 2004) and the 1999 Adapazarı earthquake in Turkey (Bray et al. 2004) produced ground failure case histories of liquefaction of silts and sandy silts with very high *FC*. This led to a shift in research priorities toward understanding the cyclic behavior of fine-grained materials. Research on cyclic strength of fine-grained soils is relevant to this report to the extent that fines corrections are often applied to fine-grained soils even though they are largely absent from the case history datasets from which the fines corrections were originally developed (i.e., fines corrections were generally developed for sands with fines).

Boulanger and Idriss (2006) postulated that fine-grained materials can be characterized as exhibiting sand-like behavior similar to clean sands, clay-like behavior similar to plastic clays, or intermediate behavior that exhibits characteristics of both sand-like and clay-like materials. They proposed that PI < 4 soils are sand-like, PI > 7 are clay-like, with intermediate soils lying between these limits. Furthermore, they suggest that cyclic resistance of sand-like fine-grained soils be evaluated using traditional liquefaction triggering evaluation procedures (with a fines-content adjustment applied to the measured penetration resistance), and that cyclic resistance of clay-like soils be evaluated using cyclic softening procedures that related cyclic strength to monotonic undrained shear strength. Bray and Sancio (2006) proposed a framework in which fine-grained soils were characterized as susceptible, not susceptible, or marginally susceptible based on plasticity characteristics and the ratio of water content to liquid limit. Boulanger and Idriss (2006) and Bray and Sancio (2006) both suggest that sampling and testing fine grained soils is the best way to assess their cyclic resistance.

1.4 Organization of this report

This report is divided into six chapters.

- **Chapter 2** focuses on the effects of fines on cyclic resistance ratio and develops a model for expressing cyclic resistance ratio, *CRR*, as a function of *FC*, D_R, *OCR*, and *PI*. The model unifies liquefaction triggering procedures that use penetration resistance, and cyclic failure assessment procedures for fine-grained soils, and uses an interpolation function to bridge between clean sands and fine-grained soils as a function of *FC*.

- **Chapter 3** focuses on the effect of fines on penetration resistance and uses variable-rate cone penetration tests data from literature to develop a model to account for the effects of drainage during penetration. The drained penetration resistance obtained from the correction is proposed as the value used for liquefaction triggering evaluation procedures. Some insights regarding penetration resistance and compressibility are provided.

- **Chapter 4** exercises the proposed models for the influence of fines on *CRR* and penetration resistance developed in Chapters 2 and 3 and compares them with existing fines content corrections.

- **Chapter 5** explores the use of alternative intensity measures, including Arias intensity, cumulative absolute velocity, and peak ground velocity in evaluation of liquefaction triggering and manifestation.
- **Chapter 6** provides conclusions and recommendations.

2 Effect on Fines on Cyclic Resistance

2.1 Overview

The addition of fines to sand affects the mechanical properties of the mixture by altering the microstructure and the state of the soil. In this chapter, we investigate the influence of fines on cyclic resistance of soil.

The effects of fines on *CRR* is a complex problem since a parameter related to density or packing of particles is generally held constant as *FC* changes, but the parameters available for baselining these comparisons have limited ranges of applicability. The parameter that is most often held constant across ranges of *FC*s to investigate their effects on cyclic strength is D_R, despite the difficulty of measuring D_R for fine-grained soils or sands that are fines-dominated, particularly when the fines are plastic. Figure 2.1 summarizes the findings of various studies that were performed at a constant D_R for relatively non-plastic fines ($PI < 5$). Cyclic resistance ratios (*CRR*s) at different *FC*s are compared relative to the *CRR* for clean sands. At a constant D_R, Polito and Martin (2001) and Boominathan et al. (2010) found that *CRR* decreases as *FC* increases. This finding is supported by experiments by Belkhatir et al. (2010), Chen et al. (2020), Cubrinovski et al. (2010), Huang et al. (2004), Oka et al. (2018), Hu et al. (2024) and Rangaswamy et al. (2010). In contrast, Amini and Qi (2000) found that *CRR* increases as *FC* increases. Furthermore, Cheng and Zhang (2024) showed that *CRR* decreases until a threshold *FC* is reached and then increases for *FC* greater than this threshold *FC*, whereas Carraro et al. (2003) and El-Mamlouk et al. (2007) noted an initial increase followed by a decrease in *CRR*. Consistent with the range of findings summarized here, Gobbi et al. (2022), Gu et al. (2024) and Monkul et al. (2021) showed that the *CRR* may increase with *FC* increases for high D_R and decrease for low D_R.

A factor that influences the effects of fines on *CRR* is the impact of *FC* on the position of the critical state line (Dash et al. 2010; Wei and Yang 2019; Yang et al. 2015). As an alternative to D_R, an index parameter developed to facilitate comparisons across *FC*s for non-plastic fines is the inter-granular void ratio (e_s), which treats the space occupied by the fines as a part of the void space. This was extended by Thevanayagam (2007) to an equivalent inter-fine void ratio $(e_f)_{eq}$ and equivalent inter-granular void ratio $(e_c)_{eq}$ which give a better representation of the state of the soil by relating them with the property of the host sand, fine particles and the relative amount of fines present. However, these parameters require extensive lab testing and have not been widely used in studies of fines effects on *CRR*. Furthermore, they are intended for gap-graded blends of sand and fines, and are not readily applicable to well-graded soils. Depending on the choice of the index parameter to hold constant as *FC* changes, the effects of non-plastic fines on *CRR* can vary drastically. For fines having plasticity, Ishihara (1993) found that they often increase the cyclic resistance of the host sand due to the adhesion between the fines and coarse-grained particles.

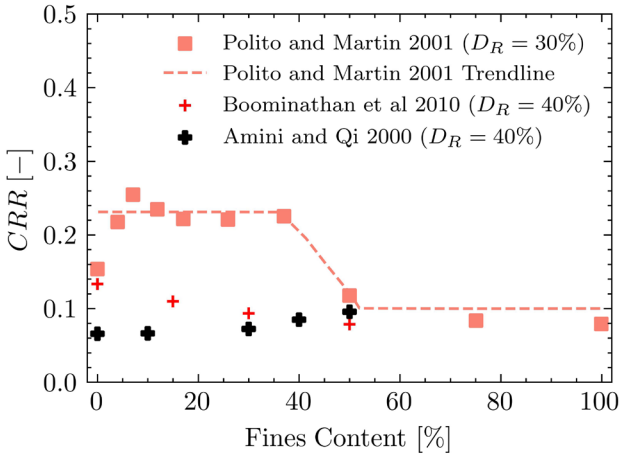

Figure 2.1 Effect of non-plastic and low-plasticity fines (*PI*<5) on *CRR* in studies performed at constant D_R.

We posit that the following factors may have influenced the diverse conclusions that are reported in literature:

1. The addition of fines to a clean sand changes the extreme void ratios e_{min} and e_{max}, which creates difficulties maintaining a constant D_R for the mixture as *FC* changes. For example, Amini and Qi (2000) had a target D_R of 40% but the tested samples had D_R in the range of 34% to 44%. Similar observations are seen in most of the studies. As a consequence, changes in *CRR* as *FC* changes are also influenced by unintended changes in D_R, which complicate the interpretation of results.

2. The studies used materials at various *FC*s. The absence of consistent *FCs* across studies complicates cross-study comparisons of results. For instance, local peaks observed in some studies at *FC* = 5-10% may not occur in other studies due to lack of data in this range.

3. The effect of fines on *CRR* may be different for different levels of relative density. This has been described as a "crossing-effect" by Monkul and Tütüncü (2024). In particular, they found that *CRR* may decrease with *FC* for materials with D_R < 45% and increase with *FC* for D_R > 45% materials. The trend may also reverse depending on the properties of sand and fines.

4. The overconsolidation ratio (*OCR*) and *PI* of the fine fraction may influence *CRR* as *FC* increases, but *OCR* and *PI* are generally not considered in fines corrections.

In order to develop recommendations in the face of these ambiguities, we have gathered available data from the literature with the aim of formulating a unifying conceptual framework to reconcile the complex effects seen in literature.

2.2 Database and Data Processing

This section presents the data used to train the model. We first present data from Carlton et al. (2023), which was compiled to investigate overburden stress correction factors and static shear stress correction factors. We then discuss additional data that were compiled from literature as part of this study. These datasets span a broad range of soil types, ranging from clean sands to plastic clays. We then present our methodological framework, which requires *CRR* to be computed separately for clean sands and fine-grained soils. Accordingly, we present separate models for clean sand (from existing literature), and for fine-grained soils (derived herein).

2.2.1 Data from Carlton et al. (2023)

A significant amount of the data assembled for this study were originally compiled by Carlton et al. (2023) to investigate overburden stress correction factors (K_σ) and initial static shear stress correction factors (K_α). This was part of a supporting study for the Next Generation Liquefaction (*NGL*) project. The data from Carlton et al. (2023) included laboratory test data of undisturbed, frozen and reconstituted specimens, which were tested using cyclic triaxial devices (*CTX*), cyclic direct simple shear devices (*CDSS*), and cyclic torsional devices (*CTS*). The overburden and static shear stress correction factors were evaluated by the authors using the laboratory test results that were available from the corresponding original papers. Subsequently, they corrected the lab data to equivalent field stress conditions as per Montgomery et al. (2014). The dataset from Carlton et al. (2023) consists of 960 *CRR* values, 231 K_σ values and 326 K_α values from 331 CDSS tests, 561 CTX tests and 58 CTS tests.

2.2.2 Additional Data

We gathered additional laboratory test data from studies that were performed specifically to investigate the influence of fines on *CRR*. The resulting dataset is mostly based on reconstituted samples that were prepared in the laboratory using pluviation, tamping, and depositional methods. Some of the data were available in a tabulated form in the original paper whereas others required manual digitization of the *CSR* vs. *N* curves provided in figures. A couple of studies that performed cyclic testing on intact/reconstituted specimens with very high *FC*s were also gathered. These tests were performed at different effective confining stresses based on the depth from which the samples were gathered and to maintain the required *OCR*.

The data sources for the present study are as follows: Tütüncü et al. (2022), Ecemis et al. (2022), Cheng and Zang (2024), Boominathan et al. (2010), Rangaswamy et al. (2010), Amini and Qi (2000), Cubrinovski et al. (2010), Polito and Martin II (2001), Carraro et al. (2003), Oka et al. (2018), Belkhatir et al. (2010), Gobbi et al. (2022), Chen et al. (2020), Monkul et al. (2021), El-Mamlouk et al. (2007), Gu et al. (2024), Huang et al. (2004), Papadopoulou and Tika (2021), Dickenson et al. (2021), Preciado Reyes (2021), Dadashiserej et al. (2024), Dahl (2011), Soysa (2015), Sanin (2010), Verma and Wijewickreme (2018), Dadashiserej et al. (2023), Verma (2019), Eslami (2017), Tom (2011), Reid and Fourie (2017) and Price et al. (2015).

The gathered data was processed as described in Section 2.2.3 to obtain CRR_{std}, where CRR_{std} is the *CRR* corrected for magnitude, overburden, initial static shear stress, field conditions, test type and specimen type. The processed data from Carlton et al. (2023) consisted of 707 (CRR_{std}, D_R, *FC*) points and 51 (CRR_{std}, *FC*) points. The data were derived from 403 cyclic triaxial tests, 297 cyclic direct simple shear tests and 58 cyclic torsional tests. Processing the additional study data resulted in 324 (CRR_{std}, D_R, *FC*) data points, and 126 (CRR_{std}, *FC*) data points. These 450 data points are based on both *CTX* tests (264) and *CDSS* tests (186). The data include test specimens prepared by various specimen preparation methods: dry deposition, dry and moist tamped, under-compacted, slurry deposited, or intact. The *FC* range across the dataset is 0 to 100%, D_R ranges from 0 to 100%, initial vertical effective stresses (σ_{vc}') ranges from 9.8 to 1471 kPa, *PI* ranges from 0 to 73, and CRR_{std} ranges from 0.03 to 1.58. It is important to note that D_R is often not reported for materials with high fines content, due to the difficulties in measuring the extreme void ratios. Figure 2.2 shows distributions of the data with respect to D_R, *FC*, σ_{vc}', *PI* and CRR_{std}.

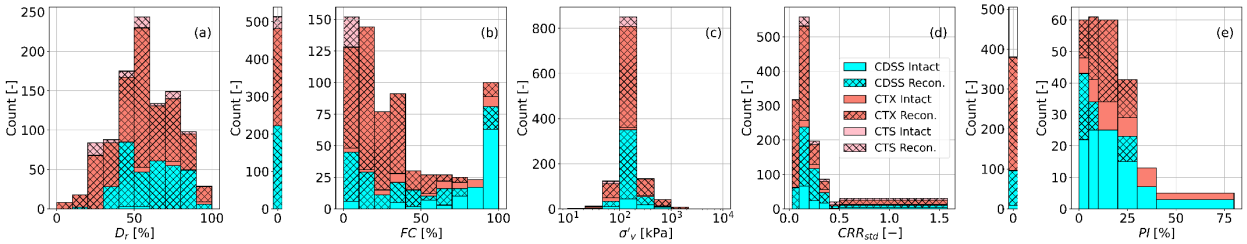

Figure 2.2 Distributions of D_R, *FC*, σ_v', CRR_{std} and *PI* in the dataset, aggregated by test type and specimen type (reconstituted or intact).

2.2.3 Data Processing

Each of the studies in the compiled database used a different type of cyclic testing (*CDSS* or *CTX* or *CTS*), had different cyclic failure criteria, had different overburden and initial static shear stress conditions, and reported the cyclic resistances (CRR_{lab}) for different reference number of cycles (N_{ref}). Moreover, laboratory data does not accurately represent the behavior of soil in the field due to different levels of stress anisotropy. Hence, we performed additional data processing to account for these effects, the results of which are corrected cyclic resistance values $CRR_{M=7.5,\ \sigma'v=1atm,\ \alpha=0}$ (hereafter CRR_{std}) that are consistent across datasets. Corrections followed the steps below.

1. **Correction for N_{ref}:** The cyclic resistance of soil depends on the number of loading cycles. The relationship between *CSR* and *N* to trigger liquefaction is often expressed by a power law Equation (2.1)

$$CSR = aN^{-b} \tag{2.1}$$

where *a* and *b* are regressed from the experimental data (*CSR* – *N* points). For the cases where *b* could not be regressed from the data, it was assumed as 0.3. For the current study, N_{ref}=15 cycles was used corresponding to a **M**7.5 earthquake event for sands as per Idriss

and Boulanger (2008). Further information on the regression of b values in this study is provided in Section 2.4.4.

2. **Overburden correction (K_σ):** An overburden correction factor (K_σ) was used to account for the dependence of *CRR* on the effective confining stress (σ'_v) due to the reduction in dilatancy as σ'_v increases. For coarse-dominated materials, K_σ was evaluated using the relationship by Carlton et al. (2025). For fines-dominated materials, we applied K_σ = 1.0 (Boulanger and Idriss 2007; Wijewickreme and Soysa 2019). More recent studies by Dadashiserej et al. (2023) have shown that consolidation pressure has multiple effects on silty materials: reduction in *OCR*, yielding of the soil fabric, and reduction in void ratio, which may not be uniquely represented by a K_σ. A detailed analysis of overburden effects for fine-grained materials is presented in Section 2.4.1, which provides evidence to support the assumptions noted above.

3. **Static shear stress correction (K_α):** Initial static shear stress correction factor (K_α) was used to account for the dependence of *CRR* on the initial static shear stress ratio (α). Materials with a non-zero α can exhibit a higher or lower *CRR* depending on state. Most of the gathered data had an associated K_α in the original study based on experimental results, in which case those results were directly used for correcting the reported CRR_{lab}. To increase the amount of data available, whenever K_α was not available, it was approximated as 1 when α was within the range of 0 to 0.02 for *CDSS* tests and when the anisotropic consolidation ratio (K_c) was in the range 0.89 to 1.11 for *CTX* tests. The data points which did not meet these criteria were screened out of consideration.

4. **Field stress corrections:** Ishihara et al. (1985) demonstrated the influence of consolidation conditions on the measured cyclic resistance using cyclic torsional tests performed at various K_o values. Corrections per Montgomery et al. (2014) were applied to account for differences in consolidation conditions in the field relative to the lab, and for multi-dimensional shaking in the field. The K_o correction is intended to account for the influence of anisotropic consolidation conditions on mean effective stress. These corrections assume that cyclic strength is a function of mean effective stress rather than vertical effective stress.

5. **Test type correction (K_t)**: Using experimental data, Boulanger (2003) found that the cyclic resistance measured from *CTX* tests are higher than *CDSS* tests. In order to account for this, we used correction factors from Ulmer et al. (2024) to convert the *CTX* results to equivalent *CDSS* values. For fines-dominated material (*FC*>=35%), we have converted the *CTX* values to equivalent *CDSS* as per Bray and Sancio (2006) with K_t =0.8 for *CTX*-based tests and K_t=1 for *CDSS* based.

6. **Specimen type correction (K_s)**: Ulmer et al. (2024) developed corrections for specimen preparation method that are a function of D_R. Their specimen type correction factors were directly applied for the coarse-grained materials in our database. A similar correction factor for fine-grained materials is derived in Section 2.4.4.

The above-mentioned corrections were used to compute the corrected cyclic resistance using Equation (2.2).

$$CRR_{std} = \frac{CRR_{lab}}{K_\sigma K_\alpha} \cdot K_t \cdot K_s \cdot C_{2D} \cdot \left(\frac{N_{lab}}{15}\right)^b \left(\frac{1+2(K_o)_{field}}{1+2(K_o)_{lab}}\right) \quad (2.2)$$

where C_{2D} accounts for the multi-dimensional shaking in the field. C_{2D} is 0.9 for coarse-grained materials (Seed 1979), 0.96 for clays (Boulanger and Idriss 2007) and intermediate soils have values between 0.9 and 0.96 (Dahl 2011). We have used C_{2D}=0.9 for coarse-grained materials and 0.96 for fine-grained materials ($FC \geq 35\%$). $(K_o)_{field}$ and $(K_o)_{lab}$ are the coefficients of lateral earth pressure in the field and the lab respectively.

2.2.4 Observations and proposed framework

Figure 2.3 shows variations of CRR_{std} values with FC for conditions in which CRR decreases (Figure 2.3a,c) and increases (Figure 2.3b,d) as FC increases. The decreasing case involves relatively dense sands (D_R = 70%) and normally-consolidated fine-grained soils for $PI \leq 4$ (Figure 2.3a) and $4 < PI \leq 15$ (Figure 2.3c). The increasing case involves relatively loose sands (D_R = 30%) and over-consolidated fine-grained soils with OCR = 2 for $PI \leq 4$ (Figure 2.3b) and $4 < PI \leq 15$ (Figure 2.3d).

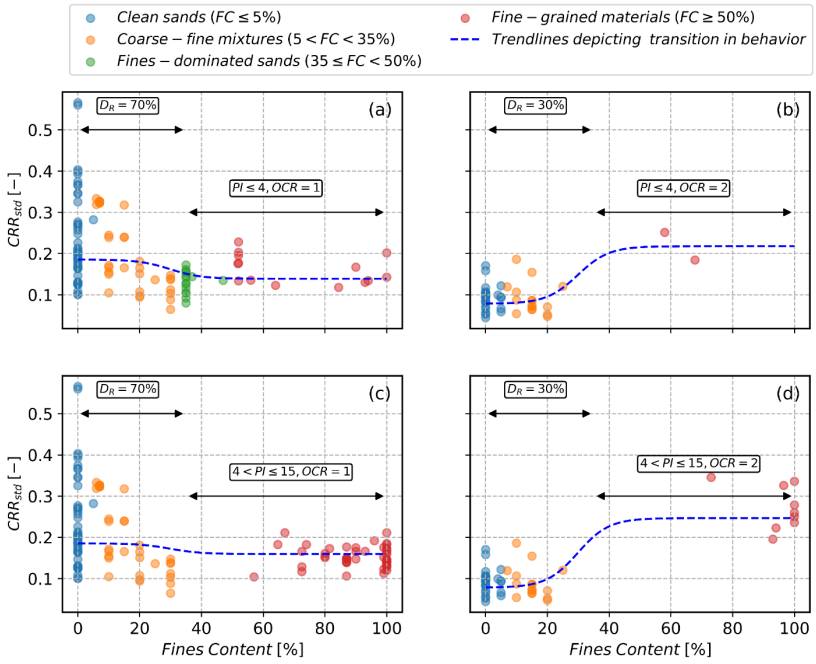

Figure 2.3 Observed trend in CRR_{std} with FC for a) clean sands and coarse-fine mixtures with D_R = 70% and normally consolidated fine grain materials with $PI \leq 4$ b) clean sands and coarse-fine mixtures with D_R = 30%, and fine grain materials with OCR = 2 and $PI \leq 4$ c) clean sands and coarse-fine mixtures with D_R = 70% and normally consolidated fine grain materials with $PI \in (4,15]$ b) clean sands and coarse-fine mixtures with D_R = 30%, and fine grain materials with OCR = 2 and $PI \in (4,15]$.

The dashed curves in the figures show transition functions which depict the shift in cyclic resistance as *FC* increases. This would essentially mean that the extremities of this curve are controlled by the properties of coarse and fine particles, respectively, with the intermediate values interpolated between the extremes as a function of *FC*.

For clean sands (*FC* ≤ 5%), the measured cyclic resistance can be taken solely as a property of the coarse-grained materials, i.e. $CRR_{std}^{s} = f(D_R)$, whereas at high *FC* the cyclic resistance can be taken as a function of *OCR*, *PI*, and/or s_u i.e. $CRR_{std}^{f} = f(OCR, PI, s_u)$. For intermediate *FC*s, where the soil is influenced by both coarse and fine particles, we hypothesize that the cyclic strength can be expressed as a linear combination of CRR_{std}^{s} and CRR_{std}^{f} conditioned on *FC* using a logistic interpolation function with γ_o and γ_1 as regression constants, as indicated by Equation (2.3).

$$CRR_{std} = CRR_{std}^{f} + \frac{CRR_{std}^{s} - CRR_{std}^{f}}{1 + e^{\gamma_o (FC - \gamma_1)}} \tag{2.3}$$

CRR_{std}^{s} can be computed using existing $q_{c1n,cs}$ - D_R correlations as per Boulanger and Idriss (2016) or more recent works from the NGL project (Ulmer et al. 2024). The CRR_{std}^{f} model can be developed by relating the cyclic strength with undrained monotonic strength of the material. Referred to as *cyclic softening* in literature, such procedures have been presented by Boulanger and Idriss (2007) and Dahl et al. (2018). Dadashiserej et al. (2024) provide a cyclic failure assessment method using *PI* and *OCR* for translational silts. By relating the CRR_{std} of the mixture with CRR_{std}^{s} and CRR_{std}^{f}, the framework has the potential to resolve the conflicting results in the literature. In the subsequent sections of this chapter, cyclic resistance models for coarse and fine grained materials are obtained followed by a regression to evaluate that define the transfer function as per Equation (2.3).

Equation (2.3) requires evaluation of both CRR_{std}^{s} and CRR_{std}^{f} regardless of *FC*, with weights being essentially unity for CRR_{std}^{s} when *FC* is low, and weights being essentially unity for CRR_{std}^{f} when *FC* is high. Mathematically, the procedure requires calculation of CRR_{std}^{s} for fine-grained soil, and CRR_{std}^{f} for clean sands. This results in counter-intuitive calculations that would generally not be performed when a clean sand or fine-grained soil are evaluated in isolation. However, the weighting function implied by Equation (2.3) renders the counter-intuitive calculations essentially moot while permitting a continuous interpolation of *CRR* for soils with *FC* that is intermediate between clean sand and fine-grained soil.

2.3 Cyclic Resistance Model for Coarse-Grained Materials

The value of CRR_{std}^{s} can be derived from any triggering or manifestation model applicable to clean sands. We use two different models in this report. One developed as part of the Next Generation Liquefaction (NGL) project by Ulmer et al. (2024), and the cone penetration based model by Boulanger and Idriss (2016). The latter is used in Chapter 4 to compare our fines content correction framework with their critical layer data.

The NGL triggering model is based on laboratory test data, and differs from field-based models that are conditioned on observations of liquefaction manifestation or lack thereof. It is possible for a soil to trigger without manifesting, therefore the NGL model tends to be lower than field-based manifestation models. To develop the model, Ulmer et al. (2024) gathered a dataset of cyclic laboratory tests on reconstituted and intact samples using direct simple shear and triaxial compression stress paths. The dataset is dominated by clean sands, with over 75% of the samples having $FC = 0$, and 94% of the samples having $FC \leq 5\%$. Although FC in their dataset was as high as 20%, the representation of high fines materials prevented development of a fines content correction in their study. This report supplements the NGL dataset with tests on higher fines materials, and therefore has considerable overlap with data used to develop the NGL model.

The NGL model was developed using a Bayesian approach in PyMC (Abril-Pla et al. 2023) to establish a relationship between CRR^{s}_{std} and relative density D_R of sands. The CRR model is given in Equation (2.4),

$$CRR^{s}_{std} = (2.88 - 0.0057{D_R}^{1.226} - 0.237\epsilon_s)^{-2.769} \quad (2.4)$$

where ϵ_s denotes the number of standard deviations about the median. The superscript s in CRR^{s}_{std} indicates that the model corresponds to clean sands. Furthermore, the NGL triggering model provides correction factors for stress path and sample type, with the relationship in Eq. 2.4 representing the direct simple shear stress path, and frozen sampling conditions. The NGL triggering model and data is presented in Fig. 2.4, along with a subset the new data added for this study corresponding to FC<25%. The NGL triggering model fits the new data reasonably well, though the new data appears slightly lower at D_R = 80%.

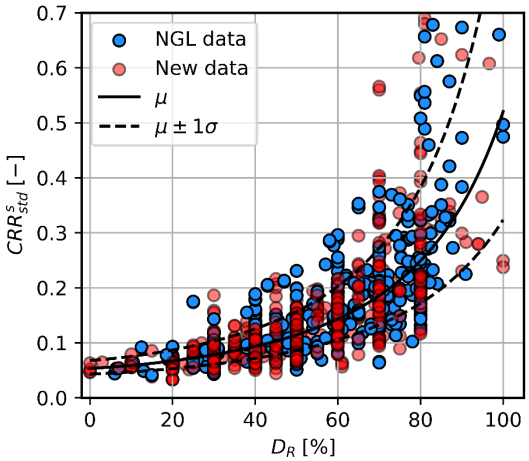

Figure 2.4 CRR^{s}_{std} vs. D_R for coarse-grained materials along with NGL triggering model predictions.

2.4 Cyclic Resistance Model for Fine-Grained Materials

The Unified Soil Classification System classifies soil as fine-grained if the percentage passing through the No. 200 Sieve is greater than 50%. However, silty sands become dominated by the fines fraction at significantly lower values that is better represented by the FC_{th} of soils that defines a condition where the amount of fines is great enough that coarse particles are mainly separated via a fines matrix, which largely controls the soil's shear behavior (Thevanayagam 2007; Castro et al. 2023). FC_{th} depends on multiple parameters including disparity ratio (defined as $R_d=D_{50}/d_{50}$ where D_{50}, d_{50} are the mean particle sizes of sand and fines respectively), fines plasticity, and gradation (Thevanayagam 2007). Experience suggests that it is generally within the range of 20-40% (Cubrinovski and Ishihara 2002). We defined a material as exhibiting fine-grained behavior if $FC \geq 35\%$ irrespective of the material's plasticity. The cyclic strength of such fine-grained soils is better characterized by *PI* and *OCR*. At $FC < 5\%$, the soil is assumed to be clean sand. In the intermediate zone between 5% and 35% soil properties are influenced by both the coarse and fines components of the soil matrix.

This section focuses on characterization of CRR_{std}^{f}, which represents the cyclic strength of fine-grained soils. Existing models to evaluate the cyclic resistance of clay-like fine-grained materials (Boulanger and Idriss 2007; Dahl 2011) use monotonic shear strength of the material and *OCR* as inputs. Recent works by Dadashiserej (2024) provides a model of evaluating the cyclic strength of intermediate fine-grained materials using the *OCR*, *PI* for a particular reference shear strain and number of cycles. In the following subsections, we use the compiled database to investigate a series of individual effects that are needed to formulate a CRR_{std}^{f} model for fine-grained materials. We also use the compiled dataset to revisit the cyclic softening type approach for clay-like fine-grained materials.

2.4.1 Effect of Overburden Stresses

In liquefaction analyses, an overburden correction factor (K_σ) is used to account for the dependence of *CRR* on vertical consolidation stress (σ'_{vc}) due to soil becoming less dilative (or more contractive) as σ'_{vc} increases. Existing models in literature are available to evaluate K_σ for sands as a function of D_R and σ'_{vc}. In contrast, the cyclic strength of clay-like soils is often assumed to normalize by s_u which scales linearly with σ'_{vc} for constant *OCR*. If the normalization holds, cyclic strength would also scale linearly with σ'_{vc}, meaning that $K_\sigma = 1.0$. However, few studies have been conducted to verify this assumption. Furthermore, the monotonic strength of silty soils does not necessarily normalize with σ'_{vc}, and the influence on K_σ is therefore unclear.

Montgomery et al. (2014) indicated that K_σ should account solely for the influence of σ'_{vc} on *CRR*, with all other factors including D_R and *OCR* held constant. Because *OCR* decreases as σ'_{vc} increases for overconsolidated soils, a K_σ relationship derived from testing of overconsolidated soils will be artificially steep for consolidation stresses less than the maximum past pressure (Montgomery et al. 2014; Carlton et al. 2025). Carlton et al. (2025) demonstrated these features in plots showing that frozen samples and tamped reconstituted specimens (i.e., specimens with *OCR*

> 1) exhibited stronger K_σ trends than pluviated and tube samples of sand (with *OCR* = 1). Their K_σ model was formulated for sands at constant *OCR* and therefore exhibited smaller K_σ effects (i.e., K_σ differing from 1.0 by lesser amounts) than prior models. Qualitatively similar results are evident from testing of intact low and moderate plasticity silt specimens from the Pacific Northwest by Dadashiserej et al. (2023).

This section of the report presents a qualitative assessment of K_σ for normally consolidated fine-grained soils from a subset of the gathered database consisting of CDSS and CTX tests on soils with plasticity index (*PI)* ranging from 0 to 36.5, *FC* ranging from 35% to 100%, and σ'_{vc} ranging from 86 to 1,000 kPa. A summary of the studies and the observed effects of overburden stresses is provided in Table 2.1.

Table 2.1 Summary of the data gathered from various studies and the observed effect of overburden stress on *CRR*.

Study	Soil	PI [%]	Range of σ'_{vc} [kPa]	Observed Trend in *CRR*	OCR	Test Type	Max. strain[1] [%]	Range of e_c [-]
Seed et al. (1973)	Lower San Fernando Dam – Hydraulic Fill	NP	100 to 300	Decreases	1	CTX	4 to 10	NA[2]
Al Tarhouni et al. (2011)	Gold Tailings	2.5	100 to 800	Almost Unaffected	1	CDSS	12 to 13	0.544 to 0.548
Sanin (2010)	Fraser River Delta Silt	4.1	86 to 400	Almost Unaffected	1 to 1.4	CDSS	15	0.818 to 0.990
Suazo et al. (2016)	Silver–Lead–Zinc tailings	4	100 to 800	Increases	1	CDSS	N/A[3]	0.510 to 0.746
Soysa (2015)	Site JS	7	100 to 200	Increases	1	CDSS	21 to 22	0.88 to 1.33
Verma and Wijewickreme (2018)	Fraser Silt – Site A	8.5	400 to 1,000	Decreases	1	CDSS	20	0.57 to 0.89
Verma (2019)	Fraser Silt – Site B	36.5	400 to 1,000	Decreases	1	CDSS	20	0.79 to 1.24
Dahl (2011)	Stratum B – Potrero Canyon	NP	225 to 450	Increases	1	CDSS	N/A	0.51 to 0.63
Dadashiserej et al. (2023)	Site E - Reconstituted	21	100 to 600	Decreases	1	CDSS	N/A	0.56 to 1.04
Dadashiserej et al. (2023)	Site F - Reconstituted	4	100 to 600	Decreases	1	CDSS	N/A	0.44 to 0.54

1. [1]Axial strain for *CTX* and shear strain for *CDSS* during monotonic shear tests, [2]NA – Data is not available
2. [3]N/A: Not applicable

The CRR^*_{std} values used in these plots and elsewhere in this section are modified from CRR_{std} values provided by Equation (2.2) by removing the K_σ correction and referencing *CRR* to 30 cycles instead of 15 cycles. Figure 2.5 shows trends of CRR^*_{std} with σ'_{vc} for test results from three groups of studies that have different trends. While these plots do not show K_σ directly, variations of CRR^*_{std} with σ'_{vc} represent the K_σ effect. The first group of test data (Figure 2.5a) show a flat trend of CRR^*_{std} with σ'_{vc}, implying K_σ =1.0. The second and third groups show an increasing trend

(implying K_σ>1.0 for σ'_{vc}>p_a; Figure 2.5b) and decreasing trend (K_σ<1.0 for σ'_{vc}>p_a; Figure 2.5c), respectively.

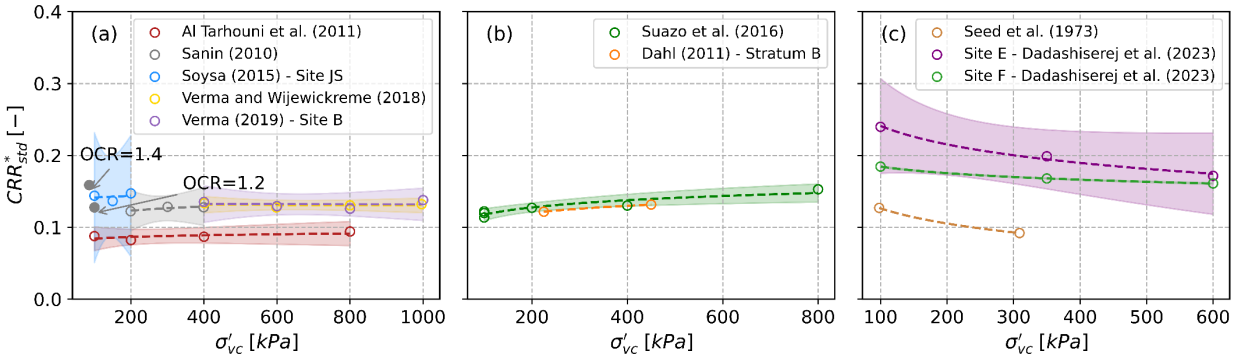

Figure 2.5 Observed effect of overburden stress on cyclic strength: (a) unaffected by σ'_{vc} (case i), (b) increases with σ'_{vc} (case ii), and (c) decreases with σ'_{vc} (case iii).

To facilitate conceptual understanding of the different trends in Figure 2.5, let us assume that the normal consolidation line (NCL) and CSL can be represented by semi-logarithmic lines. The lines can exist in any of the three possible configurations, as shown in Figure 2.6a: i) NCL and CSL are parallel, ii) NCL is steeper than CSL, and iii) NCL is flatter than CSL. For case i), the monotonic undrained strength at critical state ($s_{u,cs}$) normalized by the initial mean effective stress (p'_0) is constant for normally consolidated (NC) specimens, which can be represented as:

$$\frac{s_{u,cs}}{p'_0} = \frac{M_c}{2} \cdot exp\left(\frac{e_{0,CSL}-e_{0,NCL}}{\lambda_{CSL}}\right) = S \tag{2.5}$$

where M_c is the slope of the failure envelope in the mean effective stress (p') – deviatoric stress (q) plane, λ_{CSL} and λ_{NCL} are the slopes of the CSL and NCL in the e vs. $log(p'/p_a)$ plane, respectively, p_a is atmospheric pressure and $e_{0,CSL}$ and $e_{0,NCL}$ are the intercepts at p'=100 kPa. Fig. 2.5(c) illustrates that soils often exhibit a peak that is higher than the critical state strength. Furthermore, laboratory devices typically cannot impose high enough strains to reach a critical state. For the purpose of developing a framework for understanding how the slopes of the CSL and NCL relate to K_σ, we use critical state monotonic strengths herein, recognizing that typical definitions of s_u generally correspond to peak. A similar expression to Eq. (2.5) was presented in Eq. 6.26 of Kramer and Stewart (2025) using effective vertical stress (σ'_{v0}) as the normalizing stress:

$$\frac{s_{u,cs}}{\sigma'_{v0}} = \frac{2 \cdot 10^{\frac{e_{0,CSL}-e_{0,NCL}}{C_c}}}{1+K_o} \cdot \tan\varphi'_{cs} = S \tag{2.6}$$

where C_c is the compression index, K_o is the at-rest lateral earth pressure, φ'_{cs} is the effective stress friction angle at critical state.

For this report, we adopt Eq. (2.5), which uses mean effective stress for normalization, since it closely represents the state of the soil in critical state mechanics. If cyclic strength is proportional

to monotonic strength, the normalized cyclic strength would not vary with the initial mean effective stress p'_0, meaning that $K_\sigma = 1$.

Using a similar approach for cases ii) and iii), i.e., when the lines are not parallel, the monotonic undrained strength ratio of the material for normally consolidated conditions can be expressed as:

$$\frac{s_{u,cs}}{p'_0} = \frac{M_c \cdot (p'_0/p_a)^{\frac{\lambda_{NCL}}{\lambda_{CSL}}-1}}{2} \cdot \exp\left(\frac{e_{0,CSL}-e_{0,NCL}}{\lambda_{CSL}}\right) = S \cdot \left(\frac{p'_0}{p_a}\right)^{\frac{\lambda_{NCL}}{\lambda_{CSL}}-1} = S \cdot K_\sigma \qquad (2.7)$$

Equation (2.7) shows that when the NCL and CSL are not parallel, the normalized undrained strength depends on p'_0. If cyclic strength is proportional to monotonic strength, this implies a K_σ relationship that is not unity. For case ii) when $\lambda_{NCL} > \lambda_{CSL}$, the undrained strength ratio of the material is directly proportional to p'_0 raised to the power of a positive constant, and the undrained strength ratio increases with increasing p'_0 as shown in Figure 2.6b. Conversely, for case iii) when $\lambda_{NCL} < \lambda_{CSL}$, the undrained strength ratio decreases with increasing p'_0. The effective stress paths of specimens A, B and C, which have the same void ratio, under monotonic undrained loading are shown in Figure 2.6c as they approach steady state point D. The dilatancy of the specimens would be in the order B > A > C which explains the associated pore pressure generation during undrained shearing. The corresponding trend in $s_{u,cs}/p'_0$, as derived using Equations (2.5) and (2.7) is shown in Figure 2.6b for an assumed constant $\tau_{cyc}/s_{u,cs}$. It is interesting to note that the K_σ trend depends on the relative slopes of the CSL and NCL, which provides useful context for interpreting trends reported in the literature regarding the overburden effects for normally consolidated fine-grained materials.

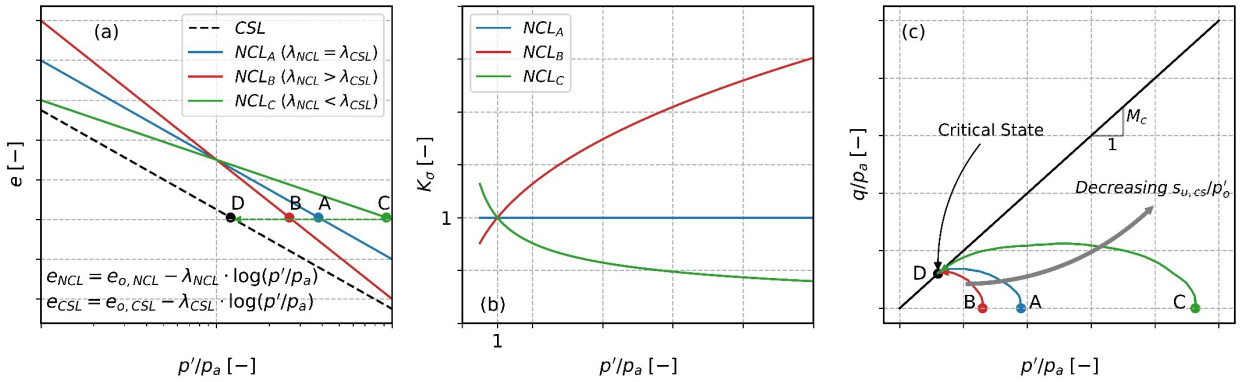

Figure 2.6 Schematic illustrations showing: (a) different scenarios of NCL slopes relative to the CSL slope, (b) their corresponding K_σ effects, and, (c) stress paths of specimens at a same void ratio undergoing monotonic undrained loading for the three cases.

Returning to the analysis of stress dependency of cyclic strength in the compiled dataset, we compute K_σ by normalizing CRR^*_{std} values from the database by $CRR^*_{std,100kPa}$ (CRR^*_{std} at σ'_{vc}=100kPa) for each study, as shown in Equation (2.8),

$$\frac{CRR^*_{std}}{CRR^*_{std,100kPa}} = K_\sigma = \left(\frac{\sigma'_{vc}}{p_a}\right)^{-\beta} \tag{2.8}$$

where β is the regressed parameter and p_a = 100 kPa.

Figure 2.7 shows the variation of the regressed exponent β, along with their error bars, with *PI*. Three of the exponents are negative ($\beta < 0$) and correspond to an increase in CRR_{std} with σ'_{vc}. Four exponents are approximately zero, in which case K_σ is approximately 1.0 for all σ'_{vc}. Two had $\beta >$ 0, indicating that K_σ decreases as σ'_{vc} increases. The 95% confidence limits encompass $\beta = 0$ for the *PI* range of the available data, which means that we cannot reject the null hypothesis that $K_\sigma = 1$ for this dataset. We also cannot reject the null hypothesis that K_σ is unrelated to *PI*. However, these statistical tests are strongly influenced by the amount of available data, which is rather sparse at this time. We therefore conclude that more testing is needed to identify potential trends and the factors that may affect K_σ for different fine-grained soils. Due to inherent variability of small, intact specimens, we believe that reconstituted specimens will be the most useful means by which to investigate these effects.

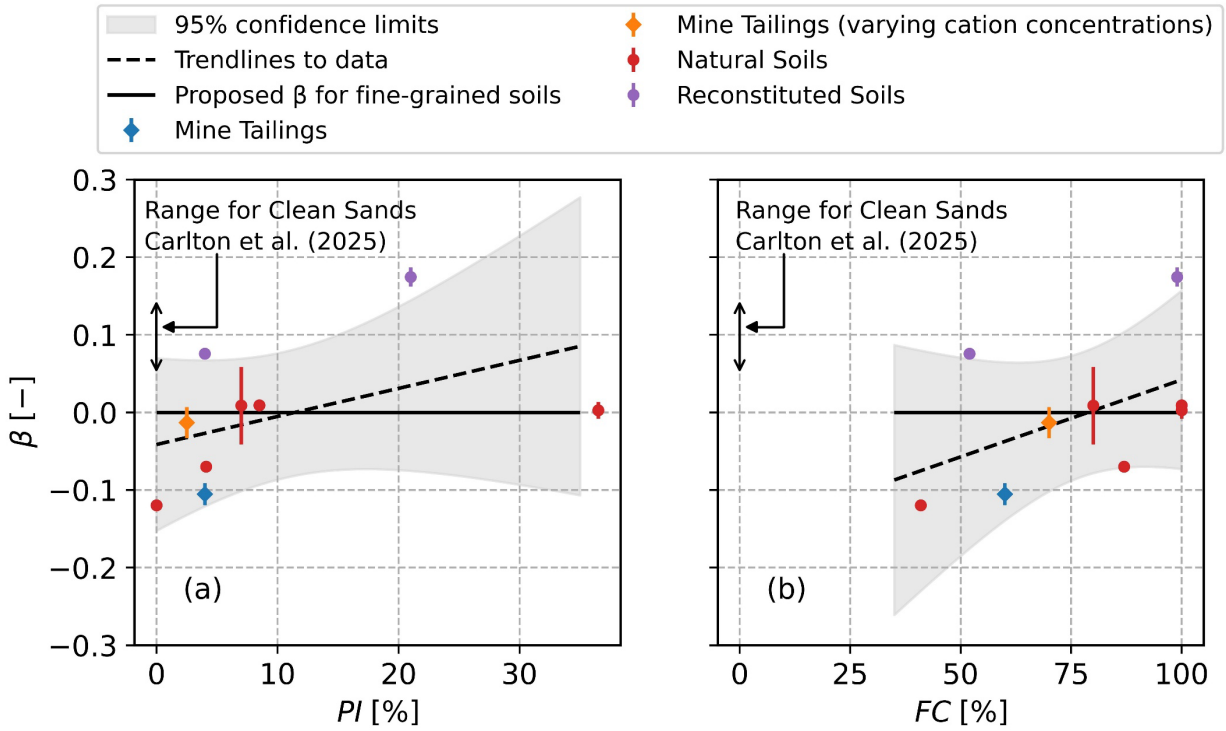

Figure 2.7 Variation in β parameter with a) *PI* and b) *FC*.

Based on the above and considering that absolute values of β for fine-grained materials are much smaller than for sands, we assume no overburden effect on the cyclic resistance of fine-grained materials (β=0), which is equivalent to assuming that the slopes of the NCL and CSL are parallel.

This is shown as the solid horizontal line at β=0 in Figure 2.7. The corresponding K_σ for CRR_{std}^{f} along with K_σ models for CRR_{std}^{s} from Carlton et al. (2025) are shown in Figure 2.8.

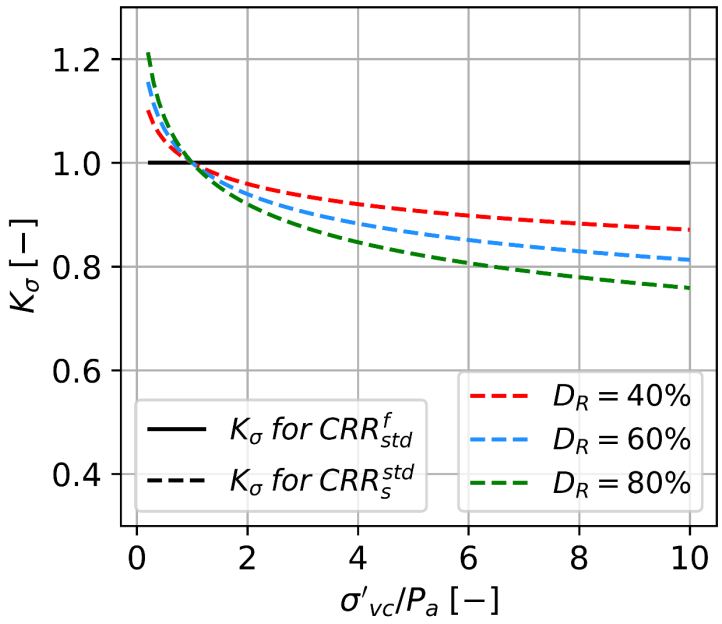

Figure 2.8 K_σ models for CRR_{std}^{s} (Cartlon et al. 2025) and CRR_{std}^{f} (present study).

We recommend subsequent expansion of the database and consider extending the analytical framework to consider more generalized scenarios where the NCL and CSL are nonlinear.

2.4.2 Effect of Overconsolidation

Over-consolidation has long been recognized as significantly increasing the cyclic resistance of soils (e.g., Seed 1979). For a material with $OCR > 1$, as consolidation stress increases OCR decreases, which reduces cyclic strength. As noted previously in Section 2.4.1, such strength reductions associated with reduced OCR can easily be misinterpreted as a K_σ effect.

Despite its significant contributions to cyclic resistance, a limited number of studies have specifically investigated OCR effects and such effects are not directly accounted for in legacy liquefaction triggering models (e.g., Boulanger and Idriss 2016; Cetin et al. 2018). Early work quantifying OCR effects was performed by Ishihara and Takatsu (1979), which involved cyclic torsional shear testing of Fuji River sand supplemented with some additional data. Based on their test results, they proposed a correction factor as follows:

$$\frac{\mathrm{CRR_{std}}}{\mathrm{CRR_{std,OCR=1}}} = \mathrm{OCR^{n}} \tag{2.9}$$

They recommended n = 0.5 and that the model be used for OCR values in the range of 1 to 5. Subsequent studies by Manmatharajan and Sivathayalan (2011) and Shahsavari and Sivathayalan

(2014) performed cyclic simple shear and cyclic triaxial tests on reconstituted Fraser River sand at same confining stress but at different *OCR* levels. Based on their test results, they proposed the following linear relationship,

$$K_{OCR} = \frac{\mathrm{CRR_{std}}}{\mathrm{CRR_{std,OCR=1}}} = 0.38 \cdot (OCR - 1) + 1 \quad (2.10)$$

Equations (2.9) and (2.10) provide similar results for sands.

For clay-like fine-grained materials, it has often been assumed in past work (e.g., Boulanger and Idriss 2007), that the monotonic undrained shear strength and the cyclic undrained shear strength are similarly influenced by *OCR*. Based on this assumption, the well-known effects of *OCR* on monotonic undrained strengths (Ladd 1991) are applied to CRR^{*}_{std}. However, the validity of this assumption is not verified in the literature. Chen and Olson (2022) collated an extensive database of cyclic test results from the literature to evaluate the influence of overconsolidation on the cyclic resistance of sands, silts, and clays. They divided the database into different series based on the soil properties like *PI* and w_c/LL ratio. The data was adjusted to an equivalent simple shear condition and the *OCR* effect was quantified by regressing an *n* value for each subset of the data as per Equation (2.9). They argued that there is a slight increase in the value of *n* with *PI* but the data at high *PI* were limited.

We investigate *OCR* effects using a subset of the database from Section 2.2, which is used to augment the data from Chen and Olson (2022) and thereby refine the K_{OCR} term. We have considered all fine-grained materials ($FC \geq 35\%$) to study this effect. To assess the influence of *OCR*, we identify from the database suites of cyclic tests on similar materials at different *OCR* values. Ideally, the best way to isolate the effect of overconsolidation is to perform cyclic tests at the same confining stress but different *OCRs* prior to shearing. Such cases of cyclic test data are limited to a few reconstituted specimens that were prepared in a laboratory. Typical testing requirements (e.g., Ladd 1991) for intact specimens are that different specimens are loaded to different confining stresses to achieve the desired range of *OCR*. Hence, such tests involve different consolidation stresses and different *OCRs* between specimens, meaning that *OCR* effects cannot strictly be isolated. However, if overburden effects can be assumed as negligible as shown in Section 2.4.1, then the observed trends from such test suites can be used to evaluate *OCR* effects.

The suite of tests developed for this investigation was filtered based on the following criteria to isolate *OCR* effects from other potential effects:

1. The range of *OCRs* over which the tests were performed must be greater than 0.15 in natural log units i.e. $\Delta ln(OCR) > 0.15$.

2. Extrapolation to obtain *CRR* using Equation (2.1) must not exceed 5 cycles.

On this basis, the data selected to evaluate *OCR* effects is summarized in Table 2.2.

Table 2.2 Subset of database used to study the influence of *OCR* on *CRR*

Reference	Soil	*OCR*	*PI*	*n*
Dadashiserej et al. (2023)	Site F	1 – 2.6	2	0.31
Dadashiserej et al. (2023)	Site E	1 – 2.2	15	0.58
Dahl (2011)	Stratum A	1 - 4	18	0.76
Dadashiserej et al. (2023)	Site E	1 – 2	28	0.76
Dadashiserej et al. (2023)	Site E	1 - 2	11	0.24
Preciado Reyes (2021)	Longview Silt	2 - 4	5.5	0.64
Dickenson et al. (2021)	Columbia River Silt	1 - 2	10	0.88
Dahl (2011)	Drammen Clay	1 - 4	27	0.69
Dahl (2011)	Boston Blue Clay	1 - 2	21	0.81
Dahl (2011)	Stratum B	2 - 4	4	0.76
Tom (2011)	Iasc Silt	1 - 4	24	0.86

Corrections were applied to derive CRR_{std} values from the lab data using Equation (2.2). Each filtered data point was normalized by the corresponding CRR_{std} for a normally consolidated specimen. Equation (2.9) was then fitted to the data and the value of *n* was evaluated. We generally used the data points from Chen and Olson (2022) as provided. However, in the case of data points from Eslami (2017) on reconstituted specimens denoted *SBFW*, *SBSW*, *SKFW*, we modified the data to account for the stress-control issues and the secondary compression effects, which influence *OCR* values. Figure 2.9 shows the resulting values of exponent *n* for each data subset from the database vs. *PI*. The first plot at *PI* = 0 shows the distribution of *n* for coarse-grained materials (FC < 35%) that are non-plastic. The second plot shows the distribution of *n* for fine-grained materials (FC ≥ 35%) with known *PI*. The data has a slight positive slope but the slope is modest and its uncertainty is large, mainly because of a lack of data at high *PI*. The *PI* of Koto A soil reported in Ishihara et al. (1978) was measured using the fines fraction and hence it was adjusted as per the relationship from Qamar et al. (2024) to be in accordance with ASTM standards.

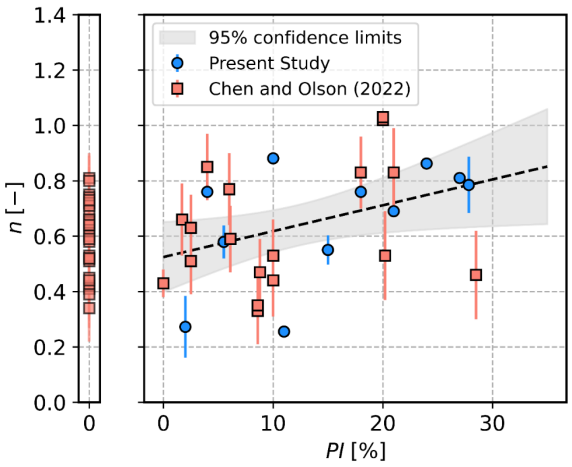

Figure 2.9 Variation in *OCR* exponent (n) with *PI* for a) coarse-grained materials and b) fine-grained materials (*FC*≥35%).

Assuming invariance of n with PI, the mean value of $n=0.64$ is used to formulate a K_{OCR} model for fine-grained materials per Eq. 2.9. The resulting K_{OCR} values are plotted in Figure 2.10 along with the data points developed in this study. The scatter at OCR=1 is caused by cases when there are multiple tests at OCR=1. Also shown in Figure 2.9 for reference purposes is the OCR effect on monotonic undrained strength from Ladd (1991).

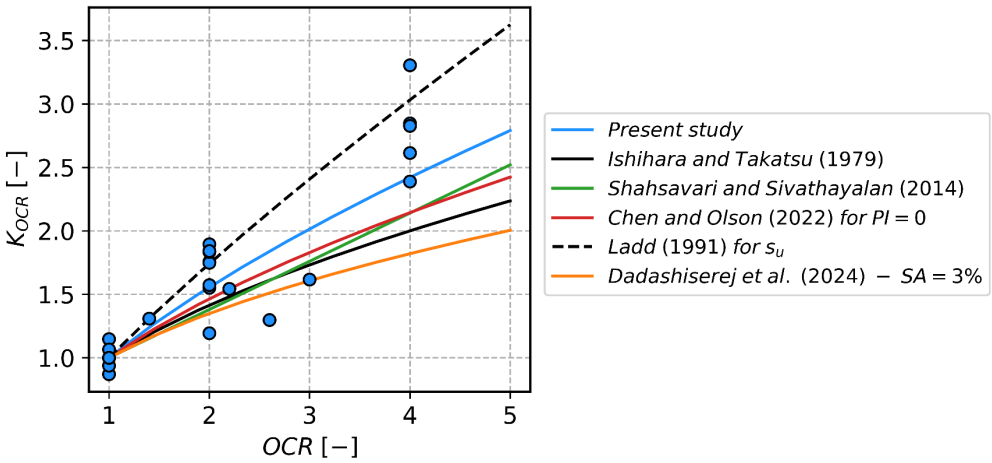

Figure 2.10 Overburden correction factor K_{OCR}

As expected, the older models are consistent with each other since they were based mainly on non-plastic coarse-grained materials. The curve for fine-grained materials from the present study lies above the curves for sands. The inferred K_{OCR} term from Dadashiserej et al. (2024) for translational silts (for SA=3%) is below the other curves. Moreover, it is noted that the curve for s_u from Ladd (1991) is higher (steeper) than the curves for cyclic strength, which indicates that some of the OCR effects for monotonic strengths are lost for cyclic strengths. This may be caused by the differences in the damage caused to the soil fabric under cyclic loading conditions (Dadashiserej et al. 2024).

The findings from this section reveal that *OCR* influences the cyclic undrained strength to a lesser extent than the monotonic undrained shear strength. This necessitates updating the existing cyclic softening approach for evaluating CRR_{std} for clay-like fine-grained materials to account for *OCR* effects.

2.4.3 Cyclic Resistance Ratios of Clay-Like Soils (PI ≥ 5)

Undrained shear strength ratio (τ_{cyc}/s_u) has been used as a component of the analysis procedure for evaluating the cyclic strength of clay-like materials in a cyclic softening framework (Boulanger and Idriss 2006, 2007). Using results from multiple cyclic and monotonic tests on fine-grained soils, Dahl (2011) updated the original model for τ_{cyc}/s_u. The updated τ_{cyc}/s_u model was recommended for use to evaluate the cyclic strength of '*Group A (clay-like) soils*' which were typically not prone to disturbance, exhibited strength normalization, and a well-defined pre-consolidation stress. This method of evaluating cyclic strength relies on monotonic undrained tests in combination with *OCR* (using preconsolidation pressures from consolidation tests) to evaluate monotonic undrained strength, which are then multiplied by τ_{cyc}/s_u from correlations to estimate *CRR*, thereby avoiding the need for expensive cyclic tests. An important assumption of the cyclic softening approach implied by the absence of a K_{OCR} term is that *OCR* influences the cyclic and monotonic undrained strengths of the material to the same extent. This assumption is not correct for the soils examined in Section 2.4.2.

In this section, we use a larger dataset (relative to Boulanger and Idriss 2007 and Dahl 2011) of clay-like soils with $PI \geq 5$ to develop a *PI*-conditioned τ_{cyc}/s_u model. The data used to derive the model is a subset of the database previously used in Section 2.2 with $PI \geq 5$. The selected subset consists of tests on intact specimens from Wijewickreme et al. (2005), Sanin (2010), Dickenson et al. (2021), Preciado Reyes (2021), Dadashiserej et al. (2023), Sanin (2010), Soysa and Wijewickreme (2015), Soysa (2015), Verma and Wijewickreme (2018), Verma (2019), Dadashiserej et al. (2024) and Dahl et al. (2018). Reconstituted specimens in the subset were taken from Eslami (2017), Tom (2011), Reid and Fourie (2017) and Price et al. (2015). The distribution of this dataset is shown on the plasticity chart in Figure 2.11. The materials with *PI* between 5 and 7 (Site CT, JS from Soysa (2015) and Longview silt from Preciado Reyes (2021)) were included to the model development dataset since they exhibit strength normalization which is a characteristic of clay-like materials.

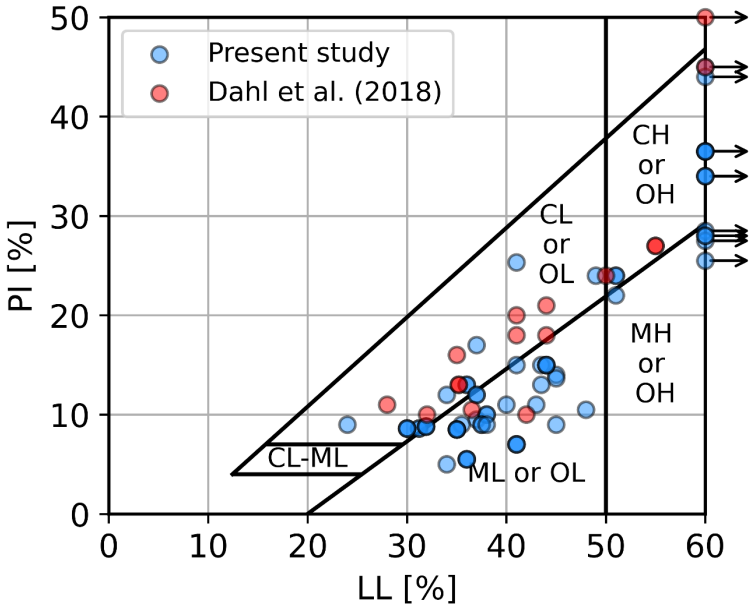

Figure 2.11 Plasticity chart showing the clay-like materials used in this section.

Within this dataset, we have instances of s_u that were directly measured from monotonic lab tests and a few cases where the authors used correlations to estimate s_u. Some studies did not report s_u (from monotonic testing or correlations) and in those cases we estimated undrained strength ratio as (Ching and Phoon 2014):

$$\frac{s_{u,mob}}{\sigma'_{vc}} = 0.28 \cdot OCR^{0.8} \cdot \left(\frac{PI}{20}\right)^{-0.005} \tag{2.11}$$

where $s_{u,mob}$ refers to the mobilized shear strength in the field and can be converted to equivalent lab measured s_u using the procedure from Mesri and Huvaj (2007) as tabulated in Ching and Phoon (2014). The coefficient of variation (*COV*) of the monotonic strength ratios from Eq. 2.11 is 0.4982 (Ching and Phoon 2014). Equation (2.11) was used only for intact specimens since the model's applicability to reconstituted specimens was not known. The errors in the laboratory measured s_u values were quantified using *COV* = 0.2 (Phoon and Retief 2016).

The data set contains 65 lab tested specimens, 9 specimens with an estimated s_u reported in the original study and 8 specimens whose s_u was approximated using Eq. 2.11. There are 67 intact and 15 pluviated specimens within the subset. The cyclic strength of the materials, τ_{cyc}, is taken at 30 cycles (per Boulanger and Idriss 2006) and represents the laboratory measured cyclic strength without corrections for test type, consolidation, 2D effects etc. This ensures that the monotonic and cyclic shear strengths represent the material under the similar conditions. Figure 2.12 shows distributions of the dataset with respect to *PI*, *OCR*, and τ_{cyc}/s_u.

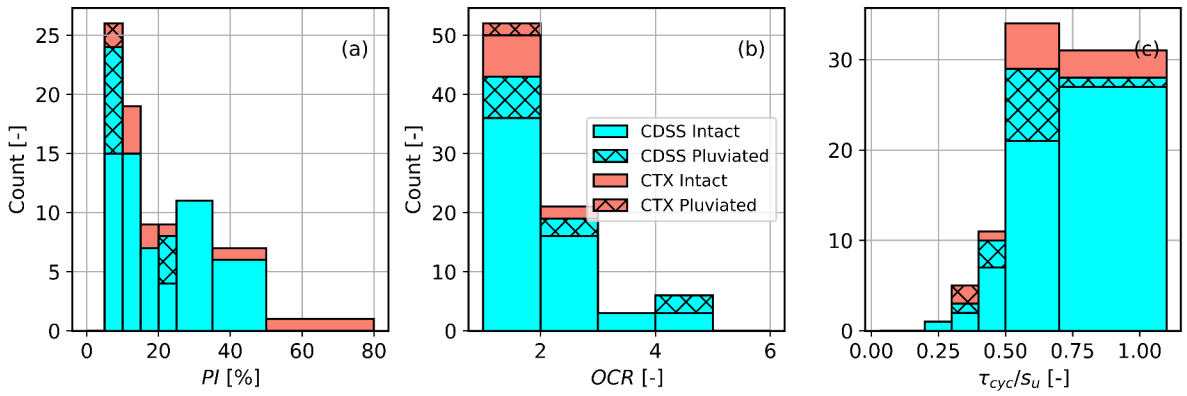

Figure 2.12 Distributions of *PI*, *OCR*, and τ_{cyc}/s_u in the clay-like dataset (*PI*≥5), aggregated by test type and specimen type (reconstituted or intact).

The variation in τ_{cyc}/s_u with *PI* is plotted in Figure 2.13a along with the cyclic softening model from Dahl et al. (2018). The sizes of data points in the plot are scaled by their *OCR*. By inspection, it is noted that the larger marker points generally plot below the smaller points. The binned mean values of the shear strength ratio in Figure 2.13b show this effect of *OCR* on shear strength ratio. The binned means of the materials having $OCR \leq 1.5$ are closer to the recommendation from Dahl et al. (2018) whereas the binned means of higher *OCR* specimens (pink and red diamonds on the plot) are lower than the model from Dahl et al. (2018). Similar plots for pluviated specimens are shown in Figure 2.14. The τ_{cyc}/s_u values for the pluviated specimens are below the Dahl's model. The influence of *OCR* on τ_{cyc}/s_u for the pluviated specimens is similar to the intact specimens.

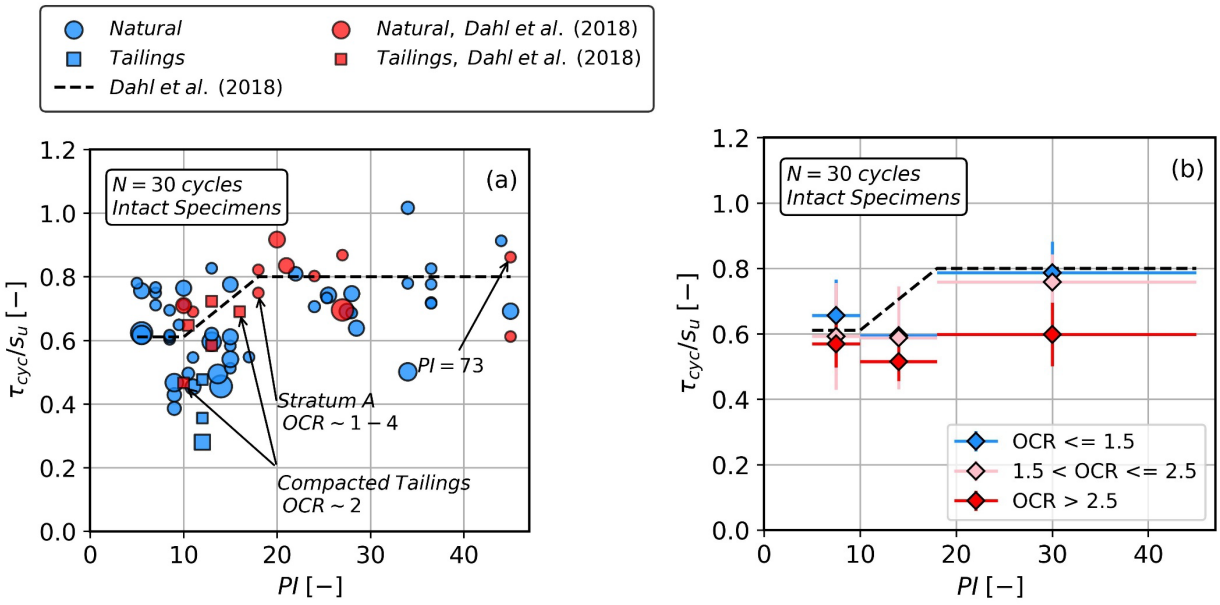

Figure 2.13 a) Variation in τ_{cyc}/s_u vs. *PI*, b) Binned means of τ_{cyc}/s_u vs. *PI* for intact clay-like specimens.

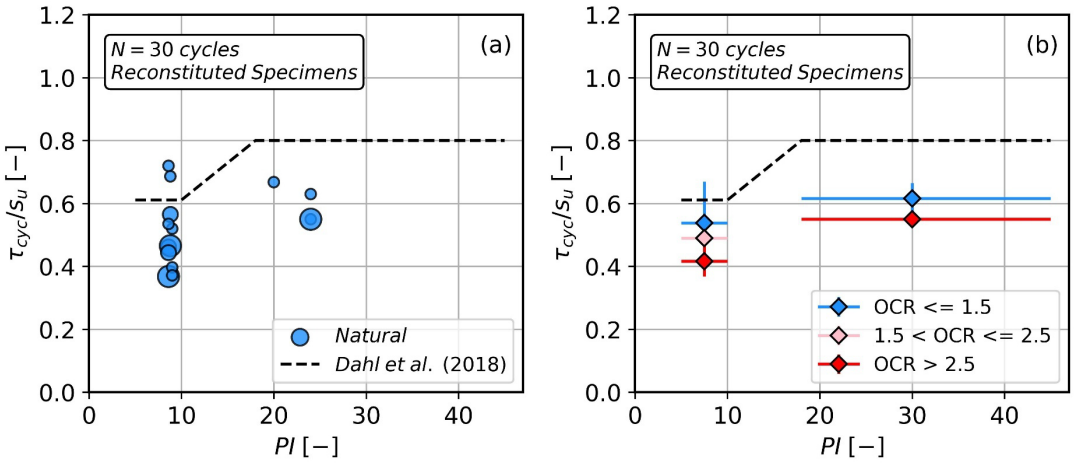

Figure 2.14 Variation in τ_{cyc}/s_u vs. *PI*, b) Binned means of τ_{cyc}/s_u vs. *PI* for reconstituted clay-like specimens.

We developed a model to fit the dataset shown in Figures 2.13-2.14. We applied a Bayesian inference approach that considers data uncertainties. Model developed applied the following assumptions:

1. Since the cyclic tests are conducted in a stress-controlled environment, the error in τ_{cyc} is generally negligible. The major source of uncertainty is therefore related to monotonic strengths, s_u. Accordingly, the *COV* of τ_{cyc}/s_u is taken as the *COV* of s_u, which is taken as 0.4982 for cases where s_u was approximated and 0.2 for lab-measured s_u.

2. The independent variable *PI* is assumed to be not influenced by the measurement error.

3. The influence of test type was neglected based on the hypothesis that the cyclic strength and the monotonic strengths are influenced in the same manner based on the type of test. This assumption can be verified by observing no bias in the model with respect to test type.

4. Both intact and reconstituted specimen tests are used in model development and potential biases between the two data sets are evaluated statistically using mixed effects regression.

A logistic function is chosen to smoothly capture the trend in τ_{cyc}/s_u with *PI* and *OCR* as given in Equation (2.12),

$$\frac{\tau_{cyc}}{s_u} = \left(\mu_2 + \frac{\mu_3}{1+e^{-\mu_1\cdot(PI-\mu_0)}}\right)\cdot OCR^{\mu_4} + \Delta\mu\cdot\xi_{specimen} + \epsilon\cdot\sigma_{\text{model}} \qquad (2.12)$$

where μ_0, μ_1, μ_2, μ_3 are coefficients that define the shape of the logistic curve, μ_4 controls the dependence on *OCR*, and $\Delta\mu$ and $\xi_{specimen}$ extend the model's applicability to reconstituted specimens as a part of the mixed effects regression model. The dispersion of the strength ratio estimate is represented by $\epsilon\cdot\sigma_{model}$, where ϵ is the standard normal variate (mean of zero, standard deviation of one) and σ_{model} is the uncertainty in the model

To account for the measurement errors associated with τ_{cyc}/s_u data, we scaled the model uncertainty with weights proportional to the variance of the measurement error associated with each data point. The weights were normalized to ensure balance in the model. Uninformed priors were chosen for all the parameters and the Bayesian analysis was performed using PyMC package in Python (Abril-Pla et al. 2023) to draw samples from the posterior distribution of each model parameter using the no u-turn sampler (NUTS). 1000 samples were drawn from 4 independent chains and their distributions are shown in

Figure 2.15.

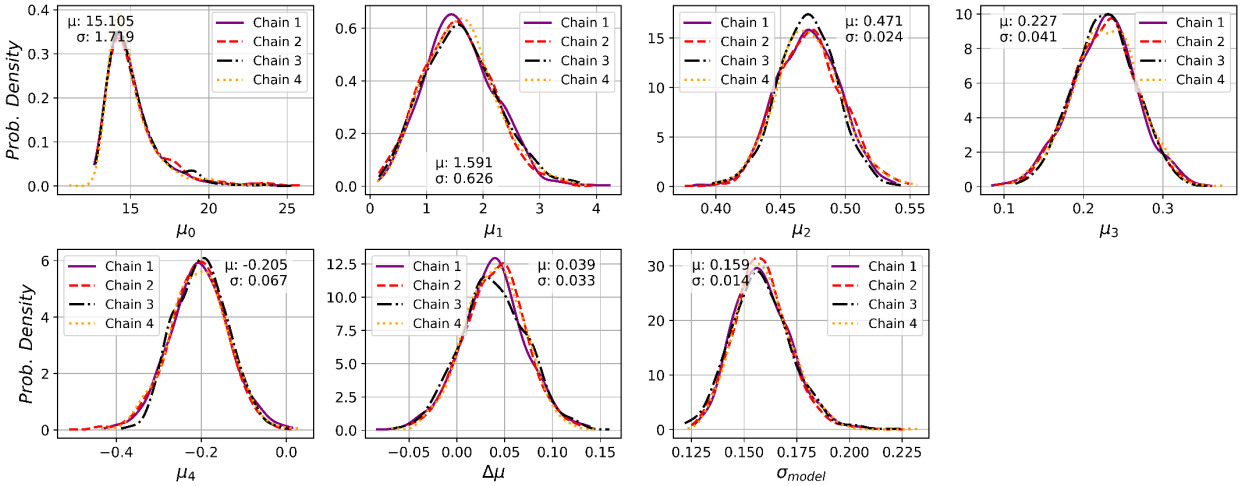

Figure 2.15 Posterior distributions of model parameters in the τ_{cyc}/s_u model

All sampling chains produce similar results, and we conclude that the sampling was stable. The posterior distribution of the model parameters represents within-model epistemic uncertainty that would be reduced by training the model on a larger dataset.

The mean model predictions for different *OCR* values are shown in Figure 2.16 along with the data points binned by *OCR*. The model is considered to provide a satisfactory fit to the data and follows physically expected trends.

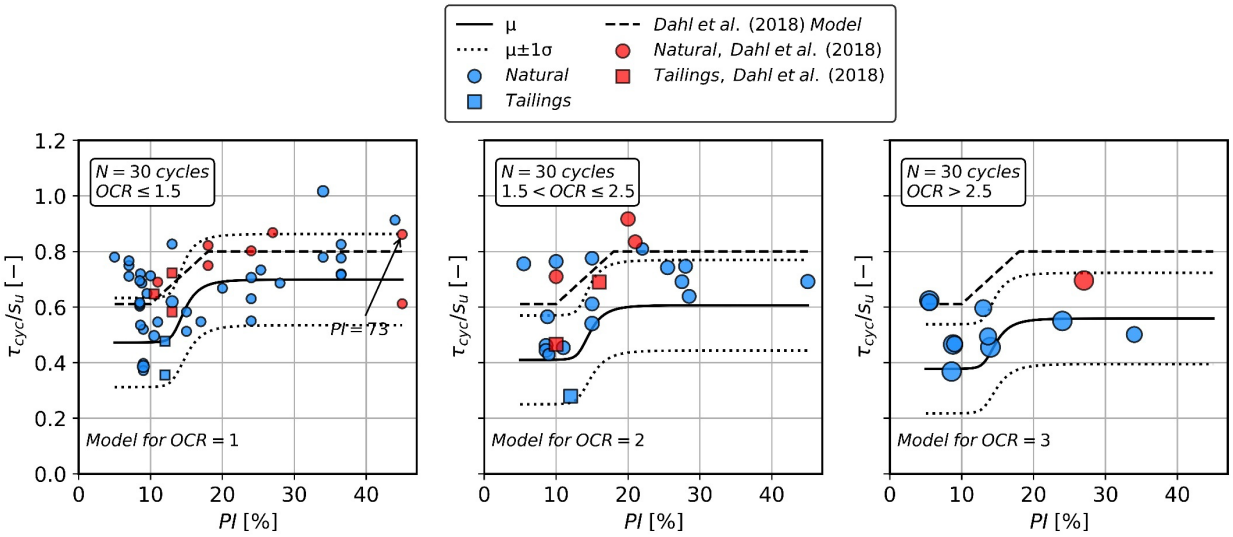

Figure 2.16 Comparison of strength ratio model (Eq. 2.11) to data for different OCR bins

2.4.4 Cyclic Resistance Ratio of All Fine-Grained Materials ($PI \geq 0$)

Section 2.4.3 presented a model that can be used to estimate *CRR* based on concepts of strength normalization, which is limited to clay-like soils. However, we often must evaluate the cyclic resistance of low-plasticity or nonplastic fine-grained soils, in which case we can either apply a fines correction to a penetration resistance, or we can use laboratory test data to directly define CRR_{std}^{f}. This section pertains to an empirical model for *CRR* that does not rely on to strength normalization principals, instead being directly regressed from laboratory test results with *PI*, *OCR*, and *N* serving as independent variables. It is therefore applicable to fine-grained soils regardless of whether strength normalization applicability. A model originally formulated for this purpose was presented by Dadashiserej et al. (2024) and was considered applicable for transitional silts.

The Dadashiserej et al. (2024) model was regressed using results from multiple cyclic tests conducted on intact silts supplemented with additional data from the literature. Their model captures the dependence of *CRR* on *PI*, *OCR*, N_{ref}, and shear strain level. The functional form of model is given by Equations (2.13) and (2.14).

$$CRR_{std}^{f} = c_0 \cdot (PI + 1)^{c_1} \cdot OCR^{c_2} \cdot N^{-b} \tag{2.13}$$

$$b = a_0 \cdot PI + a_1 \tag{2.14}$$

The parameters c_0, c_1 and c_2 are strain dependent parameters and a_0=-0.003 and a_1=0.147. For 3%*SA* shear strain, we have c_0=0.188, c_1=0.1101 and c_2=0.4321.

We assessed the performance of the Dadashiserej et al. (2024) CRR_{std}^{f} model using all the fine-grained materials (*FC*≥35%) from the dataset presented in Section 2.2. Residual plots (Figure 2.17) with respect to *PI* and *OCR* show no bias for the points that were used in their model (red points

in Figure 2.17). However, the residuals show trends with respect to the overall data, which is not unexpected because the data set gathered herein spanned a wider range of conditions than that considered in Dadashiserej et al. (2024), and the data were processed to different reference conditions for modelling. Accordingly, we re-fit the coefficients in Eq. 2.13 using the expanded database.

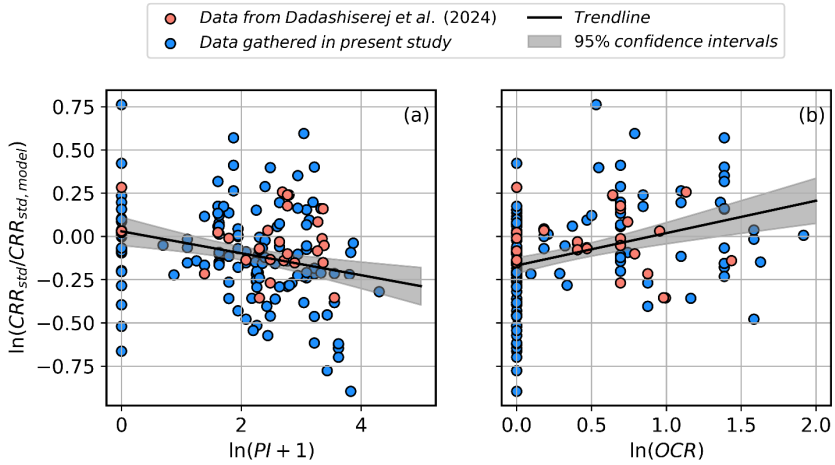

Figure 2.17 Residual plots for Dadashiserej et al. (2024)'s model.

We first regressed the equation for b (Equation (2.14)) using the full data set. This was done to avoid correlation between the independent variables if Equations (2.13) and (2.14) were regressed simultaneously. It should be noted that regressed b values are influenced by the range of *CSR*-*N* points used in their evaluation. The b values used in this study were generally regressed using *CSR*-*N* points close to the chosen reference condition of 15 cycles to get the best estimates of CRR_{std}. Including data at very high N values tends to decrease the regressed b value and hence give estimates of CRR_{std} that may be erroneous. This finding calls into question the assumption that b is a constant. As a result of using a reference condition of 15 cycles, our proposed model is appropriate for shallow crustal earthquakes but may be biased for large-magnitude subduction earthquakes that have larger numbers of cycles.

A linear function would give negative b values at high *PI* values and hence an exponential decay function was chosen to model b vs. *PI*. The regression was performed using Bayesian inference with uninformed priors. Mean model predictions along with the range for all posterior samples drawn in the analysis are shown in Figure 2.18. The fitted model depicts an expected trend in b decreasing with increasing *PI*. The fitted model is close to the linear model from Dadashiserej et al. (2024) at low *PI*s.

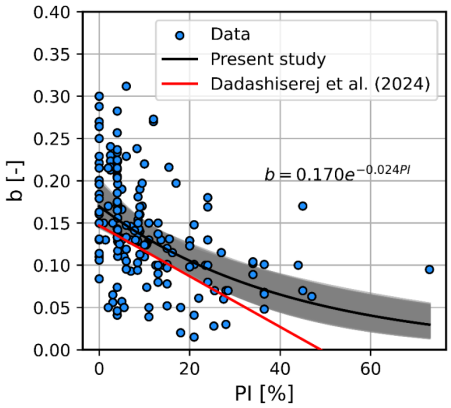

Figure 2.18 Model for b vs. PI

A log transformation was applied to Equation (2.13) to produce Equation (2.15).

$$ln\left(CRR^{f}{}_{std}\right) = ln(c_0) + c_1\, ln(PI + 1) + c_2\, ln(OCR) - b\, ln(N) + \Delta c_{0,spec}\xi_{spec} + \varepsilon \cdot \sigma_{CRR_f} \qquad (2.15)$$

where σ_{CRR_f} is the model uncertainty and $c_0 - c_2$ are model coefficients. Priors for the model parameters were taken as the mean results from Dadashiserej et al. (2024) for a shear strain of 3% *SA* but with high standard deviation (10 times the mean values). Group effects for alternative specimen types were included in the regression using an intercept adjustment factor $\Delta c_{0,spec}$. Parameter ξ_{spec} in Equation (2.15) is a dummy variable that takes the value of 1 when the specimen is intact and 0 when the specimen is pluviated/deposited. Parameter b is evaluated using the mean model from Figure 2.18. For this modeling, it must be noted that CRR_{std} is not corrected for specimen type (Eq. 2.2) since we evaluate the influence of specimen type within the regression. Bayesian analysis was implemented in Python using the PyMC package to draw samples from the posterior distribution of each model parameter using the no u-turn sampler (NUTS). The posterior sample distributions from the various sampling chains are shown in Figure 2.19.

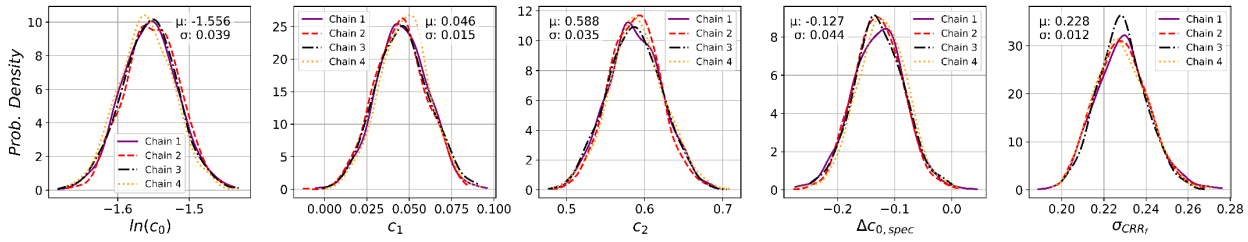

Figure 2.19 Posterior distributions of the model parameters in the CRR_f model

The sampling chains produced similar distributions confirming the model convergence. The residual plots shown in Figure 2.20 show no bias with respect to the regression variables. The regressed distribution of $\Delta c_{0,spec}$ shows that pluviated/deposited specimens have cyclic strengths that are on average 0.87 times the cyclic strengths from intact specimens. This is the K_s to obtain CRR_{std} for pluviated/deposited fine-grained specimens as mentioned in Equation (2.2). This study did not derive an independent factor to account for the differences between *CDSS* and *CTX* test results, which were assumed to follow $CRR_{CDSS} = 0.8CRR_{CTX}$.

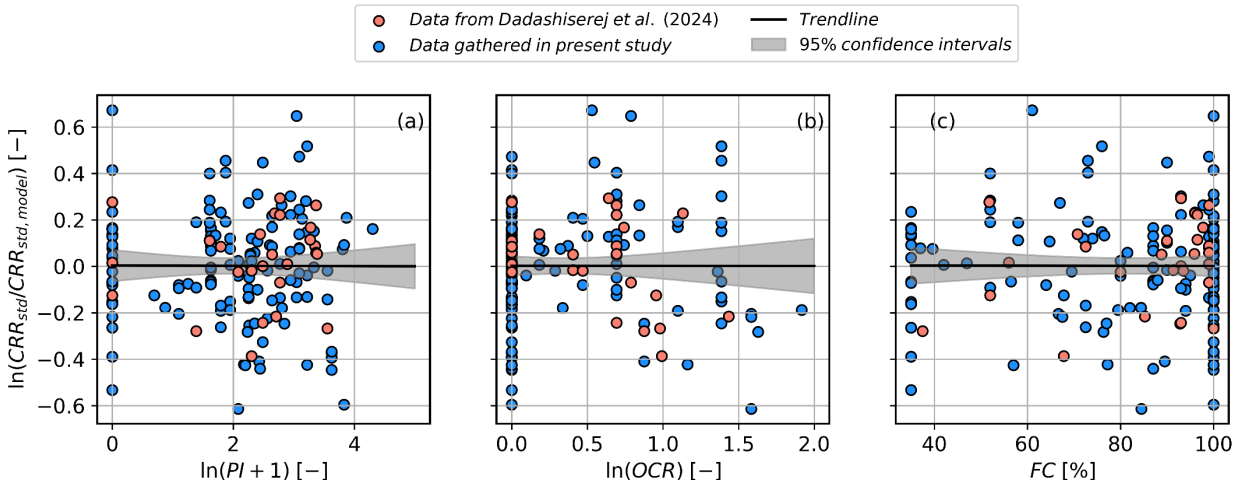

Figure 2.20 Residual plots for the regressed model w.r.t a) ln(*PI*+1), b) ln(*OCR*) and c) *FC*.

Eq. (2.15) is applied with the mean model coefficients in Figure 2.19 to obtain estimates of CRR_{std} for normally consolidated materials as shown in Figure 2.21. The model from Dadashiserej et al. (2024) for a single amplitude strain level of 3% is also shown in Figure 2.21, which fits the red data points from their study well. Their dataset did not have many data points at high *PI* and hence their model is steeper when compared against the overall dataset and model from the present study. The *OCR* exponent c_2 from the present study also benefits from the high number of data points at high *OCR*. Besides the differences between the datasets, it must be noted that there were differences between the modeling procedures adopted in both these studies.

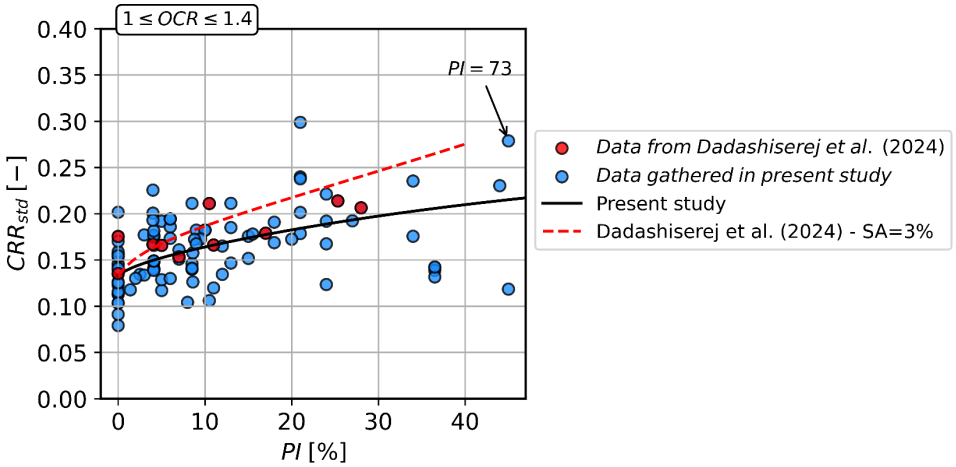

Figure 2.21 Normally consolidated datapoints (FC ≥ 35%) along with the CRR_{std}^{f} models from Dadashiserej et al. (2024) and present study.

2.5 Cyclic Resistance Model for Coarse-Fine Mixtures

With the cyclic resistance ratio models for sands and fine-grained materials established in the previous sections, here we apply them to facilitate CRR_{std} predictions for any *FC* as shown in Eq. (2.16) (repeated from Eq. 2.3),

$$CRR_{std} = CRR^{f}_{std} + \frac{CRR^{s}_{std} - CRR^{f}_{std}}{1+e^{\gamma_o(FC-\gamma_1)}} \tag{2.16}$$

where γ_o and γ_1 are regression coefficients.

Despite the large size of our database, only a small fraction could be used in the regression for the following reasons:

1. Tamped specimens at high *FC* could not be used due to the inability to quantify their *OCR* effects.

2. Materials having *FC* ≥ 35% do not have an associated relative density.

The model parameters were trained on 88 (CRR_{std}, D_R, *FC*, *PI*, *OCR*) datapoints using L-BFGS-B algorithm (Zhu et al. 1997) in Python. The regressed values are γ_o = 0.198 and γ_1 = 29.86.

By rearranging the terms in Equation (2.16), the cyclic resistance of a given material can be represented as a weighted sum of the cyclic resistance of sand and fines as given by Equations (2.17) and (2.18). This weight is a function of the material's *FC*.

$$CRR_{std} = (1-w)\cdot CRR^{f}_{std} + w \cdot CRR^{s}_{std} \tag{2.17}$$

$$w = \frac{1}{1+e^{\gamma_o(FC-\gamma_1)}} \tag{2.18}$$

The weight factor (w) is plotted versus the *FC* in Figure 2.22. The weight is close to 1.0 for *FC* < 10% implying that the mixture's cyclic resistance is controlled solely by the coarse-grained particles. For *FC* > 50%, the fines fraction controls the cyclic strength of property of the soil mixture. The proposed framework requires the estimation of CRR^{s}_{std} and CRR^{f}_{std} at all fines content as clarified earlier in Section 2.2.4. For practical purposes, one can assume $CRR_{std} \approx CRR^{s}_{std}$ for FC < 10% and $CRR_{std} \approx CRR^{f}_{std}$ for FC > 50%.

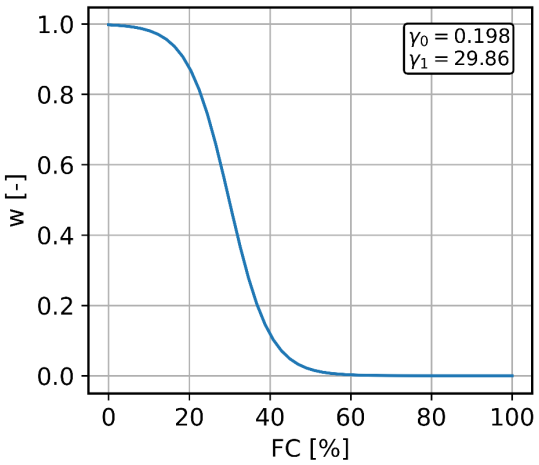

Figure 2.22 Weight factor vs. *FC* for the unified model

3 Effect of Fines on Penetration Resistance

Fines influence measured penetration resistance in two different ways. First, the addition of fines to sand influences the force chain contact of the mixture. Based on the *FC* relative to FC_{th}, the mechanical behavior of the material can vary between coarse-dominated at low *FC* and fines-dominated at *FC* greater than FC_{th}. Hence, fines influence the strength and compressibility of coarse-fine mixtures. This variation in shear strength and stiffness affects cone tip resistance depending on the amount and nature of the fines. Second, the addition of fines reduces the hydraulic conductivity of soil as the fines occupy the void spaces in the sand. Clean sands are generally considered to be drained during cone testing at the standard 2 cm/s push rate, while clays are undrained. As fines are added to a sand, the behavior will transition from drained to partially drained and ultimately to undrained, which significantly influences cone tip resistance.

Baziar and Moayed (2003) performed calibration chamber tests in which a cone penetrometer was advanced through coarse-fine mixtures at various consolidation stress, σ_c', values (Figure 3.1). The results show that measured excess pore pressure increases as *FC* increases, which points to a change in drainage effects from drained to partially drained or undrained behavior. The reduction in effective stress causes the measured penetration resistance to decrease as *FC* increases. Moreover, the effects of the changes in force chain contact are also reflected in these results.

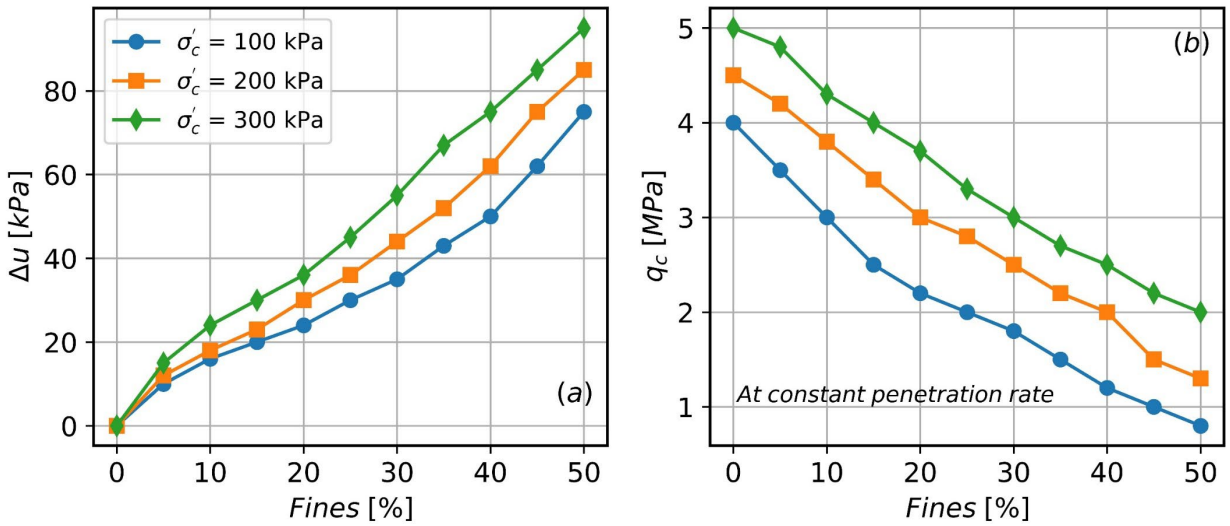

Figure 3.1 Variation in a) Excess pore pressure and b) Tip resistance with *FC* (Adopted from Baziar and Moayed 2003)

3.1 Effect on Fines on Drainage During CPT

Recent research (Ecemis et al. 2022; Thevanayagam et al. 2016) indicates that soil compressibility (m_v), and hydraulic conductivity *(k)* are strongly influenced by *FC* (Figs. 3.2 and 3.3. The coefficient of consolidation *(c_v)*, depends directly upon m_v and k, and is therefore also strongly influenced by *FC* (Fig. 3.4). As fines are added to sand, they block drainage pathways in the void space, thereby reducing k. Increasing fines also causes separations between sand particles, which increases m_v. As *FC* increases, both of these effects tend to decrease c_v, potentially significantly as illustrated by the change of two orders of magnitude as shown in Fig. 3.4.

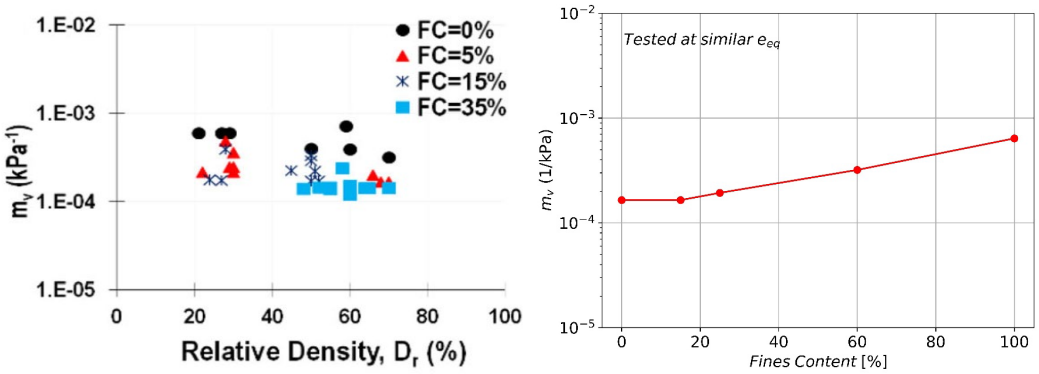

Figure 3.2 Variation of m_v with *FC* a) Ecemis et al. (2022) b) Thevanayagam et al. (2016)

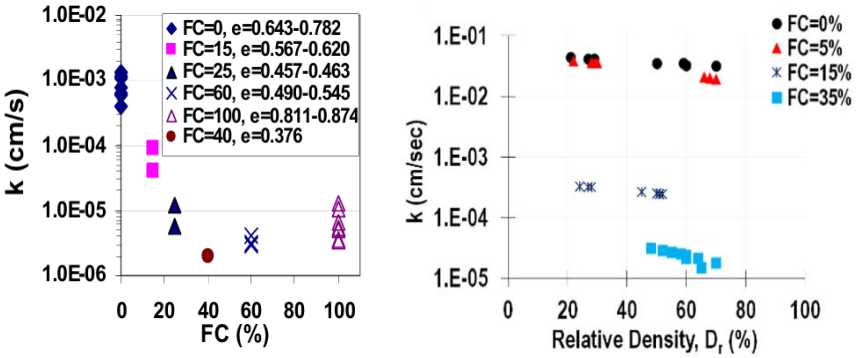

Figure 3.3 Influence of fines on *k* a) At constant e_{eq} (Thevanayagam et al. 2016) b) At constant relative density (Ecemis et al. 2022).

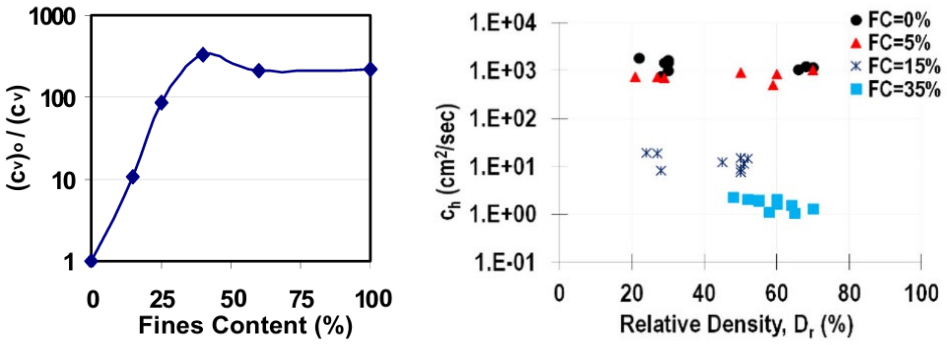

Figure 3.4 Influence of fines on c_v a) At constant e_{eq} (Thevanayagam et al. 2016) b) At constant relative density (Ecemis et al. 2022).

Variable rate cone testing can be used to evaluate how changes to hydraulic properties influence cone tip resistance. At slow penetration rates, excess pore pressures have sufficient time to dissipate, resulting in a drained response, whereas at high penetration rates, the response is partially drained or undrained. The normalized penetration rate *(V)* is defined by Equation 3.1 (Finnie and Randolph 1994), where v is the penetration velocity, d_c is the diameter of the cone and c_v (or c_h) is the coefficient of consolidation in the vertical or horizontal direction.

$$V = \frac{v \cdot d_c}{c_h} \tag{3.1}$$

As illustrated in Figure 3.5, the measured tip resistance is greatest at low values of V (drained penetration) and gradually reduces and becomes constant as V is raised to higher values (undrained penetration). Between these two extreme conditions, the soil response is partially drained. Based on experimental work, various researchers have proposed ranges of V associated with drained, undrained, and partially drained cone penetration response. Drained penetration typically occurs when V is lower than 0.1 to 0.3 and undrained penetration occurs when V exceeds 10-30 (DeJong and Randolph 2012; Mahmoodzadeh and Randolph 2014).

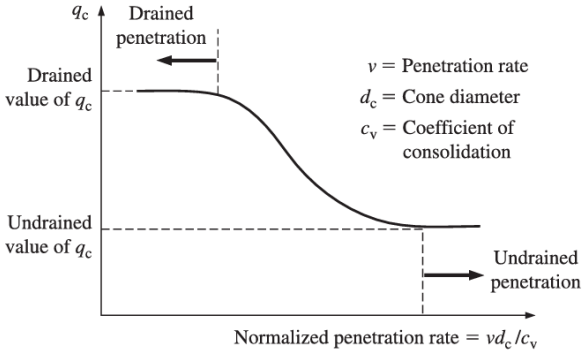

Figure 3.5 Typical results from a variable rate CPT (Salgado 2022)

Variable rate cone penetration tests have been performed in laboratory settings using centrifuge and chamber tests, or in outdoor field settings. Laboratory studies are often performed using

artificially prepared gap graded mixtures of sand and fines. Due to the small scale of typical laboratory test specimens, the penetration is performed using a mini-cone that has only one load cell to measure the tip resistance. The lack of skin friction readings makes it impossible to evaluate soil behavior type indices like I_c. Field tests use full-scale cones and provide tip resistance, sleeve friction and pore pressure measurements. The coefficient of consolidation is estimated in the field by conducting dissipation tests (Krage et al. 2015).

Variable rate penetration tests performed at sites with liquefiable silts and sandy silt deposits have shown that drained tip resistance can be 1.25 to 2.5 times higher than undrained tip resistance (Krage and DeJong 2016). Similar studies at a site in Dronninglund, Denmark containing sandy silts showed that there is a 40% increase in the measured tip resistance as penetration transitions from undrained to drained shearing (Holmsgaard et al. 2016). Drained tip resistance of a clayey silt site in Indiana was seen to be 2 to 3 times higher than the undrained tip resistance (Kim et al. 2008).

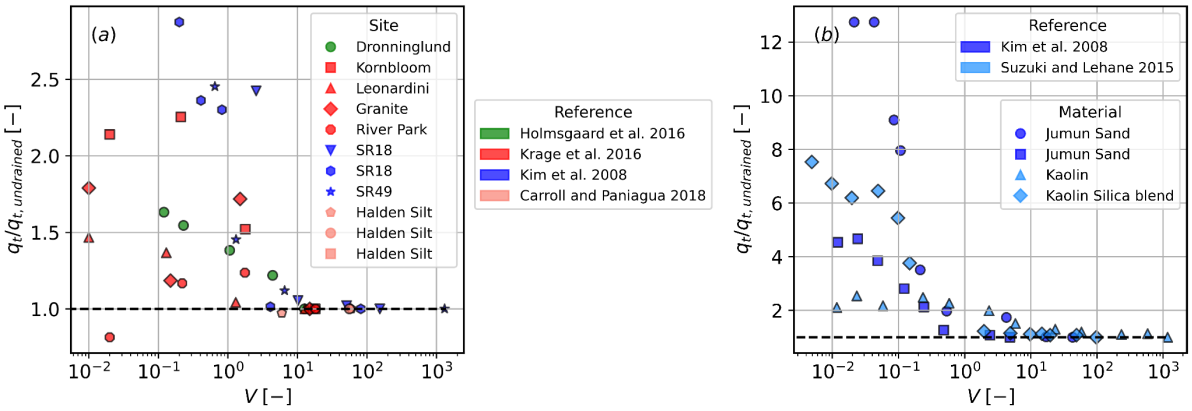

Figure 3.6 Variable rate penetration test results a) Field based and b) Chamber tests

Calibration chamber tests and centrifuge tests have also shown that the drained tip resistance is typically higher than undrained tip resistance (Kim et al. 2008; Price et al. 2019; Suzuki and Lehane 2015). However, the ratios of drained to undrained resistances reported in these studies are much higher (~3 to 12) than the findings in field-based studies (~1.25 to 3). As these lab specimens are prepared by slurry consolidating gap-graded mixtures, they tend to have significantly different soil fabric than naturally occurring soil deposits. Furthermore, drainage conditions at field sites are more complicated than in uniform lab samples. Some of the tests performed in these studies are also believed to be influenced by boundary effects based on the spacing between the wall and the diameter of the cone, and boundary effects are larger for drained loading. Our interpretation is that these factors contribute to the differences in observed ratios.

As CPT penetration rates increase, a corresponding increase in the strain rate is expected as shown in a numerical study by Acar and Tumay (1986). Due to the increased strain rate during undrained cone penetration at high penetration velocities, the measured tip resistance can increase. Nanda et al. (2017) suggested strain rate corrections to account for this effect.

Although the normalized penetration rate V is a fundamental parameter that directly quantifies whether cone testing will be drained or undrained, c_h is often not measured for field sites. Undisturbed samples of these materials often cannot be obtained because they tend to be sandy and /or low plasticity. Hence, as a part of this study we sought to define a simplified relationship between drainage conditions and soil behavior type index, I_c. A benefit is that such a relationship could be applied to typical cone measurements. However, this convenience comes at the expense of increased uncertainty because I_c is not as directly linked to the soil properties that control drainage rate and is itself influenced by partial drainage effects.

3.2 Model Development for Drainage Effects

A model for representing drainage effects is formulated based on variable rate field penetration tests and lab-based chamber tests and centrifuge tests from the literature as summarized in Table 3.1.

We first inspected the test data from each study to identify the drained tip resistance ($q_{t,drained}$) and undrained tip resistance ($q_{t,undrained}$). Penetration resistances were corrected for rate effects following Nanda et al. (2017). Some studies directly reported $q_{t,undrained}$ (e.g., Krage et al. 2016), in which case the values reported by the authors were used. In cases where the original study did not report a $q_{t,drained}$ and $q_{t,undrained}$, the data was preprocessed according to the following workflow to select appropriate values.

1. Using normalized penetration rate *(V)*, preliminarily assess which measurements are drained, undrained and partially drained using existing guidelines in the literature.
2. Observe whether the anticipated trends are present in the tip resistance and measured pore pressure data. For instance, q_t is expected to reach saturation (i.e., exhibit no change for modest changes in V) when it is completely drained or undrained. Similarly, excess pore pressure is expected to be zero for drained penetration and constant despite increase in penetration velocities during fully undrained shearing.
3. For datasets where the drained penetration was not reached, a curve was fitted to the data in $q_t/q_{t,undrained}$ vs. V space and $\Delta u/\Delta u_{ref}$ vs. V as per DeJong and Randolph (2012) using Equations (3.2) and (3.3) to obtain the drained tip resistance value.

$$\frac{\Delta u}{\Delta u_{undrained}} \approx 1 - \frac{1}{1+\left(\frac{V}{V_{50}}\right)^{c}} \tag{3.2}$$

$$\frac{q}{q_{undrained}} \approx 1 + \left(\frac{q_{drained}/q_{undrained} - 1}{1+\left(\frac{V}{V_{50}}\right)^{c}} \right) \tag{3.3}$$

The parameter c controls the maximum rate of change in excess pore pressure and V_{50} is the normalized penetration rate at which one half of the excess pore pressure for undrained penetration is mobilized.

Table 3.1 Variable rate CPTs performed in the field

Reference	Description
Holmsgaard et al. 2016	Site in Dronninglund, Denmark consisting of sandy silts with clay bands.
Krage et al. 2016	Historic test sites Leonardini51, GraniteConst123, River Park A, KornbloomB that consisted of liquefiable silts and sandy silt deposits.
Kim et al. 2008	2 sites in Indiana which had silty clay and clayey silt deposits.
Carroll and Paniagua 2018	Site in Halden, Norway consisting of silty marine deposits.
Kim et al. 2008	Chamber tests on blends of silica and kaolin mixtures.
Suzuki and Lehane 2015	Chamber tests on blends of silica and kaolin mixtures.
Price et al. 2019	Centrifuge tests on blends of silica and kaolin mixtures.

Figure 3.7 shows application of the aforementioned workflow to choose the reference cone penetration resistances for site SR-18 between 9.2m to 10.2m depth (Kim et al. 2008), which is a clayey soil. Step (1) of the workflow is implemented as shaded regions in the plot representing the drained, partially drained and undrained regions as per the recommendation by DeJong and Randolph (2012). The standard cone penetration value ($q_{t20,mm/s}$) lies within the undrained region (i.e. $V > 10$) and hence it can be inferred that the standard *CPT* would be the reference undrained condition. The chosen drained cone penetration resistance is based on the near-zero excess pore pressure in the test. Extrapolation was not required in this case to obtain the drained and undrained tip resistances.

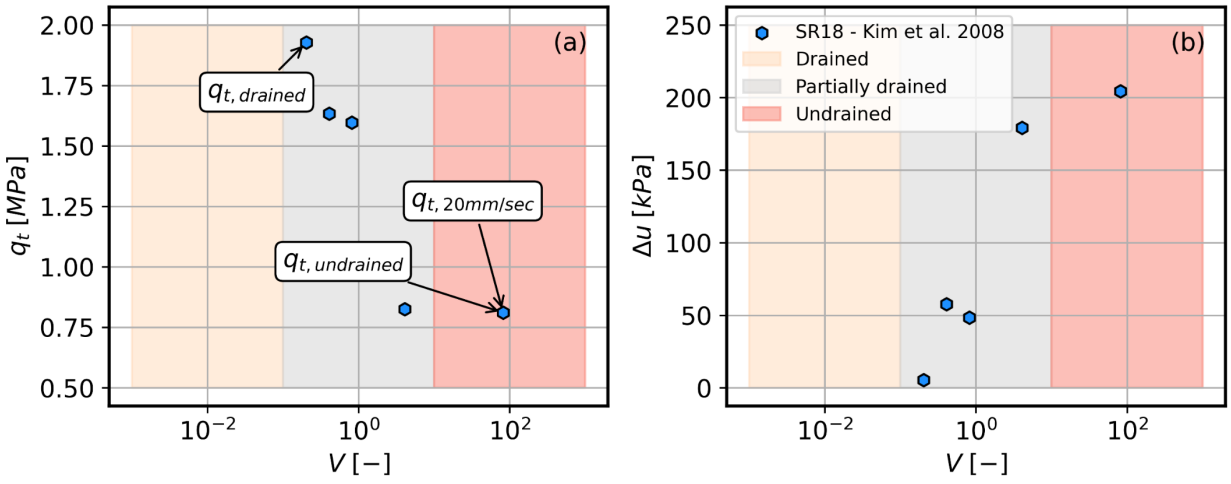

Figure 3.7 Choosing $q_{t,\,drained}$ and $q_{t,\,undrained}$ for SR-18 (Depth 9.2m to 10.2m) based on the workflow without any curve fitting. a) q_t vs. V and b) Δu vs. V

Figure 3.8 shows application of the workflow to obtain the reference cone penetration resistances for site SR-18 between 7.4m to 8.4m depth (Kim et al. 2008). The reference undrained tip resistance can be inferred based on the V value of the data points and the observed saturation in the tip resistance with V at very high penetration rates. However, the reference drained penetration cannot be determined using the available data because none of the measurements produced zero pore pressure change. Hence, there is a need for extrapolation as per DeJong and Randolph (2012) to obtain the reference drained penetration value.

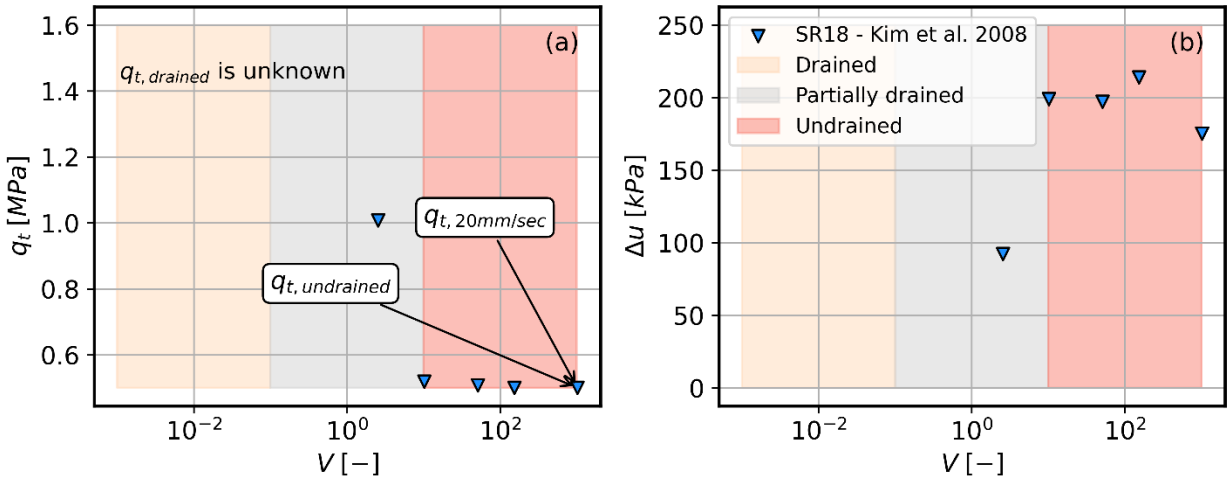

Figure 3.8 Choosing $q_{t,\,drained}$ and $q_{t,\,undrained}$ for SR-18 (Depth 7.4m to 8.4m) based on the workflow with curve fitting. a) q_t vs. V and b) Δu vs. V

The curve fitting and the extrapolation is performed in $q_t/q_{t,undrained}$ vs. V and $\Delta u/\Delta u_{ref}$ vs. V space as shown in Figure 3.9. This method of extrapolation as per Step (3) of the workflow was used for two of the tests. The fitted parameters are verified against the recommendations in the literature (DeJong and Randolph 2012; Suzuki and Lehane 2015). Due to lack of data at lower penetration rates, curve fitting option was not realistic for Halden silt to obtain the reference drained penetration resistance. Hence, the data from Halden silt were used only in the model development of undrained tip resistance.

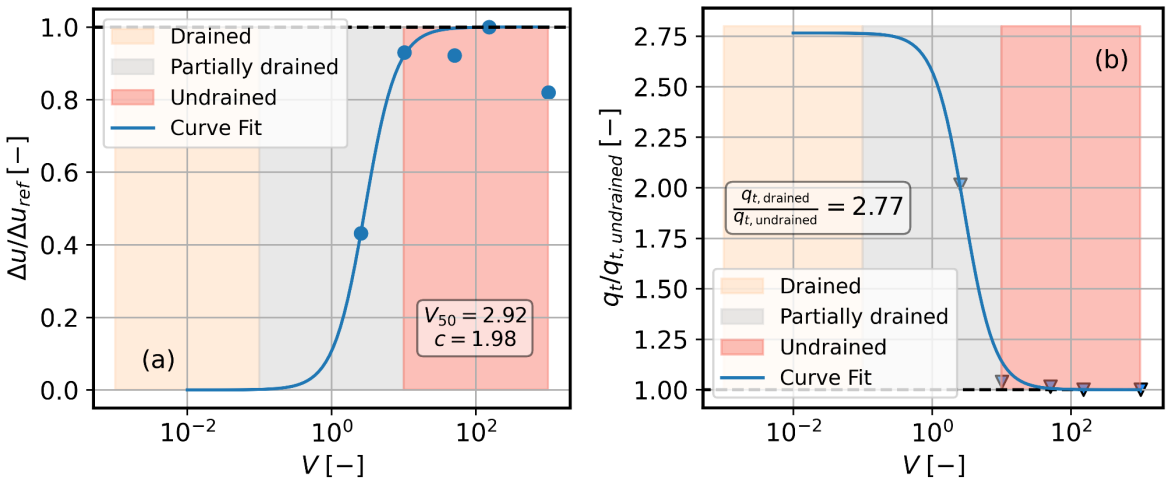

Figure 3.9 Curve fitting as per DeJong and Randolph (2012) to obtain $q_{t,drained}$ for SR-18 (Depth 7.4m to 8.4m)

Using this workflow for all the gathered variable rate penetration tests, we were able to identify the reference drained and undrained tip resistance values. The processed data is provided as a .csv file for reference. Appendix-A provides the descriptions of the columns in the data file.

The figures presented so far in this section have quantified drainage effects on cone tip resistance in terms of the dimensionless velocity parameter, V. However, V is generally not known under field conditions because it requires knowledge of the coefficient of consolidation, c_v or c_h. As a part of the model development, we chose to relate the results from these variable rate penetration tests to soil behavior type index, I_c, which is more easily quantifiable in the field. There are existing criteria in the literature to infer drainage condition during CPT using I_c (Schneider et al. 2012) and I_B (Robertson 2016). By comparing a broad dataset of dissipation test with *CPT*, these I_c-based criteria are not perfect in inferring drainage conditions (Styler et al. 2019). This suggests that using I_c carries some uncertainty that may introduce errors into the methodology. We nevertheless develop a model conditioned on I_c to facilitate practical applications.

The ratios of q_t / $q_{t,undrained}$ and q_t / $q_{t,drained}$ are presented in Figure 3.10 as a function of I_c, where I_c is the value measured at the standard 2 cm/s cone push rate (Robertson 2009). The push rate at which I_c is measured is an important detail because it depends strongly on push rate and drainage conditions. We adopt the standard push rate here so that our model can be applied to typical cone data. The results in Figure 3.10 show that I_c has promise for demarcating the drainage conditions. The information from each suite of variable rate penetration tests is condensed by following this approach.

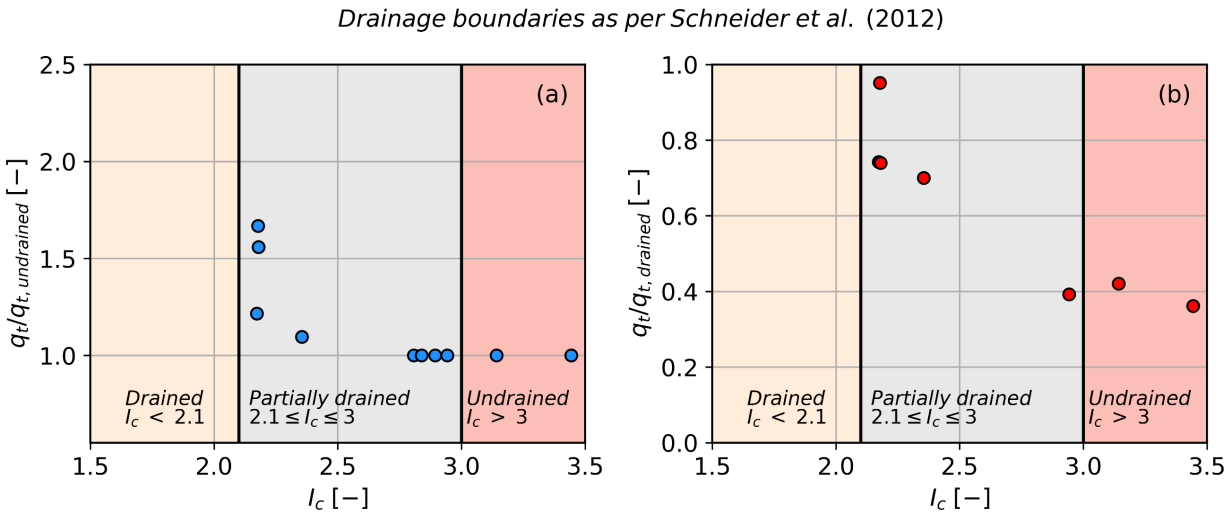

Figure 3.10 Dataset in normalized space a) $q_t/q_{t,undrained}$ vs. I_c and b) $q_t/q_{t,drained}$ vs. I_c

Based on the observed trends in the data, accompanied by contemporary knowledge regarding drainage in clays (high I_c) and sands (low I_c), the logistics functions in Equations (3.4) and (3.5) were selected to represent the trends in the data presented in Fig. 3.10.

$$ln\left(\frac{q_t}{q_{t,undrained}} - 1\right) = ln\left(\frac{\beta_2}{1+e^{\beta_0(I_c-\beta_1)}}\right) + \sigma_1 \cdot \epsilon \tag{3.4}$$

$$ln\left(1 - \frac{q_t}{q_{t,drained}}\right) = ln\left(\frac{(1-\alpha_2)\cdot e^{\alpha_0(I_c-\alpha_1)}}{1+e^{\alpha_0(I_c-\alpha_1)}}\right) + \sigma_2 \cdot \epsilon \tag{3.5}$$

where β_1 and α_1 are the mid-points of the logistic curves, β_0 and α_0 control the spread of the logistic curves β_2 and α_2 control the values of the logistic curves at the extremities, ϵ is a unit normal to represent the distribution of the outputs.

Bayesian inference was used to draw samples from the posterior distributions of the model parameters. We opted to use Bayesian inference rather than frequentist regression because the available data is relatively sparse, and imposing some prior belief provides a means of stabilizing the regression. Further, this approach also provides a systematic way of representing the uncertainty associated with the model and provides the opportunity of easily updating the model parameters when new data is available.

The prior distributions for the model parameters are summarized in Table 3.2. For the case of α_1 and β_1 which are the mid points of the sigmoid, we can estimate their approximate values based on the different drainage zones from Schneider et al. (2012). Based on the data available from the variable rate penetration tests (Figure 3.11), the parameters α_2 and β_2, which control the extreme values of the logistic curve were assigned with informed priors. The uncertainty in the model is controlled by σ_1 and σ_2. Slightly informed half-normal distributions used for σ_1 and σ_2 were

chosen to ensure that the standard deviations in the extremes are similar to the prior knowledge from the field tests.

Table 3.2 Prior distributions of the parameters used in the model.

Variable	Parameter	Prior Distribution	Remark
$\frac{q_t}{q_{t,undrained}}$	β_0 – Controls the steepness of the curve	Normal ~ (μ=6.5, σ =2)	Uninformed prior
	β_1 – Mid point of the sigmoid.	Uniform ~ (2.1,3)	Slighltly informed prior.
	β_2 – Controls maximum value of the sigmoid.	Uniform ~ (0.5, 1.8)	Chosen based on the distribution of the data from the variable rate tests.
$\frac{q_t}{q_{t,drained}}$	α_0 – Controls the steepness of the curve	Normal ~ (μ=6.5, σ =2)	Uninformed prior
	α_1 – Mid point of the sigmoid.	Uniform ~ (2.1,3)	Slighltly informed prior.
	α_2 – Minimum value of the sigmoid	Uniform ~ (0.35,0.65)	Chosen based on the distribution of the data from the variable rate tests.

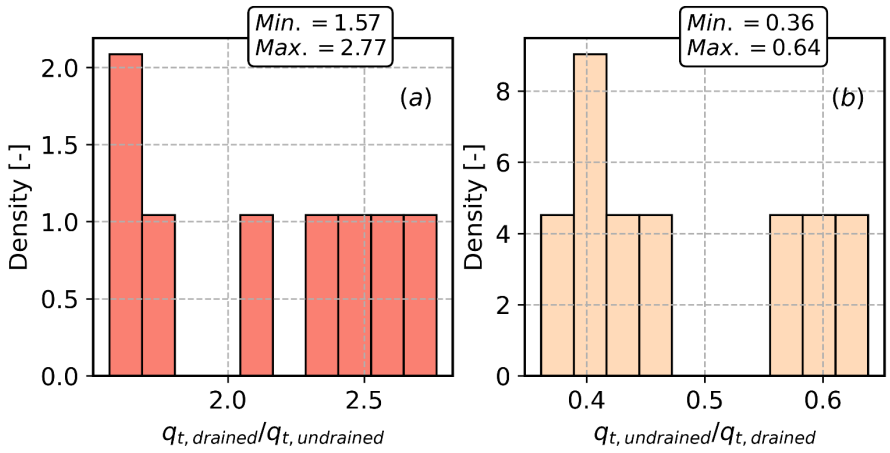

Figure 3.11 Histograms of a) $q_t/q_{t,undrained}$ i.e. $(\beta_2 + 1)$ and b) $q_t/q_{t,drained}$ i.e. (α_2)

With the priors specified, the Bayesian analysis was performed using PyMC package in Python (Abril-Pla et al. 2023) to draw samples from the posterior distribution of each model parameter using the no u-turn sampler (NUTS). 1000 samples were drawn from four independent chains and their distributions are shown in Figure 3.12 and Figure 3.13. The purpose of using multiple sampling chains is to verify that the solution is relatively insensitive to the starting point. All sampling chains produce similar results, and we conclude that the sampling was stable. The posterior distribution of the model parameters represents within-model epistemic uncertainty that would be reduced by training the model on a larger dataset.

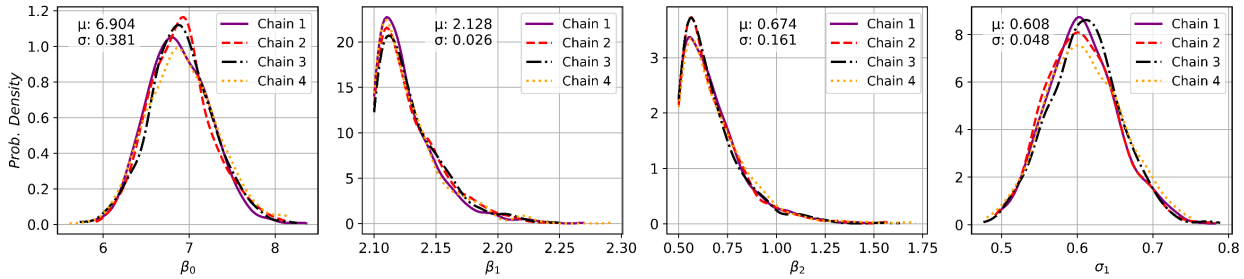

Figure 3.12 Posterior distributions of model parameters in the $q_t/q_{t,undrained}$ model.

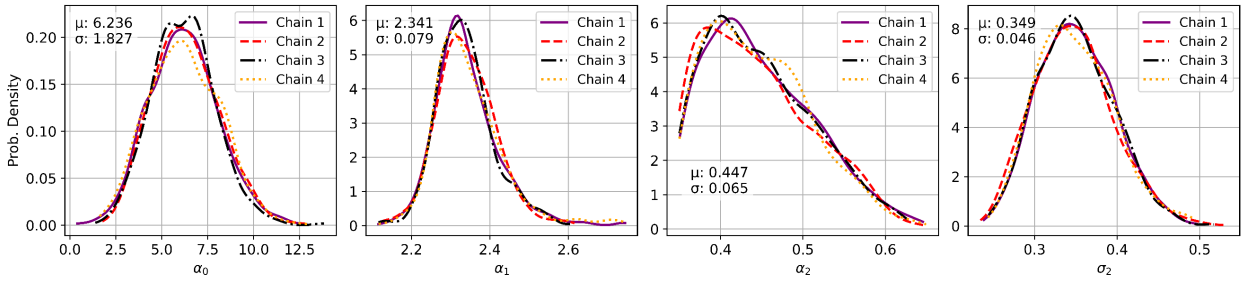

Figure 3.13 Posterior distributions of model parameters in the $q_t/q_{t,drained}$ model.

The resulting relationship is presented in Figure 3.14, including a median prediction and $\pm 1\sigma$ trend lines. The trends for the undrained tip resistance ratio have little uncertainty at high I_c values because the soil is already undrained. Furthermore, the drained tip resistance ratio is unity and has little uncertainty at low I_c because the soil is already drained. Uncertainty increases when drainage conditions during standard rate cone testing deviate from the desired tip resistance ratio.

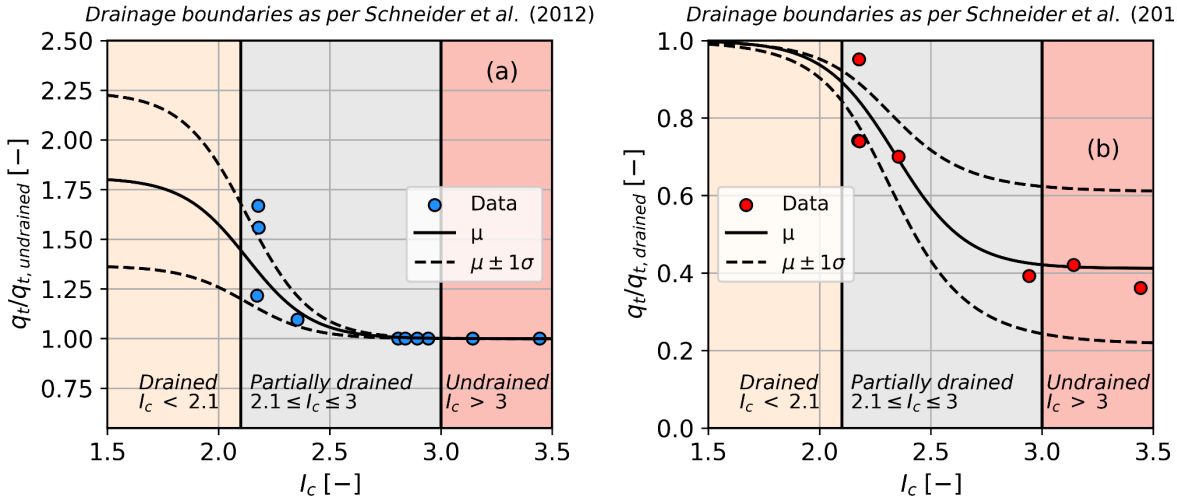

Figure 3.14 Proposed Model for a) $q_t/q_{t,undrained}$ vs. I_c and b) $q_t/q_{t,drained}$ vs. I_c

One aspect of Fig. 3.14 that warrants some discussion is that the undrained tip resistance is always less than the drained tip resistance. However, dilative soils sheared in direct simple shear

experience a reduction in pore pressure, and therefore have an undrained shear strength that is higher than the drained shear strength. Based on this framework, one might postulate that dilative soils would also have higher undrained than drained penetration resistance. However, this is generally not observed. The reason is that the stress path beneath the cone tip differs significantly from direct simple shear. The stress path involves shearing, which would produce negative pore pressure in dilative soils, but also a significant increase in total stress, which produces positive pore pressures regardless of dilatancy. The positive pore pressure increment attributed to the total stress increase is generally significantly larger in amplitude than the negative pore pressure increment attributed to shear. Therefore, drained tip resistance tends to be higher than undrained tip resistance, even for strongly dilative soils.

In order to verify the extent to which this proposition holds true, the state parameter (ξ) and relative state parameter (ξ_R) were evaluated using the CPT data as per Robertson (2010) and Idriss and Boulanger (2008), respectively. Figure 3.15 shows the variation $q_{t,drained}/q_{t,undrained}$ versus a) ξ and b) ξ_R. The general trend from these plots shows that the drained tip resistance is higher than undrained irrespective of the material's state. The only outlier in the trend is River Park (Krage and DeJong 2016) which has a lower drained resistance than the undrained resistance. This data point corresponds to depth in the range of 1.5 to 2.0m in River Park 05 site. Site investigation reports from Bennet et al. (1981) mention the presence of interbedded sand layers within this stratum. The pore pressure measurements from Krage and DeJong (2016) reveal that excess pore pressures that developed at high penetration rates were lower when compared with the tests at low rates. It is unclear the extent to which the presence of the interbedded layers may have contributed to drainage of the silts, and by extension the influence on the measured tip resistance.

Neglecting this outlier, all the other data points show the expected trend, i.e. a higher drained tip resistance than undrained irrespective of the state parameter. Hence, the proposed model, which predicts drained tip resistance is always higher than undrained, is appropriate regardless of the soil's state. Additional data could help us substantiate this conclusion with a greater degree of confidence.

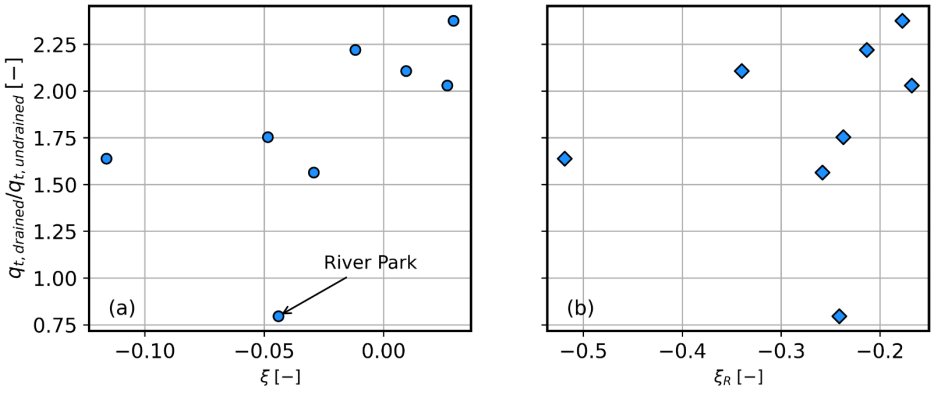

Figure 3.15 Model applicability based on a) state parameter as per (Robertson 2010) and b) Relative state parameter as per (Idriss and Boulanger 2008).

3.3 Influence of Soil Stiffness on Penetration Resistance

Bearing capacity equations, including those commonly used to infer soil properties from cone tip resistance, are often based on limit equilibrium methods that inherently assume the soil behaves in a rigid – plastic manner. However, soil is elasto – plastic and the flexibility and compressibility of the soil influences capacity. For example, shallow foundations are often conceptualized as having three possible failure modes: general bearing failure, local shear, and punching shear. Stiffer soils tend to exhibit general bearing failure, while softer soils tend to exhibit local shear and punching shear. The same mechanisms apply to deep foundations, and to cone penetration end bearing resistance. Vesić (1977) formulated equations for end bearing resistance of piles that depend on friction angle, cohesion, shear modulus, and consolidation stress. The influence of soil stiffness on pile tip resistance is represented by a reduced rigidity index for the soil, I_{rr}, which decreases as shear modulus decreases. Gamez (2024) used chamber tests from the literature to relate cone tip resistance to soil compressibility. For these reasons, increasing FC beyond FC_{th} and up to FC_{th} would be anticipated to cause a corresponding reduction in cone tip resistance due solely to the increase in compressibility.

Assessing the influence of soil stiffness on penetration resistance requires independent knowledge of small strain shear modulus G_{max}. Seismic cone tests are now routinely performed and can provide shear wave velocity details at the site that could in principle be used to make adjustments for the influence of soil compressibility. However, the majority of our dataset does not have a shear wave velocity measurement. Furthermore, it is very difficult to separate the influence of compressibility from the influence of changing drainage conditions. We acknowledge that the effects of compressibility on the measured tip resistance may be significant and would ideally be incorporated into our formulation for computing a clean-sand-equivalent tip resistance. However, the amount of available data is too small to develop a robust relationship at this time.

4 Comparison with Existing Fines Corrections

In this chapter, the findings from Chapters 2 and 3 are integrated to make comparisons of how data points are adjusted using the proposed procedures and using existing fines corrections from models in literature. The framework developed herein differs from traditional fines corrections because our framework involves both liquefaction triggering (i.e. using penetration resistance to estimate cyclic strength) and cyclic failure assessment (i.e. using soil properties to estimate cyclic strength), whereas previous fines correction models have been applied only to penetration resistance-based liquefaction triggering models. For example, the *CRR* for a sand with *FC* = 40% would be controlled by cyclic failure assessment in our framework and may therefore exhibit bias when presented in liquefaction triggering space because CRR_{std}^{s} has no influence on the assigned strength. Rather, for such a data point the relationship should be observed in cyclic failure assessment space to understand any modeling errors. Conversely, a sand with *FC* = 5% and *PI* = 0 would be controlled by liquefaction triggering in our framework and may therefore exhibit bias when presented in cyclic failure assessment space. The relationship should be viewed in triggering space in that case. For these reasons, we also examine the data in FS_L space because FS_L can be applied in both triggering or cyclic failure assessment frameworks.

We adopt the *CPT*-based liquefaction case history database from Boulanger and Idriss (2016) to provide the data points used for comparisons. The specific data points used in the comparison are normalized tip-resistance values with and without fines-corrections (q_{c1N} *and* $q_{c1N,cs}$, respectively) and corresponding cyclic stress ratios normalized for magnitude and overburden (CSR_{std}) from Boulanger and Idriss (2016). The *FC* and plasticity characteristics of the soil represented in their dataset varies over a broad range, therefore each data point is separately evaluated in our framework to derive the appropriate *CRR* and penetration resistance. To facilitate comparisons in liquefaction triggering space, we adjust the CSR_{std} and q_{c1N} data points to "clean sand equivalent" using the proposed model following the steps below:

1. The value of $q_{c1N,drained}$ is computed using Fig. 3.14b based on the measured q_{c1N} and I_c. This represents the influence of fines on tip resistance. Note that $q_{c1N,drained}$ tends to be lower than q_{c1Ncs} because the latter accounts for the effects of fines on both tip resistance and cyclic resistance.

2. The value of CRR_{std}^{s} is computed using the triggering relationship from Boulanger and Idriss (2016) to isolate the differences in the fines content corrections. CRR_{std}^{s} is computed using Equation 4.1

$$\mathrm{CRR}_{std}^{s} = \exp\left(\frac{q_{c1N,drained}}{113} + \left(\frac{q_{c1N,drained}}{1000}\right)^2 - \left(\frac{q_{c1N,drained}}{140}\right)^3 + \left(\frac{q_{c1N,drained}}{137}\right)^4 - 2.8\right) \quad (4.1)$$

3. The value of $\mathrm{CRR}_{std}^{\mathrm{f}}$ is evaluated using Eq. 2.15, where the *OCR* value is taken as 1.2 considering that liquefaction sites tend to contain young geologic materials that are often normally consolidated or weakly over-consolidated.

4. The value of CRR_{std} is then interpolated based on *FC* using Eq. 2.17.

5. A multiplicative fines content adjustment factor (K_{FC}) is then computed using Equation (4.2), which relates the material's CRR_{std} (evaluated using Equation 2.17) to its clean sand equivalent evaluated using $q_{c1N,drained}$ from Eq. 4.1.

$$K_{FC} = \frac{CRR_{std}}{\mathrm{CRR}_{std}^{\mathrm{s}}} \tag{4.2}$$

6. The corrected CSR_{std} is then computed as the *CSR* reported by Boulanger and Idriss (2016) divided by K_{FC}.

In step 3, correlations to evaluate the *OCR* from *CPT* tip resistance (Agaiby and Mayne 2019; Robertson 2009) were evaluated, but ultimately not adopted because they exhibit significant scatter when applied to sands, which dominate the Boulanger and Idriss (2016) dataset. The scatter is likely because the influence of *OCR* cannot readily be separated from the influence of D_R on cone tip resistance since sand density is influenced more by depositional energy than by stress history. Our interpretation was that these relationships provided *OCR* values that were too high given our knowledge of the geological history of the liquefaction sites.

A comparison between the proposed fines corrections and the corrections proposed by Boulanger and Idriss (2016) is provided in Fig. 4.1. The top row of subplots corresponds to the Boulanger and Idriss (2016) fines corrections, and the bottom row of subplots corresponds to our model. The columns of subplots correspond to fines content ranges of 0 – 5%, 5 – 15%, 15 – 35%, and 35 – 100% from left to right, respectively. Within each plot, the solid symbols are cases for which manifestation was observed (i.e., "yes" cases), the open symbols are cases for which manifestation was not observed (i.e., "no" cases), and the green triangles are marginal cases. The fully opaque symbols correspond to q_{c1Ncs} for the top row, and $q_{c1,drained}$ for the bottom row. The semi-transparent symbols correspond to q_{c1N} in both sets of figures (no fines corrections). The size of the symbols corresponds to the weight assigned to CRR_{std}^{s} based on *FC*, and the symbols are largest for the left column and smallest for the right column. The motivation for sizing the symbols in this manner is that the liquefaction triggering framework becomes a less important contributor to CRR_{std} as *FC* increases, and the symbol sizes represent the importance of triggering in the overall assignment of CRR_{std}.

For the first column, corresponding to *FC* = 0 - 5%, there is no fines correction using the Boulanger and Idriss (2016) method, hence the q_{c1N} and q_{c1Ncs} data points overlie each other. Using the proposed methodology, there are a few cases in which $q_{c1,drained}$ is larger than q_{c1N} (i.e., the points move horizontally), but the CRR_{std} values remain unchanged (i.e., the points do not move vertically). The points move horizontally because we use I_c to infer drainage conditions during CPT testing, with adjustments beginning at $I_c > 1.5$. However, the size of the adjustment is

relatively minor, and would have no impact on inferring a boundary curve separating the yes / no cases.

For the second column, corresponding to FC = 5 – 15%, we see horizontal movement of the data points using the Boulanger and Idriss (2016) fines correction, which begins to take effect for FC > 5%. To help understand how the points are moving, we have drawn arrows between the "no" data points. Doing so for all of the data points would clutter the figure. Using the proposed fines content correction, the data points also shift horizontally by amounts that are sometimes larger and sometimes smaller than the Boulanger and Idriss (2016) fines correction. The relative amount of movement of the data points depends on the relationship between FC and I_c, which contains significant uncertainty (e.g., Hudson et al. 2023). Some small vertical movement of the data points is also visible in the bottom row of the second column of plots, which indicates that these data points are influenced by both CRR^{s}_{std} and CRR^{f}_{std}. However, the vertical movements are small, indicating that CRR^{s}_{std} is the more influential contributor in this FC range.

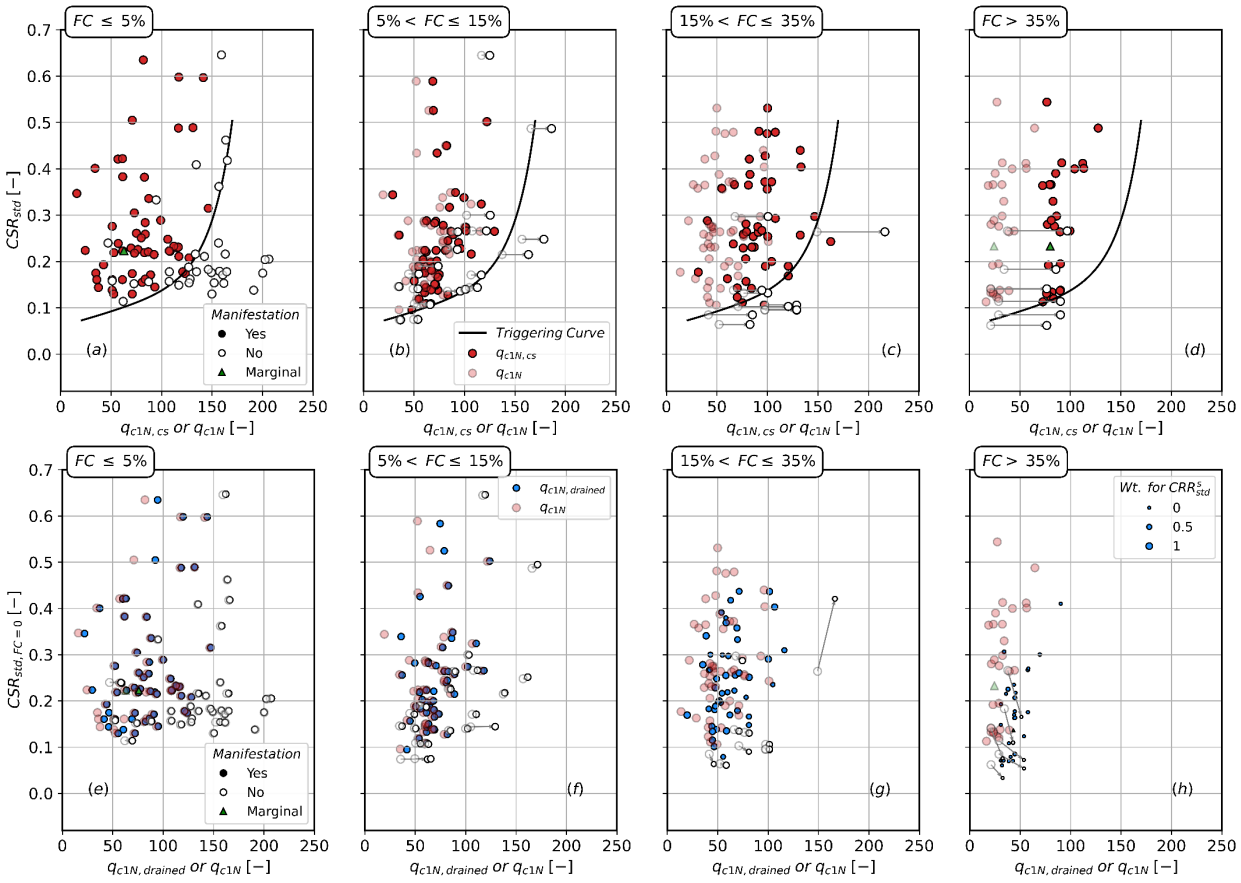

Figure 4.1 Comparison between fines correction from Boulanger and Idriss (2016) [a-d] and proposed corrections [e-h] in a triggering framework. The triggering curve shown in [a-d] is for clean sands.

Moving on to the third column of plots for FC = 15 – 35%, we observe that the Boulanger and Idriss (2016) fines content correction involves more horizontal movement of the data points compared with the proposed model. This is because their Δq_{c1N} values for FC = 35%, range from about Δq_{c1N} = 45 for q_{c1N} = 20 to Δq_{c1N} = 70 for q_{c1N} = 140. The ratio of q_{c1N} / q_{c1Ncs} is therefore in the range of about 0.3 to 0.5 for FC = 35%. By contrast, the minimum ratio of q_{c1N} / $q_{c1,drained}$ in the proposed model is only 0.4 for high I_c values (Fig. 3.14) and increases as I_c decreases. The relative amount of shift is consistent with the observation that Δq_{c1N} from Boulanger and Idriss (2016) is intended to account for all influences of fines on liquefaction behavior, whereas in our method, the horizontal shift reflects only the influence of fines on cone tip resistance. The vertical shift of the data points is significant using our method, with a predominantly downward movement observed. The downward movement arises from the value of CRR_{std} being larger than CRR^{s}_{std}, in which case $K_{FC} > 1$. Recall that the reported CSR values are divided by K_{FC} to impose an inverse fines correction for the purpose of plotting the data points relative to a clean sand equivalent triggering curve. The reasons why K_{FC} is larger than 1 for these cases are (1) $q_{c1,drained}$ remains relatively low, and the corresponding values of CRR^{s}_{std} are therefore fairly small, and (2) the soils are assumed to be slightly overconsolidated, which increases CRR^{f}_{std}, and therefore CRR_{std}.

Finally, moving on to the last column for $FC > 35\%$, we observe that our fines content correction has shifted many of the data points downward, with a significant number of "yes" observations lying below the clean sand triggering curve. These data points are entirely controlled by CRR^{f}_{std}, and for that reason the liquefaction triggering framework has no weight (hence the small symbol sizes). Arguably, data with $FC > 35\%$ should not be plotted in liquefaction triggering space using our fines correction, but rather in cyclic failure assessment space. Nevertheless, we plot the points here for comparison purposes and completeness.

Having compared the fines corrections using a liquefaction triggering framework, we now turn our attention to comparing data points within a cyclic failure assessment framework. To remove the influence of OCR on CRR^{f}_{std}, we adjust the data to a normally consolidated equivalent value using Equation (4.3), where K_{OCR} is the OCR correction factor that was evaluated in Section 2.4.2.

$$CSR_{std,OCR=1} = \frac{CSR_{std}}{K_{OCR}} \tag{4.3}$$

The relationship of $CSR_{std,OCR=1}$ is shown in Figure 4.2 for various FC ranges, along with the cyclic failure assessment relationships defined by Equation 2.15 and Dahl et al. (2018). Dahl's model is converted to N=15 cycles, assuming b=0.192 (Equation 2.1). Conventions for open and closed circles are the same as for Figure 4.1. Symbol sizes now correspond to the weights used for CRR^{f}_{std} in the proposed model (i.e., larger symbols for high FC). The materials were assumed to be non-plastic when PI values were not reported in the case histories. Fig. 4.2(a) for $FC > 35\%$ is plotted vs. PI since soils in this FC range exhibited variations in plasticity. However, FC is plotted on the abscissa for Fig. 4.2(b, c) because all of the soils with FC = 5 to 35% were interpreted as being nonplastic.

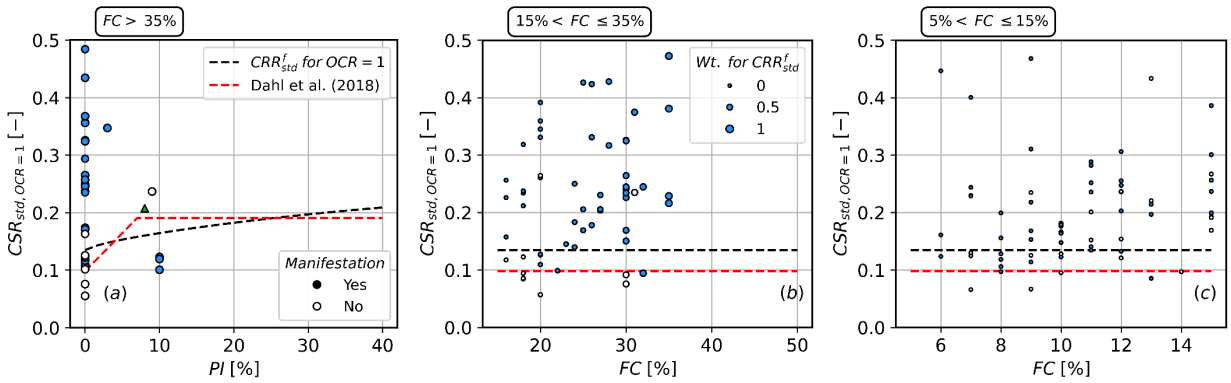

Figure 4.2 Comparison of proposed framework with case history dataset from Boulanger and Idriss (2016) (Assumed PI=0 when not reported.)

Fig. 4.2(a) indicates that the cyclic failure assessment framework reasonably separates the yes / no case history data for $FC > 35\%$. Notable outliers include three closed symbols with PI=10 below the resistance curves (i.e., false negative predictions). These correspond to sites (Y24, Y28 and Y29) from the 1976 **M**=7.6 Tangshan earthquake (Arulanandan et al. 1982), which have high uncertainties because the PGA estimates were based on intensity correlations. Furthermore, two open symbols plot above the curve, and an additional six closed circles lie slightly below the proposed curve at $PI = 0$. The open circles above the curve might be cases where cyclic softening did occur but did not manifest at the surface. The high FC points are better separated by the cyclic failure assessment framework in Fig. 4.2(a) than in the liquefaction triggering framework in Fig. 4.1(d) when our fines content correction is used.

The cyclic failure assessment framework also works reasonably well for the soils with $FC = 15\%$ - 35% in Fig. 4.2(b). These data points lie in the range where the interpolation between CRR^s_{std} and CRR^f_{std} is important. The triggering curve in Fig. 4.1(g) and cyclic softening curve in Fig. 4.2(b) exhibit similar ability to separate the yes / no cases.

The cyclic failure assessment framework does not form a distinct boundary between the yes / no cases for the soils with FC = 5% to 15%. As per the proposed framework, CSR_{std} is significantly influenced by CRR^s_{std} for these materials and hence a triggering framework (Figure 4.1f) shows better separation between the case histories than the cyclic failure assessment framework in Figure 4.2c.

Given the fact that weight is almost 0 for CRR^f_{std} while evaluating the cyclic strength of materials with $FC < 5\%$, it is not efficient to assess these case histories using a cyclic failure assessment framework. A triggering framework (Figure 4.1e) is well suited for such materials.

Having evaluated the data in a liquefaction triggering and cyclic failure assessment frameworks, we now turn our attention to evaluating the factor of safety, which reflects the output of the entire

fines correction method. The factor of safety is computed using Equation 4.4, where CSR_{std} is reported in the case history database and CRR_{std} is evaluated using the different models under consideration. Results are presented as a confusion matrix in Table 4.1.

$$FS_L = \frac{CRR_{std}}{CSR_{std}} \tag{4.4}$$

The Boulanger and Idriss (2016) model had 5 false negative predictions (i.e., predictions of "no" liquefaction manifestation at sites where it was in fact observed), whereas the proposed model has 11 false negatives. The predictions are otherwise almost identical. The superior performance of the Boulanger and Idriss (2016) model is likely due to the fact that their fines content correction is derived from the case history data against which it is being compared, whereas the proposed model was not developed from the case history data.

Table 4.1 Confusion matrix for Boulanger and Idriss (2016) and proposed framework.

		Actual		
		Liquefied	**Non-liquefied**	**Marginal**
Boulanger Idriss (2016)	$FS_L < 1$	175	32	2
	$FS_L \geq 1$	5	39	0
Present study	$FS_L < 1$	169	31	2
	$FS_L \geq 1$	11	40	0

The fines content correction proposed by Boulanger and Idriss (2016) is based on a dataset consisting largely of sand, with only a few fine-grained soils. Application of their model to low plasticity or nonplastic fine-grained soils therefore carries significant uncertainty since these soils were not well represented in the training dataset for their model. We therefore explore how their model compares with laboratory measurements of *CRR* for the silty soils tested by Dadashiserej et al. (2024), Soysa (2015) and Sanin (2010). These studies performed cone penetration tests at sites where they also performed drilling and high quality sampling, followed by cyclic direct simple shear testing to measure *CRR*. Data from Dadashiserej et al. (2024) consisted of low plasticity (Site F: *PI* = 0 to 5) soils with *FC* in the range from 38% to 52%, medium plasticity (Site AB-L: *PI* = 11 to 15) fine grained soils, and higher plasticity fine grained soils (Site E: *PI* = 25 to 28). Meanwhile Soysa (2015) studied Fraser River silts with *PI*=5 (Site CT) and *PI*=7 (Site JS). Sanin (2010) investigated Fraser River silts (FRS) in Richmond, BC. We first interpret the reported CPT data using the Boulanger and Idriss (2016) fines content correction to compute q_{c1Ncs} and then CRR_{std}. Only soils deemed susceptible to liquefaction (i.e., the Sites F, CT, JS and FRS subsets) were analyzed in this manner to be consistent with their triggering framework. For the proposed model, the reported *PI* and *OCR* values were used to compute CRR_{std}^{f} using Eq. 2.15 and the

drained tip resistance (Fig. 3.14b) was used to get CRR^{s}_{std}. CRR_{std} was then obtained through interpolation using Eq. 2.16. The results are plotted in Figure 4.3. The measured CRR_{std} values from Soysa (2015) had to be corrected for *OCR*s as per Eq. 2.8 to match the field conditions.

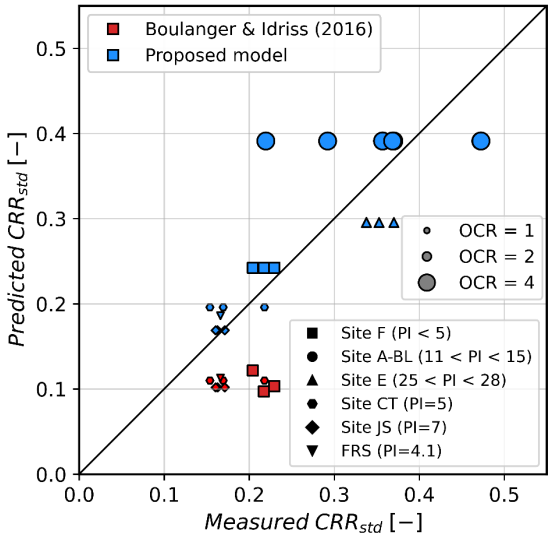

Figure 4.3 Comparison of the proposed framework and the fines correction from Boulanger and Idriss (2016) for sand-like fine-grained soils tested by Dadashiserej et al. (2024), Soysa (2015) and Sanin(2010).

The CRR_{std} computed using the fines correction and triggering model by Boulanger and Idriss (2016) for Site F, CT, JS and FRS results in significantly lower values of CRR_{std} compared with the measured values. Values of q_{c1N} were relatively low for these soils, ranging from 10 to 40. The *FC*s were all relatively high, resulting in Δq_{c1N} values ranging from 50 to 60. As a result, the Δq_{c1N} values constituted between 60% and 80% of the computed q_{c1Ncs} values. The computed CRR_{std} values are therefore strongly influenced by the fines content correction, diminishing the influence of the measured q_{c1N} value. These soils happen to be overconsolidated, with *OCR* values ranging from about 1.4 to 3. The measured tip resistance is likely influenced by *OCR*, but the tip resistance has diminished influence on the computed *CRR* values in this case since q_{c1Ncs} is more significantly influenced by Δq_{c1N}. These observations demonstrate that application of the Boulanger and Idriss (2016) model to high *FC* materials may produce errors because these soils are not well represented in their training dataset. Sampling and testing remains the best approach for assessing the cyclic strength of these soil types.

The CRR_{std} values computed using the proposed model are reasonably consistent with the observed values. They are particularly accurate for the materials from sites F, CT, JS and FRS. For these soils, the proposed procedures appear to provide superior predictions to a fines correction applied within a triggering framework, even for liquefaction susceptible soils. More testing is needed to confirm this finding since it is based on a relatively small sample of data points.

5 Alternative Intensity Measures

Liquefaction triggering evaluation is generally based on peak ground acceleration (*PGA*) and earthquake magnitude (**M**). Fundamental reasons for using these two parameters in combination are (1) *PGA* relates to cyclic stress, and (2) **M** relates to number of loading cycles. In this manner, the combination of *PGA* and **M** captures salient features of demand, and provides a direct basis for assessing demand in a manner that can be directly compared with stress-controlled harmonic cyclic laboratory tests. However, using both *PGA* and **M** complicates the application of liquefaction triggering procedures at sites where a range of different magnitudes control seismic hazard. For example, the Pacific Northwest contains significant contributions from shallow crustal earthquakes with magnitudes up to about 8, and subduction earthquakes with magnitudes potentially higher than 9. The state of practice is to select a design level *PGA* value from a probabilistic seismic hazard analysis (PSHA), and select **M** from the PSHA disaggregation. Often, the modal magnitude is selected. However, many magnitudes contribute to seismic hazard, and errors associated with selecting a single magnitude are unclear. Moreover, for a given **M**, the number of uniform stress cycles depends on site-source distance, site conditions, fault types and directivity effects (e.g., Liu et al. 2001). Therefore, magnitude is an imperfect predictor of number of stress cycles. For these reasons, there would be benefit in identifying an alternative scalar-valued intensity measure that inherently captures the effects of both shaking intensity and duration.

Intensity measures such as Arias Intensity (I_A), cumulative absolute velocity (*CAV*), and peak ground velocity (*PGV*) have potential as alternatives to *PGA* and **M** in liquefaction evaluation. For example, Kayen and Mitchell (1997) proposed a liquefaction triggering procedure using I_A to represent seismic demand. Kramer and Mitchell (2006) found that cumulative absolute velocity with an acceleration cutoff of 5 cm/s^2 (i.e., CAV_5) is a good predictor of excess pore pressure development. Bullock et al. (2021) found that *CAV* for the input motion at the base of numerical models (i.e., the outcropping motion) correlated well with liquefaction development. Kramer and Sideras (2022) showed that phasing of energy in input stress signals influenced the rate of buildup of pore pressure in direct simple shear tests with broadband stress histories. They proposed a ground motion intensity measure denoted IM_L that accounts for phasing of stress demands, and therefore can account for features of ground motion that are not captured by other IM's (e.g., directivity effects, rupture characteristics, etc.). Models relating liquefaction occurrence to *PGV* have not been developed, but *PGV* is an attractive alternative to *PGA* because it relates more closely with shear strain, and plastic shear strain is fundamentally related to pore pressure development. For shear waves propagating in an unbounded elastic medium, maximum shear strain amplitude is equal to PGV / V_S. Of course, the presence of a free surface alters this relationship, but nevertheless *PGV* warrants exploration as an alternative intensity measure.

A limitation to applying alternative intensity measures to liquefaction problems has been that the alternative IM's have not been estimated at sites known to have exhibited liquefaction effects. To address this limitation, Pretell et al. (2024) computed values of alternative intensity measures at

liquefaction sites in the Next Generation Liquefaction (NGL) database. They first compute within-event residuals using recorded ground motions for earthquakes that produced liquefaction observations at one or more sites. Bayesian inference is then used to develop samples of variogram models representing the spatial correlation of the within event residuals. Earthquakes with large numbers of recordings produce variogram models with less uncertainty, while those with only a few recordings carry more uncertainty. The within-event residual(s) are then interpolated at the liquefaction site(s) using Kriging. Finally, the within event residual is added to the median ground motion model prediction at the liquefaction site. Interpolation is performed on within-event residuals instead of directly on ground motions because within-event residuals are anticipated to be a stationary random field that is well-suited to Kriging. In the absence of ground motion recordings for a particular earthquake, their procedure becomes identical to application of a ground motion model and carries significant uncertainty. In the case where a liquefaction site has a collocated instrument, the ground motion is well characterized with uncertainty arising only from sensor measurement error and potential effects of liquefaction on earthquake ground motion. For these reasons, Pretell et al. (2024) also present standard deviation terms for each computed ground motion. In addition to *PGA*, Pretell et al. (2024) computed *PGV*, I_A, and *CAV* at each of the liquefaction sites in the NGL database.

As part of their study, Pretell et al. (2024) conducted a preliminary study to identify whether *PGV*, I_A, and *CAV* provide more predictive power than *PGA* and **M**. Many of the NGL sites were included in previous liquefaction model development efforts in which analysts selected critical layer properties for developing a bound between cases for which liquefaction manifestation was and was not observed. Data for the critical layers used in the model by Boulanger and Idriss (2016) were adopted for this purpose. Figure 5.1 presents overburden- and fines-corrected cone tip resistance (q_{c1Ncs}) vs. *PGA*, *PGV*, I_A, and *CAV*, where open symbols are for case histories where liquefaction manifestation was not observed, and closed circles are case histories where manifestation was observed. Intensity measures with strong predictive power would be anticipated to provide a better separation of the yes / no case histories, thereby enabling development of more robust liquefaction triggering procedures. Pretell et al. (2024) concluded that *PGA* and *PGV* exhibited similar ability to separate yes / no cases, while I_A and *CAV* were worse.

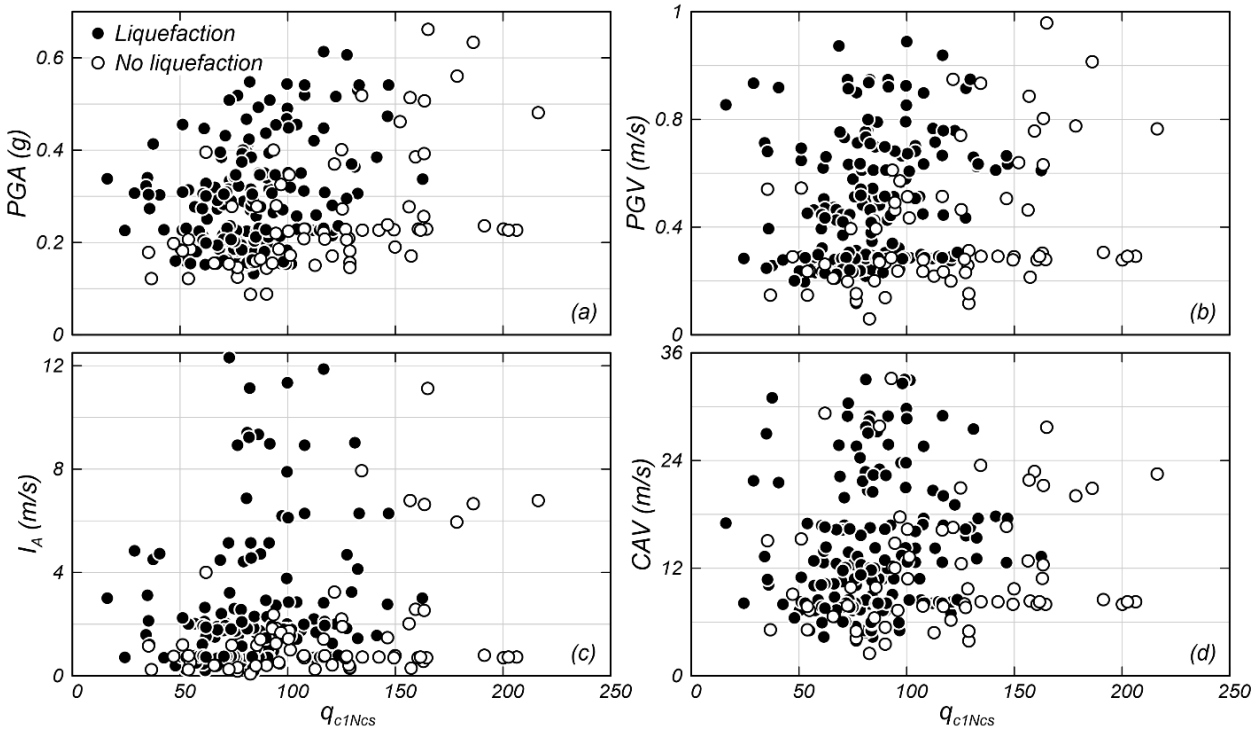

Figure 5.1. Critical layer overburden- and clean-sand-corrected tip resistance vs. (a) *PGA*, (b) *PGV*, (c) I_A, and (d) *CAV*.

These preliminary findings point to *PGA* and **M** being superior to alternative intensity measures for predicting liquefaction at field case history sites. However, a number of unexplored factors may contribute to the relatively poor performance in this preliminary study. First, the stress-based liquefaction triggering procedures include a depth correction factor, r_d, to account for wave propagation effects and the corresponding reduction in shear stress with depth compared with a case in which acceleration is constant at all depths. These factors have been developed from ground response analyses and are calibrated for use in *PGA*-based models. Similar procedures do not exist for *PGV*, *CAV*, or I_A. Second, *PGA*-based models are also corrected for overburden and static shear effects. These corrections were not applied in Fig. 5.1. Pretell et al. (2024) found that applying these corrections and using magnitude and overburden corrected cyclic stress ratio, $CSR_{M=7.5,\sigma'=1atm}$, was superior to *PGA* in separating yes / no case histories. This is anticipated since $CSR_{M=7.5,\sigma'=1atm}$ accounts for the influence of number of loading cycles, stress demands at the depth of the liquefiable layer, and the influence of confining pressure on liquefaction resistance. Finally, multiple layers might contribute to liquefaction manifestation, but Fig. 5.1 presents properties of one single critical layer for each site. Ulmer et al. (2024) developed a profile-based liquefaction manifestation model that accounts for all layers in a profile, including probabilistic relationships for susceptibility, triggering, and manifestation. They used *PGA* and **M** in their procedures, and have not evaluated alternative intensity measures. Future efforts to address these issues may result in improvements of alternative intensity measures for modeling liquefaction manifestations from field case histories.

6 Conclusions

6.1 Summary

A fines content correction was developed in which the influence of fines content on penetration resistance and on cyclic resistance are formulated separately. This is a departure from fines corrections used in existing triggering models in which a single adjustment to the measured penetration resistance is used to account for both effects. Published fines content corrections have been developed largely based on surface evidence of liquefaction (or lack thereof) during past earthquakes, the properties of the critical layer, and the shaking intensity and magnitude of the earthquake that produced the observation. Separating the effects of fines on penetration resistance and cyclic resistance has the potential to improve fines content corrections by isolating each effect, which can vary between soils having different fines contents, stress history, and plasticity. Variable rate cone penetration test data was used to quantify the tip resistance that would be measured under drained loading conditions, conditional on the soil behavior type index measured at the standard penetration rate of 2 cm/s. This approach captures the influence of fines content on drainage conditions during cone penetration testing. Cyclic laboratory test data was used to quantify the influence of fines on cyclic resistance, with clean sands represented by a liquefaction triggering framework, and fine-grained soils represented by a cyclic failure assessment framework. The cyclic resistance of sands with appreciable fines is interpolated between these two behavior types. Application of the fines content framework to cone penetration test case history behavior shows good agreement with observations.

This report also evaluates whether alternative intensity measures, including peak ground velocity, Arias intensity, and cumulative absolute velocity exhibit better predictive power than peak acceleration and magnitude. Values of the alternative intensity measures interpolated at liquefaction sites from the Next Generation Liquefaction database are used to evaluate field case history data. Alternative intensity measures do not show improved predictive power based on preliminary findings presented herein.

6.2 Recommendations

The influence of fines content on penetration resistance was constrained using the best data set that is currently available, but which is nonetheless relatively small dataset and therefore carries significant uncertainty. Additional variable rate cone penetration tests would improve the model developed herein. Furthermore, the influence of compressibility on cone penetration test resistance was not considered, aside from the influence of compressibility on drainage. Increasing compressibility is associated with decreasing tip resistance. Improved understanding of the influence of fines on compressibility, and the influence of compressibility on cone tip resistance would facilitate a better model for clean sand-equivalent tip resistance.

When compared with the sands from the Boulanger and Idriss (2016) CPT dataset, their fines correction performed better than the proposed model. This is not surprising since their fines content correction was developed from those same case history data, whereas ours was not. However, the Boulanger and Idriss (2016) fines correction and triggering model under-predicted the cyclic resistance of susceptible silts tested by Dadashiserej et al. (2024), Soysa (2015) and Sanin (2010) whereas the proposed model performed well. The dataset from which the Boulanger and Idriss (2016) fines correction was developed contains very few silts, and the model is not really intended for application to silt, but rather to sand with fines. The fines correction constitutes a significant percentage of the q_{c1Ncs} value used to compute *CRR* using the Boulanger and Idriss (2016) method, potentially diminishing the influence of *OCR* and other factors that contribute to the measured tip resistance. More data will be needed to assess whether susceptible silts should be analyzed using a liquefaction triggering method with a fines content adjustment or using a cyclic failure assessment procedure similar to the one proposed in this study.

The finding that alternative intensity measures did not outperform *PGA* and **M** compared with field case history data should be considered preliminary because numerous factors were not considered in this study. First, methods based on *PGA* and **M** apply a depth correction factor, r_d, that accounts for the influence of wave propagation on reduction in demand with depth. These factors improve the predictive power of *PGA*-based triggering models by accounting for the physics of wave propagation. Such factors have not been developed for alternative intensity measures, and were therefore not applied here. Developing them could improve the predictive power of alternative intensity measures. Second, the preliminary analysis was performed only for critical layer properties at each site, whereas the soil profile is known to influence liquefaction triggering and manifestation behavior. Evaluating alternative intensity measures within a profile-based framework, such as the one developed by Ulmer et al. (2024) would be required to more fully vet the utility of alternative IMs.

References

Abril-Pla, O., V. Andreani, C. Carroll, L. Dong, C. J. Fonnesbeck, M. Kochurov, R. Kumar, J. Lao, C. C. Luhmann, O. A. Martin, M. Osthege, R. Vieira, T. Wiecki, and R. Zinkov. (2023). "PyMC: a modern, and comprehensive probabilistic programming framework in Python." *PeerJ Comput. Sci.*, 9: e1516. PeerJ Inc. https://doi.org/10.7717/peerj-cs.1516.

Acar, Y. B., and M. T. Tumay. (1986). "Strain Field Around Cones in Steady Penetration." *J. Geotech. Eng.*, 112 (2): 207–213. American Society of Civil Engineers. https://doi.org/10.1061/(ASCE)0733-9410(1986)112:2(207).

Agaiby, S. S., and P. W. Mayne. (2019). "CPT Evaluation of Yield Stress Profiles in Soils." *J. Geotech. Geoenvironmental Eng.*, 145 (12): 04019104. American Society of Civil Engineers. https://doi.org/10.1061/(ASCE)GT.1943-5606.0002164.

Amini, F., and G. Z. Qi. (2000). "Liquefaction Testing of Stratified Silty Sands." *J. Geotech. Geoenvironmental Eng.*, 126 (3): 208–217. American Society of Civil Engineers. https://doi.org/10.1061/(ASCE)1090-0241(2000)126:3(208).

Arulanandan, K., Douglas, B. J., Qu, Y. Z., Junfei, X., Chengchun, W., and Qizhi, H. (1982). "Evaluation of earthquake induced liquefaction in Tientsin during the Tangshan Earthquake P. R. C." *Proc., United States-People's Republic of China Bilateral Workshop on Earthquake Engineering*, E-3-1–E-3-42.

Basson, M. S., A. Martinez, and J. T. DeJong. (2024). "DEM Investigation of the Effect of Gradation on the Strength, Dilatancy, and Fabric Evolution of Coarse-Grained Soils." *J. Geotech. Geoenvironmental Eng.*, 150 (8): 04024060. American Society of Civil Engineers. https://doi.org/10.1061/JGGEFK.GTENG-12310.

Baziar, M. H., and R. Ziaie Moayed. (2003). "Effect of silt content in sand on CPT results using calibration chambers." *Int. J. Civ. Eng.*

Belkhatir, M., A. Arab, N. Della, H. Missoum, and T. Schanz. (2010). "Liquefaction Resistance of Chlef River Silty Sand: Effect of Low Plastic Fines and other Parameters." *Acta Polytech. Hung.*, 7 (2).

Bennett, M. J., McLaughlin, P. V., Sarmiento, J. S., and Youd, T. L. (1984). Geotechnical investigation of liquefaction sites, Imperial Valley, California. U.S. Geological Survey, Open-File Report 84-252, 103 pp.

Bolton, M. D. 1986. "The strength and dilatancy of sands." *Géotechnique*, 36 (1): 65–78. ICE Publishing. https://doi.org/10.1680/geot.1986.36.1.65.

Boominathan, A., K. Rangaswamy, and K. Rajagopal. (2010). "Effect of non-plastic fines on liquefaction resistance of Gujarat sand." *Int. J. Geotech. Eng.*, 4 (2): 241–253. Taylor & Francis. https://doi.org/10.3328/IJGE.2010.04.02.241-253.

Boulanger, R. W. (2003). "High Overburden Stress Effects in Liquefaction Analyses." *J. Geotech. Geoenvironmental Eng.*, 129 (12): 1071–1082. American Society of Civil Engineers. https://doi.org/10.1061/(ASCE)1090-0241(2003)129:12(1071).

Boulanger, R. W., and I. M. Idriss. (2006). "Liquefaction Susceptibility Criteria for Silts and Clays." *J. Geotech. Geoenvironmental Eng.*, 132 (11): 1413–1426. American Society of Civil Engineers. https://doi.org/10.1061/(ASCE)1090-0241(2006)132:11(1413).

Boulanger, R. W., and I. M. Idriss. (2007). "Evaluation of Cyclic Softening in Silts and Clays." *J. Geotech. Geoenvironmental Eng.*, 133 (6): 641–652. American Society of Civil Engineers. https://doi.org/10.1061/(ASCE)1090-0241(2007)133:6(641).

Boulanger, R. W., and I. M. Idriss. (2016). “CPT-Based Liquefaction Triggering Procedure.” *J. Geotech. Geoenvironmental Eng.*, 142 (2): 04015065. American Society of Civil Engineers. https://doi.org/10.1061/(ASCE)GT.1943-5606.0001388.

Bray, J. D., and R. B. Sancio. (2006). “Assessment of the Liquefaction Susceptibility of Fine-Grained Soils.” *J. Geotech. Geoenvironmental Eng.*, 132 (9): 1165–1177. American Society of Civil Engineers. https://doi.org/10.1061/(ASCE)1090-0241(2006)132:9(1165).

Bray, J. D., R. B. Sancio, T. Durgunoglu, A. Onalp, T. L. Youd, J. P. Stewart, R. B. Seed, O. K. Cetin, E. Bol, M. B. Baturay, C. Christensen, and T. Karadayilar. (2004). “Subsurface Characterization at Ground Failure Sites in Adapazari, Turkey.” *J. Geotech. Geoenvironmental Eng.*, 130 (7): 673–685. American Society of Civil Engineers. https://doi.org/10.1061/(ASCE)1090-0241(2004)130:7(673).

Bullock, Z., Dashti, S., Liel, A.B., Porter, K.A., and Maurer, B.W. (2022). “Probabilistic liquefaction triggering and manifestation models based on cumulative absolute velocity.” J. Geotech. Geoenviron. Eng., 148(3), doi: 10.1061/(ASCE)GT.1943-5606.0002729

Carlton, B., K. Ulmer, T. Nguyen, Q. Parker (2023). Next Generation Liquefaction (NGL) - Supporting Studies: Overburden and Initial Shear Stress. *DesignSafe-CI*. https://doi.org/10.17603/ds2-c9fr-x257

Carlton, B., Ulmer, K., Zimmaro, P., Hudson, K. S., Brandenberg, S. J., Stewart, J. P., and Kramer, S. L. (2025) "Evaluating the effects of overburden stress on soil liquefaction: insights from cyclic test data." *Journal of Geotechnical and Geoenvironmental Engineering,*ASCE, Accepted

Carraro, J. A. H., P. Bandini, and R. Salgado. (2003). “Liquefaction Resistance of Clean and Nonplastic Silty Sands Based on Cone Penetration Resistance.” *J. Geotech. Geoenvironmental Eng.*, 129 (11): 965–976. https://doi.org/10.1061/(ASCE)1090-0241(2003)129:11(965).

Castro, G. M., J. Park, and J. C. Santamarina. 2023. “Revised Soil Classification System: Implementation and engineering implications.” J. Geotech. Geoenviron. Eng. 149 (11): 04023109. https://doi.org/10.1061/JGGEFK.GTENG-10447.

Cetin, K. O., R. B. Seed, R. E. Kayen, R. E. S. Moss, H. T. Bilge, M. Ilgac, and K. Chowdhury. (2018). “SPT-based probabilistic and deterministic assessment of seismic soil liquefaction triggering hazard.” *Soil Dyn. Earthq. Eng.*, 115: 698–709. https://doi.org/10.1016/j.soildyn.2018.09.012.

Chen, G., Q. Wu, K. Zhao, Z. Shen, and J. Yang. (2020). “A Binary Packing Material–Based Procedure for Evaluating Soil Liquefaction Triggering during Earthquakes.” *J. Geotech. Geoenvironmental Eng.*, 146 (6): 04020040. American Society of Civil Engineers. https://doi.org/10.1061/(ASCE)GT.1943-5606.0002263.

Chen, J., and S. M. Olson. (2022). “Effect of Overconsolidation on Cyclic Resistance of Soils.” *J. Geotech. Geoenvironmental Eng.*, 148 (11): 04022087. American Society of Civil Engineers. https://doi.org/10.1061/(ASCE)GT.1943-5606.0002905.

Cheng, K., and Y. Zhang. (2024). “A Cyclic Resistance Ratio Model of Sand-Fines Mixtures Based on Cyclic Triaxial Test.” *Geotech. Geol. Eng.*, 42 (2): 1021–1033. https://doi.org/10.1007/s10706-023-02602-6.

Ching, J., and K.-K. Phoon. (2014). “Transformations and correlations among some clay parameters — the global database.” *Can. Geotech. J.*, 51 (6): 663–685. NRC Research Press. https://doi.org/10.1139/cgj-2013-0262.

Chu, D. B., J. P. Stewart, S. Lee, J. S. Tsai, P. S. Lin, B. L. Chu, R. B. Seed, S. C. Hsu, M. S. Yu, and M. C. H. Wang. (2004). "Documentation of soil conditions at liquefaction and non-liquefaction sites from 1999 Chi-Chi (Taiwan) earthquake." *Soil Dyn. Earthq. Eng.*, 24 (9–10): 647–657.

Cubrinovski, M., and K. Ishihara. (2002). "Maximum and Minimum Void Ratio Characteristics of Sands." *Soils Found.*, 42 (6): 65–78. https://doi.org/10.3208/sandf.42.6_65.

Cubrinovski, M., S. Rees, and E. Bowman. (2010). "Effects of Non-plastic Fines on Liquefaction Resistance of Sandy Soils." *Earthq. Eng. Eur.*, M. Garevski and A. Ansal, eds., 125–144. Dordrecht: Springer Netherlands.

Dadashiserej, A., A. Jana, A. W. Stuedlein, and T. M. Evans. (2023). "Effect of Overburden Stress and Plasticity on the Cyclic Resistance of Silts." *J. Geotech. Geoenvironmental Eng.*, 149 (12): 06023007. American Society of Civil Engineers. https://doi.org/10.1061/JGGEFK.GTENG-11345.

Dadashiserej, A., A. Jana, A. W. Stuedlein, and T. M. Evans. (2024). "Cyclic Resistance Models for Transitional Silts with Application to Subduction Zone Earthquakes." *J. Geotech. Geoenvironmental Eng.*, 150 (2): 04023135. American Society of Civil Engineers. https://doi.org/10.1061/JGGEFK.GTENG-11671.

Dahl, K. (2011). "Evaluation of Seismic Behavior of Intermediate and Fine-Grained Soils." *PhD Thesis*, University of California, Davis, CA

Dahl, K., Boulanger, R.W., and DeJong, J.T. (2018) "Trends in Experimental Data of Intermediate Soils for Evaluating Dynamic Strength", *11th U.S. National Conference on Earthquake Engineering*, Los Angeles, CA, June 25-29, 2018.

Dash, H. K., T. G. Sitharam, and B. A. Baudet. (2010). "Influence of Non-Plastic Fines on the Response of a Silty Sand to Cyclic Loading." *Soils Found.*, 50 (5): 695–704. https://doi.org/10.3208/sandf.50.695.

DeJong, J. T., and M. Randolph. (2012). "Influence of Partial Consolidation during Cone Penetration on Estimated Soil Behavior Type and Pore Pressure Dissipation Measurements." *J. Geotech. Geoenvironmental Eng.*, 138 (7): 777–788. American Society of Civil Engineers. https://doi.org/10.1061/(ASCE)GT.1943-5606.0000646.

Dickenson, S. E., A. Khosravifar, M. Beaty, J. Bock, D. Moug, S. Schlechter, J. Six, and Inc. New Albion Geotechnical. (2021). *Cyclic and Post-Cyclic Behavior of Silt-Rich, Transitional Soils of the Pacific Northwest: A Data Archive for Geo-professionals in Practice and Research*.

Ecemis, N., M. M. Monkul, Y. E. Tütüncü, and M. S. Arik. (2022). "CPT-based liquefaction resistance of clean and silty sands: a drainage conditions based approach." *Bull. Earthq. Eng.*, 20 (15): 7957–7980. https://doi.org/10.1007/s10518-022-01501-0.

El-Mamlouk, H. H., A. K. Hussein, and A. M. Hassan. (2007). "Cyclic Behavior of Nonplastic Silty Sand under Direct Simple Shear Loading." *Soil Stress-Strain Behav. Meas. Model. Anal.*, H. I. Ling, L. Callisto, D. Leshchinsky, and J. Koseki, eds., 615–624. Dordrecht: Springer Netherlands.

Eslami, M. (2017). "Experimental Mapping of Elastoplastic Surfaces for Sand and Cyclic Failure of Low-Plasticity Fine-Grained Soils." *PhD Thesis*, University of California, Los Angeles, CA.

Finnie, I. M. S., and Randolph, M. F. (1994). "Punch-through and liquefaction induced failure of shallow foundations on calcareous sediments." Proc., 7th Int. Conf. on Behavior of Offshore Structures, M. Hoo Fatt, ed., Cambridge, MA, 217–230.

Gamez, J. A. (2024). “Compressibility-based interpretation of cone penetration test data.”, *PhD Thesis*, University of Illinois at Urbana-Champaign.

Gobbi, S., P. Reiffsteck, L. Lenti, M. P. S. d’Avila, and J.-F. Semblat. (2022). “Liquefaction triggering in silty sands: effects of non-plastic fines and mixture-packing conditions.” *Acta Geotech.*, 17 (2): 391–410. https://doi.org/10.1007/s11440-021-01262-1.

Gu, X., K. Zuo, C. Hu, and J. Hu. (2024). “Liquefaction resistance and small strain stiffness of silty sand: Effects of host sand gradation and fines content.” *Eng. Geol.*, 335: 107546. https://doi.org/10.1016/j.enggeo.2024.107546.

Holmsgaard, R., B. N. Nielsen, and L. B. Ibsen. (2016). “Interpretation of Cone Penetration Testing in Silty Soils Conducted under Partially Drained Conditions.” *J. Geotech. Geoenvironmental Eng.*, 142 (1): 04015064. American Society of Civil Engineers. https://doi.org/10.1061/(ASCE)GT.1943-5606.0001386.

Hu, J., Y. Xiao, J. Shi, A. W. Stuedlein, and T. M. Evans. 2024. “Small-strain shear modulus and liquefaction resistance of calcareous sand with non-plastic fines.” *Géotechnique*, 1–15. https://doi.org/10.1680/jgeot.23.00199.

Huang, Y.-T., A.-B. Huang, Y.-C. Kuo, and M.-D. Tsai. (2004). “A laboratory study on the undrained strength of a silty sand from Central Western Taiwan.” *Soil Dyn. Earthq. Eng.*, Soil Liquefaction: Evaluation, Instrumentation, and In Situ Tests, 24 (9): 733–743. https://doi.org/10.1016/j.soildyn.2004.06.013.

Hudson, K. S., K. J. Ulmer, P. Zimmaro, S. L. Kramer, J. P. Stewart, and S. J. Brandenberg. 2024. “Relationship between Fines Content and Soil Behavior Type Index at Liquefaction Sites.” Journal of Geotechnical and Geoenvironmental Engineering, 150 (5): 06024001. American Society of Civil Engineers. https://doi.org/10.1061/JGGEFK.GTENG-12146.

Ishihara, K. (1993). “Liquefaction and flow failure during earthquakes.” *Géotechnique*, 43 (3): 351–451. ICE Publishing. https://doi.org/10.1680/geot.1993.43.3.351.

Ishihara, K., and H. Takatsu. (1979). “Effects of overconsolidation and K0, conditions on the liquefaction characteristics of sands.” *Soils Found.*, 19 (4): 59–68. https://doi.org/10.3208/sandf1972.19.4_59.

Ishihara, K, Yamazaki, A, and Haga, K., (1985). Liquefaction of Ko consolidated sand under cyclic rotation of principal stress direction with lateral constraint, *Soils and Foundations, Japanese Society of Soil Mechanics and Foundation Engineering* 5(4), 63–74.

Jamiolkowski, M., Ladd, C.C., Germain, J.T., and Lancellotta, R. 1985. New developments in field and laboratory testing of soils. In Proceedings of the 11th International Conference on Soil Mechanics and Foundation Engineering, San Francisco. Vol. 1, pp. 57–153.

Kayen, R.E., and Mitchell, J.K. (1997). “Assessment of liquefaction potential during earthquakes by Arias intensity” *J. Geotech. Geoenviron. Eng.*, 123(12), 1162-1174.

Kim, K., M. Prezzi, R. Salgado, and W. Lee. (2008). “Effect of Penetration Rate on Cone Penetration Resistance in Saturated Clayey Soils.” *J. Geotech. Geoenvironmental Eng.*, 134 (8): 1142–1153. American Society of Civil Engineers. https://doi.org/10.1061/(ASCE)1090-0241(2008)134:8(1142).

Krage, C. P., and J. T. DeJong. (2016). “Influence of Drainage Conditions during Cone Penetration on the Estimation of Engineering Properties and Liquefaction Potential of Silty and Sandy Soils.” *J. Geotech. Geoenvironmental Eng.*, 142 (11): 04016059. American Society of Civil Engineers. https://doi.org/10.1061/(ASCE)GT.1943-5606.0001543.

Krage, C. P., J. T. DeJong, and F. Schnaid. (2015). “Estimation of the Coefficient of Consolidation from Incomplete Cone Penetration Test Dissipation Tests.” *J. Geotech. Geoenvironmental*

Eng., 141 (2): 06014016. American Society of Civil Engineers. https://doi.org/10.1061/(ASCE)GT.1943-5606.0001218.

Kramer, S.L., and Mitchell, R.A. (2006). "Ground motion intensity measures for liquefaction hazard evaluation." *Earthquake Spectra*, 22(2), 413-438.

Kramer, S.L., and Sideras, S. S. (2022). "Transient loading effects on pore pressure generation and the response of liquefiable soils." *4th International Conference on Performance Based Design in Earthquake Geotechnical Engineering*, 74-99.

Liu, A.H., Stewart, J.P., Abrahamson, N.A. and Moriwaki, Y., 2001. Equivalent number of uniform stress cycles for soil liquefaction analysis. *Journal of Geotechnical and Geoenvironmental Engineering*, *127*(12), pp.1017-1026.

Mahmoodzadeh, H., and M. F. Randolph. (2014). "Penetrometer Testing: Effect of Partial Consolidation on Subsequent Dissipation Response." *J. Geotech. Geoenvironmental Eng.*, 140 (6): 04014022. American Society of Civil Engineers. https://doi.org/10.1061/(ASCE)GT.1943-5606.0001114.

Manmatharajan, M. V., and S. Sivathayalan. (2011). "Effect of overconsolidation on cyclic resistance correction factors K σ and K α."

Mesri, G., and N. Huvaj. (2007). "Shear Strength Mobilized in Undrained Failure of Soft Clay and Silt Deposits." 1–22. American Society of Civil Engineers. https://doi.org/10.1061/40917(236)1.

Monkul, M. M., S. B. Kendir, and Y. E. Tütüncü. (2021). "Combined effect of fines content and uniformity coefficient on cyclic liquefaction resistance of silty sands." *Soil Dyn. Earthq. Eng.*, 151: 106999. https://doi.org/10.1016/j.soildyn.2021.106999.

Monkul, M. M., and Y. E. Tütüncü. (2024). "Revisiting the effect of relative density on cyclic liquefaction of clean and silty sands: the crossing effect." *Bull. Earthq. Eng.*, 22 (8): 3817–3843. https://doi.org/10.1007/s10518-024-01910-3.

Montgomery, J., R. W. Boulanger, and L. F. Harder. (2014). "Examination of the Kσ Overburden Correction Factor on Liquefaction Resistance." *J. Geotech. Geoenvironmental Eng.*, 140 (12): 04014066. American Society of Civil Engineers. https://doi.org/10.1061/(ASCE)GT.1943-5606.0001172.

Nanda, S., V. Sivakumar, P. Hoyer, A. Bradshaw, K. G. Gavin, H. Gerkus, S. Jalilvand, R. B. Gilbert, P. Doherty, and J. Fanning. 2017. "Effects of Strain Rates on the Undrained Shear Strength of Kaolin." *Geotech. Test. J.*, 40 (6): 951–962. https://doi.org/10.1520/GTJ20160101.

Oka, L. G., M. Dewoolkar, and S. M. Olson. (2018). "Comparing laboratory-based liquefaction resistance of a sand with non-plastic fines with shear wave velocity-based field case histories." *Soil Dyn. Earthq. Eng.*, 113: 162–173. https://doi.org/10.1016/j.soildyn.2018.05.028.

Papadopoulou, A. I., and T. M. Tika. (2021). "Laboratory-Based Correlation between Liquefaction Resistance and Shear Wave Velocity of Sand with Fines." *Geotechnics*, 1 (2): 219–242. Multidisciplinary Digital Publishing Institute. https://doi.org/10.3390/geotechnics1020012.

Phoon, K. K., and J. V. Retief (Eds.). (2016). *Reliability of Geotechnical Structures in ISO2394*. London: CRC Press.

Polito, C. P., and J. R. Martin. (2001). "Effects of Nonplastic Fines on the Liquefaction Resistance of Sands." *J. Geotech. Geoenvironmental Eng.*, 127 (5): 408–415. American Society of Civil Engineers. https://doi.org/10.1061/(ASCE)1090-0241(2001)127:5(408).

Preciado Reyes, A. (2021). “Undrained Cyclic Loading of Low Plasticity Silty Soils in the Pacific Northwest Using Laboratory and Field Cyclic Shear Testing.” *MS Thesis*. Portland State University.

Pretell, R., Brandenberg, S. J., and Stewart, J. P. (2024) "Ground motion intensity measures at liquefaction field case history sites." GIRS-2024-02. (*B. John Garrick Risk Institute, Natural Hazards Risk and Resiliency Research Center*, UCLA)

Price, A. B., R. W. Boulanger, and J. T. DeJong. (2019). “Centrifuge Modeling of Variable-Rate Cone Penetration in Low-Plasticity Silts.” *J. Geotech. Geoenvironmental Eng.*, 145 (11): 04019098. American Society of Civil Engineers. https://doi.org/10.1061/(ASCE)GT.1943-5606.0002145.

Price, A. B., R. W. Boulanger, J. T. DeJong, A. M. P. Bastidas, and D. Moug. (2015). “Cyclic Strengths and Simulated CPT Penetration Resistances in Intermediate Soils.” *Proc 6th Int. Conf. Earthq. Geotech. Eng.* Christchurch, New Zealand.

Qamar, S. U., B. Alshameri, W. Hassan, Z. Maqsood, and A. Haider. 2024. “Predictive modeling of Atterberg’s limits of soil passing through sieve #40 and #200 using artificial neural networks and multivariate regression: advancing sustainable construction practices.” Multiscale and Multidiscip. Model. Exp. and Des., 7 (6): 5809–5827. https://doi.org/10.1007/s41939-024-00560-x.

Rangaswamy, K., A. Boominathan, and K. Rajagopal. (2010). “Influence of initial conditions on liquefaction resistance of silty sands.” *Geomech. Geoengin.*, 5 (3): 199–211. Taylor & Francis. https://doi.org/10.1080/17486021003706572.

Reid, D., and A. Fourie. (2017). “Effects of Polymer Treatment on Undrained Strengths and Cyclic Behavior of a Low-Plasticity Slurry.” *J. Geotech. Geoenvironmental Eng.*, 143 (6): 04017007. American Society of Civil Engineers. https://doi.org/10.1061/(ASCE)GT.1943-5606.0001660.

Robertson, P. K. (2009). “Interpretation of cone penetration tests — a unified approach.” *Can. Geotech. J.*, 46 (11): 1337–1355. https://doi.org/10.1139/T09-065.

Robertson, P. K. (2010). “Estimating in-situ state parameter and friction angle in sandy soils from CPT.” *2nd Int. Symp. Cone Penetration Test.* Huntington Beach, CA, USA,.

Robertson, P. K. (2016). “Cone penetration test (CPT)-based soil behaviour type (SBT) classification system — an update.” *Can. Geotech. J.*, 53 (12): 1910–1927. NRC Research Press. https://doi.org/10.1139/cgj-2016-0044.

Sanin, M. V. (2010). “Cyclic shear loading response of Fraser River delta silt.”, *PhD Thesis*, University of British Columbia.

Saye, S. R., S. M. Olson, and K. W. Franke. (2021). “Common-Origin Approach to Assess Level-Ground Liquefaction Susceptibility and Triggering in CPT-Compatible Soils Using ΔQ.” *J. Geotech. Geoenvironmental Eng.*, 147 (7): 04021046. American Society of Civil Engineers. https://doi.org/10.1061/(ASCE)GT.1943-5606.0002515.

Schneider, J. A., J. N. Hotstream, P. W. Mayne, and M. F. Randolph. (2012). “Comparing CPTU Q–F and Q–Δu2/σv0′soil classification charts.” *Géotechnique Lett.*, 2 (4): 209–215. ICE Publishing. https://doi.org/10.1680/geolett.12.00044.

Seed, HB (1979). Soil liquefaction and cyclic mobility evaluation for level ground during earthquakes, J. Geotech. Engrg., ASCE, 105 (2), 201-255.

Seed, H. B., I. M. Idriss, and I. Arango. (1983). “Evaluation of Liquefaction Potential Using Field Performance Data.” *J. Geotech. Eng.*, 109 (3): 458–482. American Society of Civil Engineers. https://doi.org/10.1061/(ASCE)0733-9410(1983)109:3(458).

Shahsavari, M., and S. Sivathayalan. (2014). “Effects of overconsolidation and the direction of principal stresses on liquefaction susceptibility of Fraser River sand.” Regina, SK.

Soysa, A. N. (2015). “Monotonic and cyclic shear loading response of natural silts.”, *PhD Thesis*, University of British Columbia.

Stark, T. D., H. Choi, and S. McCone. (2005). “Drained Shear Strength Parameters for Analysis of Landslides.” *J. Geotech. Geoenvironmental Eng.*, 131 (5): 575–588. American Society of Civil Engineers. https://doi.org/10.1061/(ASCE)1090-0241(2005)131:5(575).

Steven L. Kramer and Jonathan P Stewart (2025). Geotechnical Earthquake Engineering, 2nd Edition. Taylor & Francis, New York, NY. 1060 pages.

Styler, M. A., J. Greig, and M. Nguyen. (2019). “Inferring Drainage Conditions during In Situ Cone Penetration.” 62–70. American Society of Civil Engineers. https://doi.org/10.1061/9780784482131.007.

Suzuki, Y., and B. M. Lehane. (2015). “Cone penetration at variable rates in kaolin–sand mixtures.” *Int. J. Phys. Model. Geotech.*, 15 (4): 209–219. ICE Publishing. https://doi.org/10.1680/ijpmg.14.00043.

Thevanayagam, S. (2007). “Intergrain contact density indices for granular mixes—I: Framework.” *Earthq. Eng. Eng. Vib.*, 6 (2): 123–134. https://doi.org/10.1007/s11803-007-0705-7.

Thevanayagam, S., U. Sivaratnarajah, V. Veluchamy, and Q. Huang. (2019). “Liquefaction Screening—Non-plastic Silty Sands and Sands.” *Geotech. Des. Pract. Sel. Top.*, K. Ilamparuthi and R. G. Robinson, eds., 15–32. Singapore: Springer.

Thevanayagam, S., V. Veluchamy, Q. Huang, and U. Sivaratnarajah. (2016). “Non-plastic silty sand liquefaction, screening, and remediation.” *Soil Dyn. Earthq. Eng.*, 6ICEGE – Earthquake Geotechincal Engineeering, 91: 147–159. https://doi.org/10.1016/j.soildyn.2016.09.027.

Tokimatsu, K., and Yoshimi, H., "Field Correlation of Soil Liquefaction with SPT and Grain Size," Proceedings of the International Conference on Recent Advances in Geotechnical Earthquake Engineering and Soil Dynamics, 1981

Tom, J.G. (2011). “Numerical study of drainage effects on prediction of cone penetration resistance in a silty-clay.” MS thesis, University of California, Davis.

Tatsuoka, F., Iwasaki, T., Tokida, K., Yasuda, S., Hirose, M., Imai, T., and Kon-no, M., "Standard Penetration Tests and Soil Liquefaction Potential Evaluation," Soils and Foundations, Japanese Society of Soil Mechanics and Foundation Engineering, Vol. 20, No. 4, Dec, 1980

Tütüncü, Y. E., S. B. Kendir, and M. M. Monkul. (2022). “Influence of silt content on cyclic liquefaction of sand: conflicting effects of relative density.”

Ulmer, K., Hudson, K. S., Brandenberg, S. J., Zimmaro, P., Pretell, R., Carlton, B., Kramer, S. L., and Stewart, J. P. (2024) "Next Generation Liquefaction models for susceptibility, triggering, and manifestation, Rev 1." RIL-2024-13. (US Nuclear Regulatory Commission, Research Information Letter, Office of Nuclear Regulatory Commission)

Verma, P. (2019). “Monotonic and cyclic shear loading response of natural silts from British Columbia, Canada.”, *PhD Thesis*, University of British Columbia.

Verma, P., and D. Wijewickreme. (2018). “Effect of High Initial Effective Confining Stress on the Mechanical Response of Natural Silt.” 208–218. American Society of Civil Engineers. https://doi.org/10.1061/9780784481486.022.

Vesic, A. S. (1977), “Design of Pile Foundation,” Synthesis of Highway Practice 42, Transportation Research Board, National Research Council, Washington, D.C., 68 pages.

Wei, X., and J. Yang. (2019). “Characterizing the effects of fines on the liquefaction resistance of silty sands.” *Soils Found.*, 59 (6): 1800–1812. https://doi.org/10.1016/j.sandf.2019.08.010.

Wijewickreme, D., M. V. Sanin, and G. R. Greenaway. (2005). “Cyclic shear response of fine-grained mine tailings.” *Can. Geotech. J.*, 42 (5): 1408–1421. NRC Research Press. https://doi.org/10.1139/t05-058.

Yang, J., L. M. Wei, and B. B. Dai. (2015). “State variables for silty sands: Global void ratio or skeleton void ratio?” *Soils Found.*, 55 (1): 99–111. https://doi.org/10.1016/j.sandf.2014.12.008.

Zhu, C., Byrd, R. H., Lu, P., & Nocedal, J. (1997). Algorithm 778: L-BFGS-B: Fortran Subroutines for Large-Scale Bound-Constrained Optimization. ACM Transactions on Mathematical Software (TOMS), 23(4), 550-560.

Appendix A

Table A.1 Column descriptions for the CPT dataset

Category	Field	Units	Description
Meta Data	**Ref_ID**	-	Reference ID to the original study.
	Mat_ID	-	Entries with same Mat_ID correspond to the results from variable test CPTs performed in a particular site / soil.
	Soil	-	Name of the soil / site
	PI	%	Plasticity Index
	FC	%	Fines Content
CPT Data	**qt (Mpa)**	MPa	Measured tip resistance during CPT.
	qt_rate	MPa	Processed tip resistance – Accounted for rate effects.
	fs (kPa)	kPa	Skin friction measured during CPT.
	gamma_sat(kN/m3)	kN/m^3	Saturated unit weight of the soil
	sigma (kPa)	kPa	Total stress at the level of measured tip resistance.
	u0(kPa)	kPa	Hydrostatic pore pressure at the level of measured CPT.
	del_u(kPa)	kPa	Excess pore pressure developed during penetration.
	eff_sigma(kPa)	kPa	Effective stress at the level of measured tip resistance.
	v(mm/s)	mm/s	Penetration velocity
	d(mm)	mm	Diameter of the cone
Drainage Parameters	**ch(m2/s)**	m^2/s	Coefficient of consolidation in the horizontal direction.
	cv(m2/s)	m^2/s	Coefficient of consolidation in the vertical direction.
	V	-	Normalized penetration rate.
Reference Conditions	**q_ref(Mpa)**	MPa	Reference undrained tip resistance for the Mat_ID
	q_drained(Mpa)	MPa	Reference drained tip resistance for the Mat_ID
	Remark	-	Remarks on depth and other details